THESIS APPROVAL
GRADUATE SCHOOL, KASETSART UNIVERSITY

Master of Engineering (Chemical Engineering)
DEGREE

Chemical Engineering   Chemical Engineering
FIELD   **DEPARTMENT**

TITLE: Simulation of Momentum, Heat, and Mass Transfer in a Proton Exchange
Membrane Fuel Cell

NAME: Mr. Kitipoom Tangwongpimook

THIS THESIS HAS BEEN ACCEPTED BY

_____ **THESIS ADVISOR**
(Associate Professor Terdthai Vatanatham, Ph.D.   )

_____ **THESIS CO-ADVISOR**
(Associate Professor Sunun Limtrakul, D.Sc.   )

_____ **DEPARTMENT HEAD**
(Associate Professor Phungphai Phanawadee, D.Sc.   )

APPROVED BY THE GRADUATE SCHOOL ON   _____

_____ **DEAN**
(Associate Professor Gunjana Theeragool, D.Agr.)

THESIS

SIMULATION OF MOMENTUM, HEAT, AND MASS TRANSFER IN A PROTON EXCHANGE MEMBRANE FUEL CELL

KITIPOOM TANGWONGPIMOOK

A Thesis Submitted in Partial Fulfillment of

the Requirements for the Degree of

Master of Engineering (Chemical Engineering)

Graduate School, Kasetsart University

2010

Kitipoom Tangwongpimook 2010: Simulation of Momentum, Heat, and Mass Transfer in a Proton Exchange Membrane Fuel Cell. Master of Engineering (Chemical Engineering), Major Field: Chemical Engineering, Department of Chemical Engineering. Thesis Advisor: Associate Professor Terdthai   Vatanatham, Ph.D. 144 pages.

The non-isothermal two-dimensional simulation in GDL and membrane of proton exchange membrane fuel cell was investigated for studying gas phase transport characteristics. Assuming that the thickness of catalyst can be negligible, thus the geometry consists of gas diffusion layers at anode and cathode, and electrolyte membrane with catalyst layers as interface boundaries between GDL's and membrane. The simulation was carried out under steady state condition. The non-isothermal and compressible fluid was assumed. The problem was solved by FEMLAB 3.0a and simulated under finite element method. The variables and parameters were coupled and solved at the same time. The simulation results show that the current production rate is higher at the reaction surface behind the channel rib. The hydrogen concentration near the reaction surface is higher and varies inversely with the operating voltage while the oxygen concentration at the cathode reaction surface is lower and varies with the operating voltage. The high water concentrations near upper edge of the anode rib and the lower edge of cathode gas diffusion layers are observed. Near the reaction surface, the anode water concentration is lower but the cathode water concentration is higher. The temperature distribution in the gas diffusion layer is higher near the membrane behind the flow channel and the temperature at cathode is higher than at anode. From the study of polarization curve, the activation losses vary slightly with temperature while ohmic losses vary inversely with temperature. The polarization results show that the fuel cell performance is increased with the operating temperature. The increasing of operating pressure can improve the OCV due to high hydrogen and oxygen partial pressure in the fuel cell.

_____   _____   _____/_____/_____

Student's signature   Thesis Advisor's signature

ACKNOWLEDGEMENTS

TABLE OF CONTENTS

Page

LIST OF TABLES

LIST OF FIGURES

LIST OF FIGURES (Continued)

LIST OF FIGURES (Continued)

LIST OF FIGURES (Continued)

LIST OF FIGURES (Continued)

LIST OF ABBREVIATIONS

a_w	=	activity of water
c	=	concentration (mol m^{-3})
D_{ij}	=	binary diffusivity of component i and j (m^{2}s^{-1})
$D_{ij}{}^0$	=	binary diffusivity of component i and j at reference state (m^{2}s^{-1})
$D_{ij}{}^{eff}$	=	effective binary diffusivity of component i and j (m^{2}s^{-1})
D_λ	=	water diffusivity in Nafion membrane (cm^{2}s^{-1})
E_{eq}	=	Equilibrium fuel cell voltage (V)
F	=	Faraday's constant (96,485 C mol^{-1})
h	=	enthalpy of fluid flowing through the fuel cell (J/mol K)
i	=	current density (A m^{-2})
$\dot{I}$	=	local current density (A m^{-2})
i_0	=	exchange current density (A m^{-2})
$\bar{k}$	=	effective thermal conductivity (W m^{-1} K^{-1})
k_{eff}	=	effective thermal conductivity (W m^{-1} K^{-1})
k_{nf}	=	thermal conductivity of dry Nafion (W m^{-1} K^{-1})
k_w	=	thermal conductivity of water (W m^{-1} K^{-1})
M_w	=	molecular weight of water (kg kmol^{-1})
N	=	molar flux (mol m^{-2} s^{-1})
N_{H2O}	=	water molar flux (mol m^{-2} s^{-1})
n	=	number of electrons in rate determining step
n_{drag}	=	electro-osmotic drag coefficient ([H_2O]/[H^+])
n_{drag}^{SAT}	=	electro-osmotic drag coefficient at saturation level ([H_2O]/[H^+])
p	=	pressure (Pa)
P	=	Power (W)
p^{SAT}	=	Saturation vapor pressure of water (Pa)
R	=	gas constant (8.314 J mol^{-1} K^{-1})
ρ	=	fluid density (kg m^{-3})

LIST OF ABBREVIATIONS (Continued)

R_i	=	Reaction rate (mol m^3 s^{-1})
$\dot{S}_h$	=	entropy losses due to electrochemical reaction (J K^{-1})
$\Delta\hat{s}_{rxn}$	=	entropy of reaction (J mol^{-1} K^{-1})
T	=	temperature (K)
$\vec{u}$	=	velocity vector (m s^{-1})
V_{cell}	=	Fuel cell voltage (V)
w_i	=	mass fraction of specie i
x_i	=	mole fraction of specie i
α	=	charge transfer coefficient
β	=	reaction stoichiometry
ε	=	porosity
η	=	polarization losses
κ	=	permeability (m^2)
λ	=	membrane water content ($\frac{[H_2O]}{[SO_3^-]}$)
μ	=	viscosity (Pa·s)
σ	=	proton/electron conductivity (S cm^{-1})
σ_{303K}	=	proton/electron conductivity at 30°C (S cm^{-1})
φ	=	potential (V)

Subscript

a	=	the anode side
c	=	the cathode side
s	=	electrode region
m	=	membrane region
ion	=	ionic species
$elec$	=	electronic species

LIST OF ABBREVIATIONS (Continued)

R	=	reactant species
P	=	product species
w	=	water
act	=	activation loss
ohm	=	ohmic loss
con	=	concentration loss
$cross$	=	cross-over loss

superscript

*	=	at catalyst surface
ref,0	=	at reference state

SIMULATION OF MOMENTUM, HEAT, AND MASS TRANSFER IN A PROTON EXCHANGE MEMBRANE FUEL CELL

INTRODUCTION

Energy is fundamental to the quality of our lives. Since then, a vast array of energy devices and systems has been developed. A sustainable energy supply, both in the short- and the long-term, is needed for promoting both economic development and people's quality of life, as well as protecting the environment. Fuel cells provide a range of critical benefits. Fuel cells have received considerable attention lately for their potential to be clean and reliable devices for generating electricity. Cells will certainly be widely used in future decades.

A fuel cell has been considered as an efficient and clean alternative power source for automobile industry since the energy crisis forced people to find a substitution for fossil fuels. A proton exchange membrane fuel cell, also known as polymer electrolyte membrane fuel cell (PEMFC), becomes a prime candidate for applications in vehicles because of its following features: the PEMFC operates at a relative low temperature (less than 90°C); the PEMFC can start quickly; the PEMFC has a higher current density due to thin membrane electrodes assembly (MEA) compared to other types of fuel cells; and there are no corrosive fluid hazards since there is no liquid electrolyte present in the PEMFC.

Nevertheless, the wide application of a PEMFC is limited due to high capital cost, fuel availability, and durability etc. The difficulty of maintaining suitable thermal management and water management also affects the fuel cell performance significantly. For example, too much water produced on the cathode side will fill the pores of gas diffusion layers (GDLs), and therefore block the diffusion of reactants to reach the catalyst layer. Too little water on the anode side will dry up the membrane so that protons cannot migrate through it. Both cases result in a decrease in the cell output power.

Experimental research and numerical simulation have been used in fuel cell design in order to improve the performance of fuel cells. Experimental data is useful to validate the models. The computational models are efficient in predicting the cell performance under a variety of design parameters. Fuel cell models can be classified into 1D, 2D and 3D according to dimensions. The accuracy of 1D model (Springer *et al.,*1991), (Gurau *et al.,* 2000) is sacrificed due to some assumptions made in order to simplify the problem to 1D. A 3 D model simulates the reactant gas flow in the directions along the flow channel and perpendicular to the flow channel simultaneously, which results in more accurate results but requires longer computational time and larger computing capacity facility (Berning *et al.,* 2002). A 2D fuel cell model (Siegel *et al.,* 2003, Hwang, 2006, Guvelioglu and Stenger, 2007) combines the benefits of 1D and 3D models and gains its popularity in PEM fuel cell modeling due to its higher computational efficiency compared to 3D models and better simulation accuracy compared to 1D models. Now a day, PEMFC has been developed much. But the main problem is water management. Many researches deled with this problem in many ways. The most popular method is doing simulation to find the optimized condition to operate the best performance.

The main task of this work is to investigate the effects of different operating conditions on the performance of a high pressure drop across the channel. PEMFC using a two-dimensional (2-D) non-isothermal CFD model. This fuel cell model consists of the continuity, momentum and energy equations, the species transport equation, and the electrochemical reaction models. Begin with the study of the momentum, heat, and mass transfer in the GDL and membrane. The simulation result is investigated at operating condition of $80^{o}C$ with inlet pressure of 0.1 atm. The different operating conditions studied here in include the pressure drop of 0.1 atm, operating temperatures of $80^{o}C$, $70^{o}C$, and $60^{o}C$, back pressures of 1 atm, 2 atm and 3 atm. Then the simulation results compare with the experimental result from the 5 cm^2 PEMFC in KUCHE's laboratory (Leelasupakorn, H., 2008). In this work uses FEMLAB 3.0a for simulate the result. This CFD is based on finite element method. FEMLAB 3.0a can solve partial differential equation and couple the equations

together. The script setting for solved the problem to get the convergence solution is investigated.

OBJECTIVES

1. To simulate momentum, heat, and mass transport in a single cell PEMFC in 2D

2. To study the transport phenomena effects in flow channel, GDL, and surface of catalyst layer.

Scopes

1. Studying of the transport phenomena of fluid in flow channel, GDL, and surface of catalyst layer is done at steady-state condition.

2. Validation of prediction is made against available experimental data obtained from literature.

3. Simulation is done on a commercial software, FEMLAB 3.0a.

LITERATURE REVIEW

1. Fuel cell technology

Fuel cell is a device that takes fuel as input and produces electricity as output directly in one step. A fuel cell will continue to churn out product (electricity) as long as the fuel is supplied. This is the difference between a fuel cell and a battery. It is a cell which transforms the chemical energy stored in a fuel into electrical energy.

Combustion engines are another device that take the chemical energy stored in a fuel and transform it into useful mechanical energy which in turn can be transformed into electrical energy. It cannot produce electricity directly from chemical energy. In conventional combustion engine, fuel is burned, and releases heat. Consider, for example, the combustion of hydrogen:

$$H_2 + \frac{1}{2}O_2 \rightarrow H_2O \tag{1}$$

On the molecular scale, collisions between hydrogen molecules and oxygen molecules result in a reaction. The hydrogen molecules are oxidized, water is produced and the heat is released. To produce electricity, this heat must be converted into mechanical energy, and then the mechanical energy must be converted into electrical energy. Going through all these steps is potentially inefficient.

The fuel cell produces electricity in an alternative way. It can convert chemical energy to electrical energy directly. The hydrogen and oxygen reactants are separated so that the electron transfer necessary to complete the bonding reconfiguration occurs over a greatly extended length of distance. Then, as the electrons move from the fuel species to the oxidant species to complete the reaction, they can be harnessed as an electrical current.

Similar to combustion engines, fuel cell can produce electricity as long as they are supplied with fuel. Comparing to the batteries, fuel cells are electrochemical

energy conversion devices that rely on electrochemistry. Therefore, fuel cells share some common characteristics with primary batteries.

Direct production of electricity using fuel cell is far more efficient than combustion engines. Fuel cells can be all solid state and mechanically ideal, meaning no moving parts. This yields the potential for highly reliable and long-lasting systems. A lack of moving parts means that fuel cells are silent. Also, undesirable products such as NO_x, SO_x, and particulate emissions are virtually zero.

Fuel cells offer potentially higher energy densities than batteries and can be quickly restarted by refueling, whereas batteries must be thrown away or plugged in for a time-consuming recharging.

An advantages of fuel cell is a zero-emission power source, high efficiency, high reliability, and flexibility. Fuel cell is operated with pure hydrogen, therefore it produces less emissions than conventional power plants. Because they make energy electrochemically, fuel cells are more efficient than combustion systems. The ability to produce continuous power makes fuel cells well suited for supporting critical loads or emergency applications. Fuel cells operate with hydrogen and continue to generate power as long as fuel is supplied.

While fuel cells present interesting advantages, they also provide some serious disadvantages. Cost represents a major barrier to fuel cell implementation. Power density is another significant limitation. Fuel cell needs more improvements if they are to compete in portable and automotive applications. Combustion engines with liquid fuels and batteries in combinations generally outperform fuel cells on a volumetric power density basis. On a gravimetric power density basis, the race is much closer. The power density comparison of selected technologies is shown in **Figure 1**.

Fuel availability and storage pose further problems. Fuel cell work best on hydrogen gas, a fuel that is not widely available, has a low volumetric energy density,

and is difficult to store. An energy comparison of selected fuels was shown in **Figure 2**.
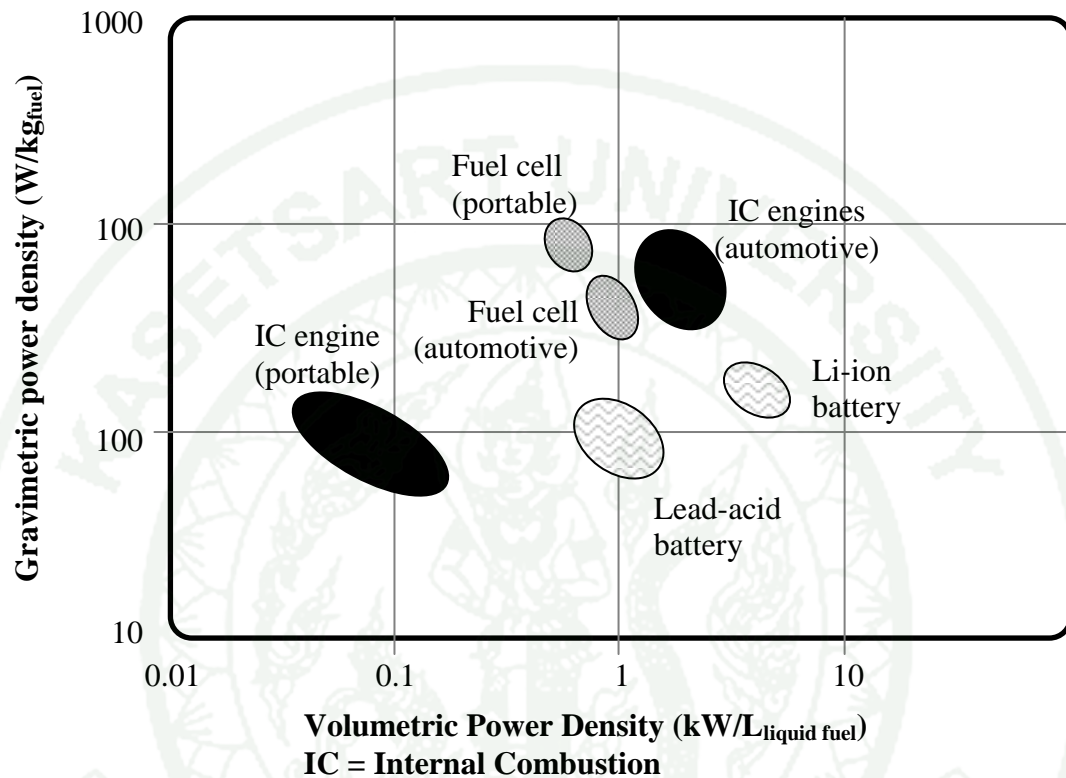
Figure 1 Power density comparison of selected technologies (approximate ranges).

Source: O'Hayre *et al.* (2009)

An another fuel cell limitations include operational compatibility concerns, susceptibility to environmental poisons, and durability under start-stop cycling. These significant disadvantages will not be easy to overcome. Fuel cell adoption will be severely limited unless technological solution can be developed to overcome these problems.

There are five major types of fuel cell, differentiated from one another by their electrolyte. The summarized of fuel cell types is shown in **Table 1**. There are five major types of fuel cells, classified by the manner of their electrolyte. The

phosphoric acid fuel cell (PAFC) employs liquid H_3PO_4 electrolyte. PAFC can be operated at moderated temperature ($200^{o}C$) with excellent reliability but the liquid electrolyte must be replenished during operation. The polymer electrolyte membrane fuel cell (PEMFC) is constructed from a proton-conducting polymer electrolyte membrane. It provide the highest power density of all the fuel cell with good start-stop competency. Because of low-temperature operation ($80\text{-}100^{o}C$), PEMFC is suitable for portable application. The water management and the components cost of PEMFC, however, are important problems must be resolved. Alkaline fuel cell (AFC) with liquid KOH electrolyte can operated at moderated temperature ($60\text{-}220^{o}C$). The limitation of AFC is pure $H_2\text{-}O_2$ usage and water management. The electrolyte in molten carbonate fuel cell (MCFC) is a molten mixture of alkali carbonates, Li_2CO_3 and K_2CO_3, immobilized in a $LiOAlO_2$ matrix. The relatively high operating temperature ($650^{o}C$) provides fuel flexibility. MCFC can run on hydrogen, hydrocarbon, and alcohol. Solid oxide fuel cell (SOFC) employs a solid ceramic electrolyte. Due to high operating temperature ($600\text{-}1000^{o}C$), SOFC has high efficiency while it need relatively expensive equipments.

The fuel cell can be applied to with every kind of electronic and electrical devices. Fuel cell with the size of a printer could provide enough electric current to equivalent to a combustion engine. Fuel cells also offer the possibility of application to laptops and cell phones with energy life measured in days or weeks. It is scalable, which means it can go small enough to power medical devices. In a large scale stationary power production, fuel cell could provide a backup power supplied in a necessary places such as hospitals and airports.

In this work, the simulation of proton exchange membrane fuel cell (PEMFC) was developed. PEMFC is attractive for many applications because they operate at low temperature and have high power density.
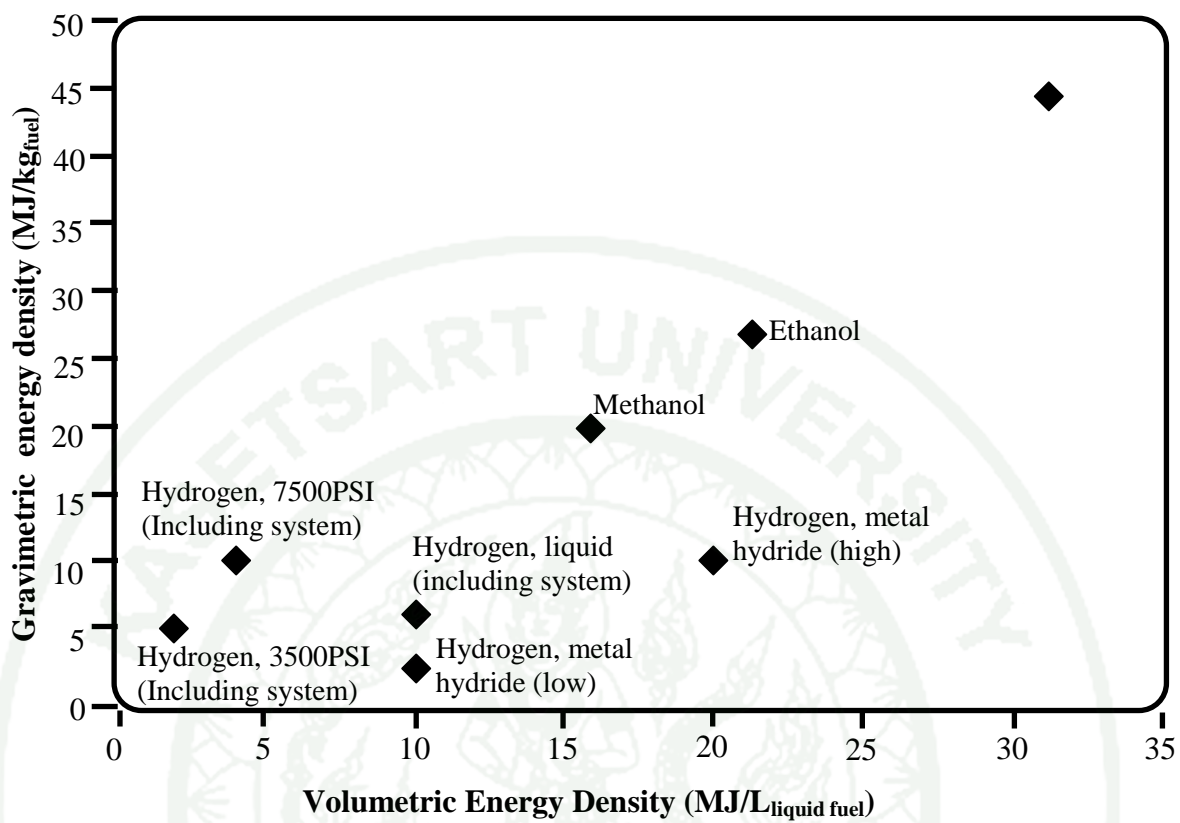
Figure 2 Energy density comparison of selected fuels (lower heating value)

Source: O'Hayre *et al.* (2009)

Table 1 The description of Fuel Cell Types

	PEMFC	PAFC	AFC	MCFC	SOFC
Electrolyte	Polymer membrane	Liquid H_3PO_4	Liquid KOH	Molten carbonate	Ceramic
Charge carrier	H^+	H^+	OH^-	CO_3^{2-}	O^{2-}
Operating temperature	80^oC	200^oC	$60\text{-}220^oC$	650^oC	$600\text{-}1000^oC$
Catalyst	Platinum	Platinum	Platinum	Nickel	Perovskite (ceramic)
Structure components	Carbon based	Carbon based	Carbon based	Stainless based	Ceramic based
Fuel compatibility	H_2, Methanol	H_2	H_2	H_2, CH_4	H_2, CH_4, CO

Source: O'Hayre *et al.* (2009)

2. Proton Exchange Membrane Fuel Cell (PEMFC)

A. Overview

The PEMFC is a fuel cell that use a proton-conducting polymer membrane, usually a perfluorinated sulfuric acid polymer, as electrolyte. The anode and cathode reactions in the PEMFC are

Anode (Oxidation Reaction): $\qquad H_2 \rightarrow 2H^+ + 2e^-$ $\qquad$ (2)

Cathode (Reduction Reaction): $\qquad \frac{1}{2}O_2 + 2H^+ + 2e^- \rightarrow H_2O$ $\quad$ (3)

Overall Reaction (Redox Reaction): $\quad H_2 + \frac{1}{2}O_2 \rightarrow H_2O$ $\qquad$ (1)
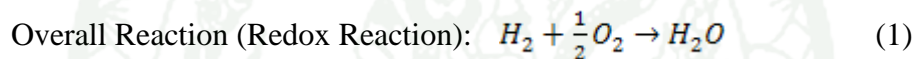
A schematic diagram of a PEMFC is provided in **Figure 3**. The hydrogen is fed at anode bipolar plate (or flow field) and then diffuse through anode gas diffusion layer. The oxidation reaction takes place at platinum catalyst surface and produce two protons and two electrons per one hydrogen molecule. The produced protons move through the proton conducting membrane while the produced electron move out to external electrical circuit. Oxygen gas, fed at cathode side, reacts with proton and electron from anode side to produce the water molecule and complete reduction reaction. Hydrogen and oxygen left over from electrochemical reaction through gas diffusion layer to bipolar plate flow channel on respective sides and are removed out from PEMFC. The water molecules are also removed out from PEMFC through the same way.

The polymer membrane employed in PEMFC is a proton conducting material which allows only proton can transport through it. It is constructed from polymer with anion functional group. The platinum catalyst is coated on both sides of membrane. Then they are sandwiched with porous carbon support material. This structure is referred to as a membrane electrode assembly (MEA). The operating

temperature of the PEMFC is limited to under 100°C and lower because the polymer membrane must be hydrated with liquid water to maintain adequate proton conductivity. Because of the low operating temperature, platinum are the only practical catalysts currently available.
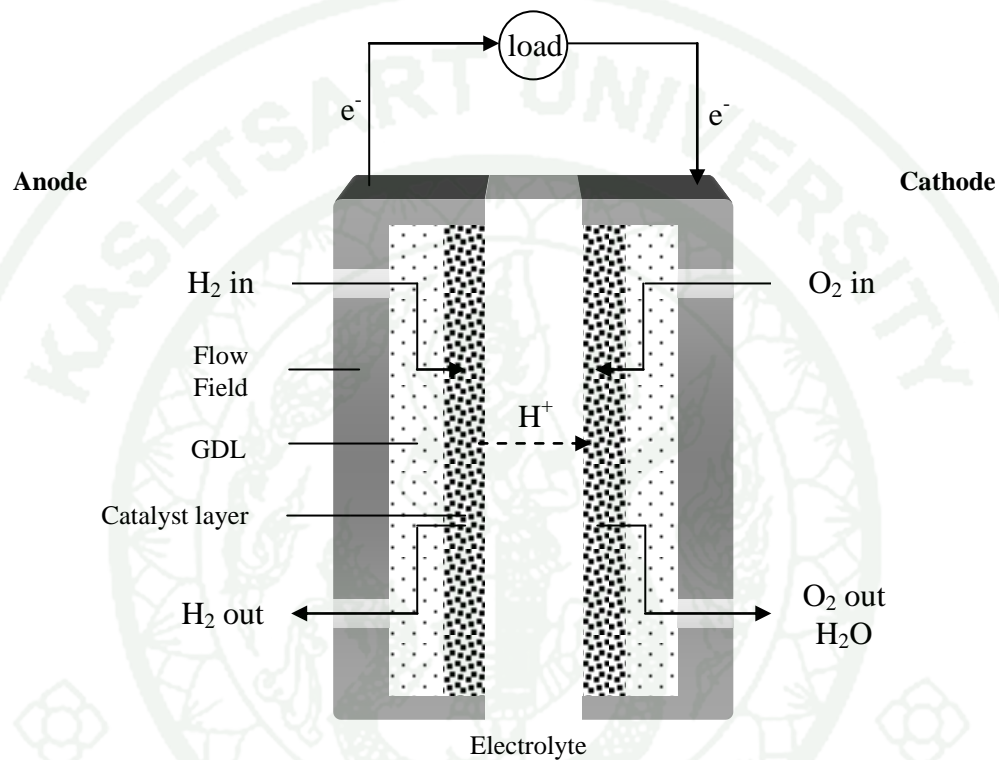
Figure 3 Schematic of proton exchange membrane operation

B. Advantages and disadvantages of PEMFC comparing with other types of fuel cells

PEMFC advantages

      - Highest power density of all the fuel cell classes

      - Good start-stop capabilities (easy to start and stop)

      - Low-temperature operation makes it suitable for portable applications

PEMFC disadvantages

- Uses expensive platinum catalyst
- Polymer membrane and ancillary components are expensive
- Active water management is often required
- Very poor carbon monoxide and sulfur tolerance

C. PEMFC components

To make the fuel cell works, various components are fabricated and assembled together as shown in **Figure 4**. They are:
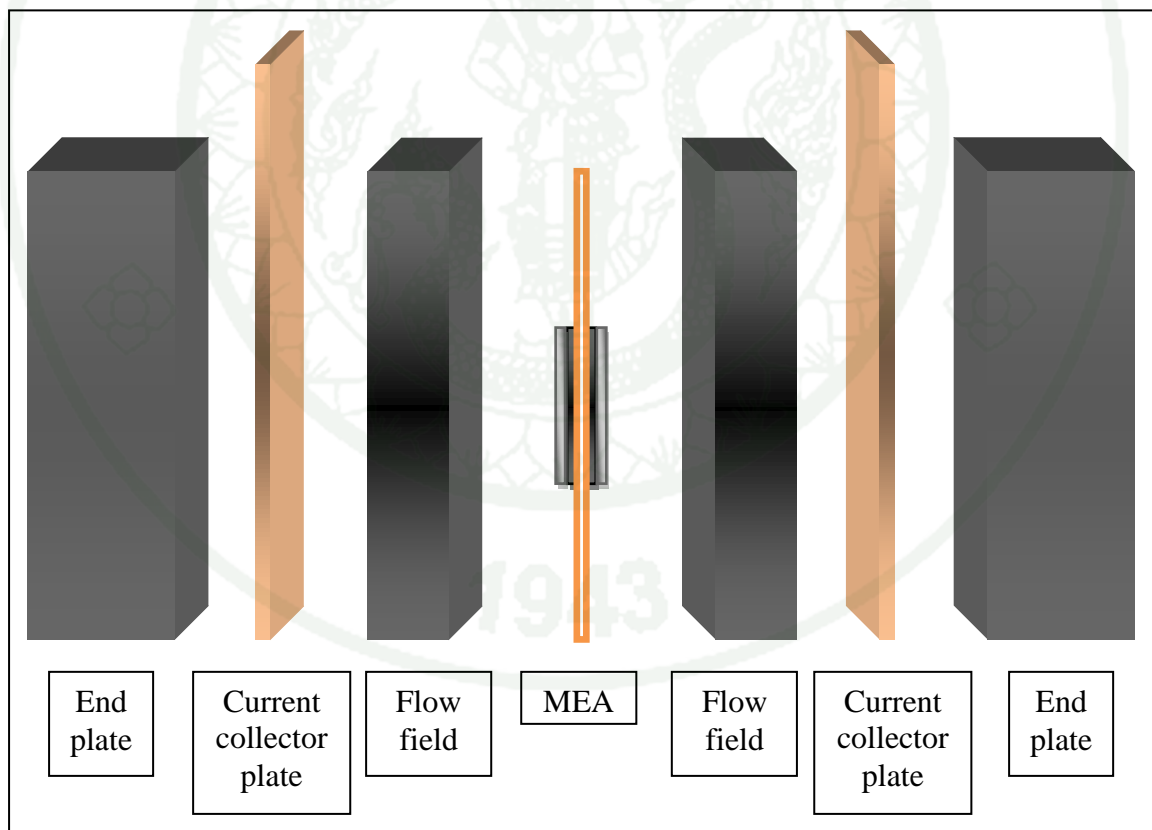
Figure 4 The components of PEMFC

1. Membrane Electrode Assembly (MEA)

The heart of a proton exchange membrane fuel cell is the membrane electrode assembly. It consists of electrolyte membrane coated with catalyst such as platinum on each side. The catalyst coated membrane is sandwiched between gas diffusion layer (GDL). The schematic diagram of MEA is shown in **Figure 5**. The reactant gases from the flow fields diffuse through the gas diffusion layers to the catalyst layers, and then react at the catalyst surfaces. The proton is produced on the side that is fed with hydrogen (anode) and diffuses through the membrane to another side which is fed with oxygen (cathode). The electrons cannot pass through the membrane, thus go along the conducting wire outside the fuel cell to reach the cathode and produce the electrical current. The proton reacts with oxygen and recombines with electron at the cathode and produces water. The product water is removed from the cathode catalyst surface by diffusion through the GDL on the cathode side. Thus, the performance of PEMFC depends on the MEA significantly. The MEA comprises of various layers as follow:
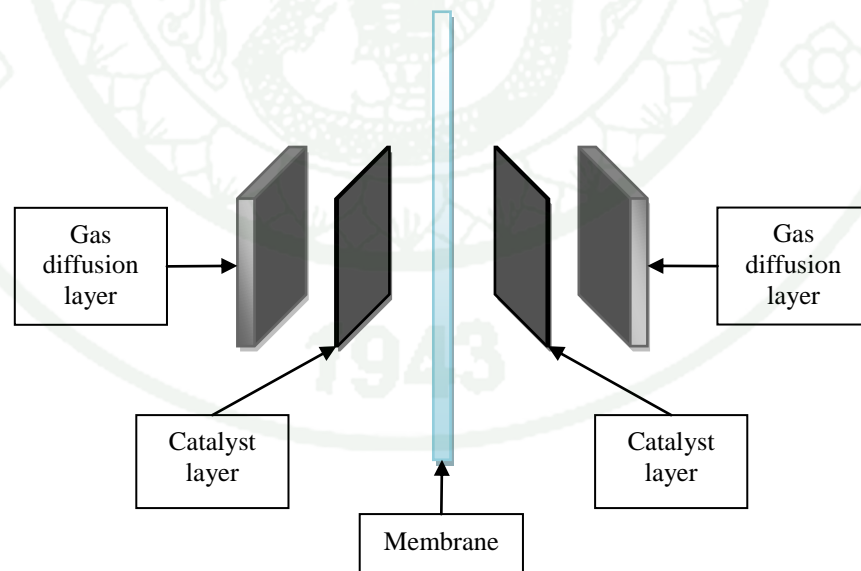
Figure 5 The component of membrane electrode assembly

a) Membrane

The membrane is the part that separates the reduction and oxidation reactions. It allows proton to pass through and completes the overall reaction while forcing the electron to pass through an external circuit. The perfluorosulfonic acid (PFSA) is the most commonly used membrane material for PEM fuel cell. PFSA consists of three regions: (a) The Teflon-like fluorocarbon backbone with hundreds of repeating $-CF_2-CF-CF_2-$ units in length, (b) the side chains of $-O-CF_2-CF-O-CF_2-CF_2-$ which connect the molecular backbone to the third region, and (c) the ion clusters consist of sulfonic acid ions, $SO_3^-H^+$. When the membrane becomes hydrated, the hydrogen ions in the third region become mobile by bonding to the water molecules and moving between sulfonic acid sites as shown in **Figure 6**. The thickness of a membrane in a membrane electrode assembly can vary with the type of membrane.
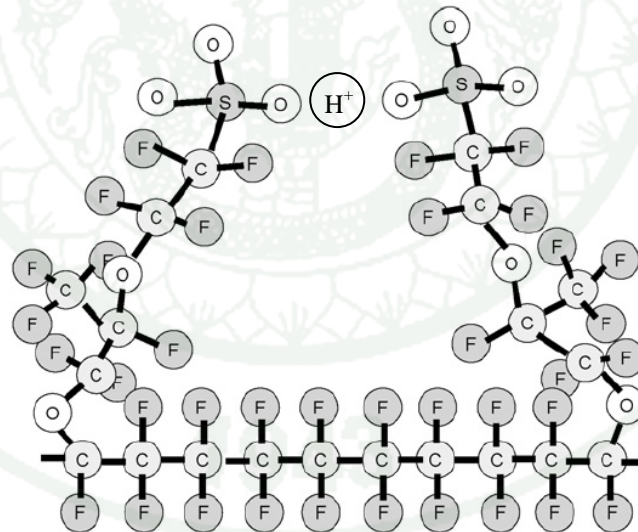
Figure 6 Schematic of Nafion® structure

Source: Vayenus *et al.* (2007)

The properties of electrolyte membrane, such as proton conductivity, diffusion coefficient, and thermal conductivity, are a function of membrane water

content, λ, which is defined as the ratio of number of water molecules per sulfonate molecules,

$$\lambda = \frac{[H_2O]}{[SO_3^-]} \qquad (4)$$

The membrane water content, λ, at the surface of membrane is determined by the water activity, a_w, at the electrode/membrane interface. The water activity is defined as a ratio of vapor pressure of water in a system to the saturation pressure of pure water at equal temperature.

$$a_w = \frac{x_w p}{p_{sat}} \qquad (5)$$

where x_w is mole fraction of water, p is local pressure, and p_{sat} is saturation pressure.

An experiment was done with Nafion[®] 117 at 30°C to determine the effect of water vapor activity on membrane water content. The membrane was equilibrated in a closed chamber with aqueous LiCl solution of known a_w. The measured membrane water content was plot versus water activity, called isopiestic curve. The result is shown in Figure 6. The value of λ is 14 for fully hydrated Nafion[®] (Zawodzinski et al., 1991). Later on, the relationship of membrane water content and water activity was developed and compared to the experimental result at 80°C and 100°C where λ are 16.8 and 22 for fully hydrated Nafion[®] 117 respectively (Springer et al., 1991). Assumed that the membrane water content increase linearly from 14 to 16.8 as the mole fraction of water exceeded the saturation value at 30°C. The mole fraction of water increases from $x_{w,sat}$, 30°C to $3x_{w,sat}$, 30°C. The correlations are as follow.

$$\lambda = \begin{cases} 0.043 + 17.81a_w - 39.85a_w{}^2 + 36.0a_w{}^3 & for\ 0 \le a_w \le 1 \\ 14 + 1.4(a_w - 1) & for\ 1 < a_w \le 3 \end{cases} \qquad (6)$$

In Nafion® 117, the number of water molecules dragged per proton or electroosmotic drag, n_{drag}, was found to be 2.5 ± 0.2 for a fully hydrated membrane in equilibrium with liquid water at 30-50°C. Assume the water drag coefficient is linearly proportional to water content. The number of water molecules per proton, n_{drag}, is defined as (Springer et al., 1991)

$$n_{drag} = n_{drag}^{SAT} \frac{\lambda}{22} \qquad (7)$$
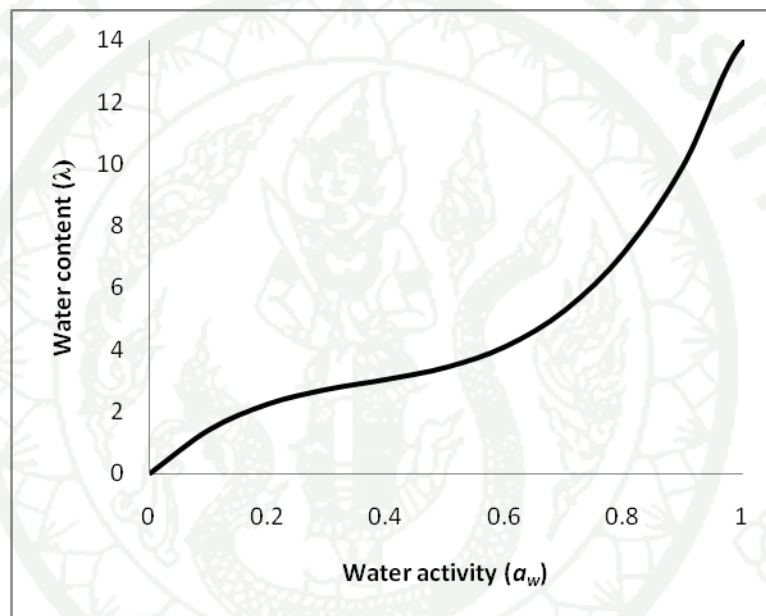
Figure 7 Measured membrane water content vs. water activity of Nafion® 117 at 30°C and correlation result.

When water diffuses back from cathode to anode through the membrane, its diffusivity in Nafion®, D_λ, is a function of water content, λ. For $\lambda > 4$, a model is represent as: (Springer et al., 1991)

$$D_\lambda = 10^{-6} \exp\left[2416 \left(\frac{1}{303} - \frac{1}{T} \right) \right]$$
$$\times (2.563 - 0.33\lambda + 0.0264\lambda^2 - 0.000671\lambda^3) \qquad (8)$$

where D_λ is in cm^2/s. For $\lambda < 4$, the extrapolated values from **Figure 8** should be used instead.
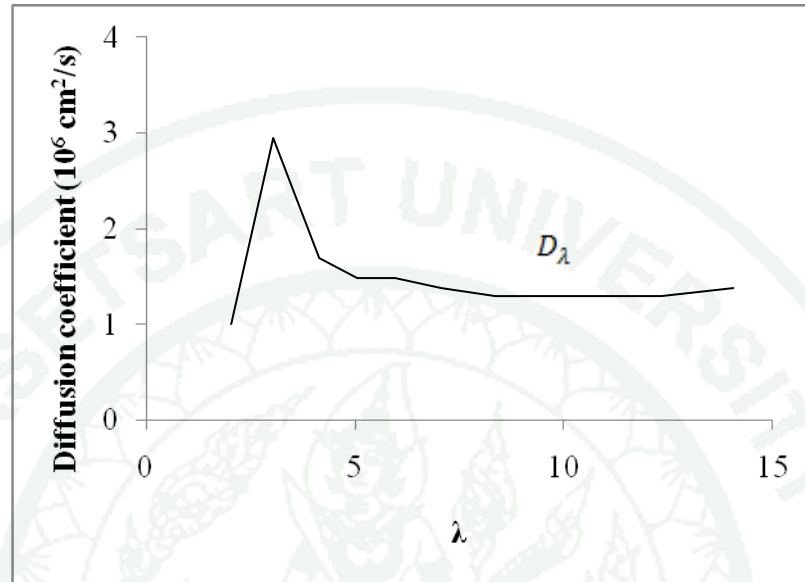
Figure 8 Water diffusivity, D_λ, in Nafion$^®$ versus water content λ at 303 K

Source: Springer *et al.* (1991)

The Nafion$^®$ membrane proton conductivity, σ, is a function of membrane water content and temperature. The correlation is: (Springer et al., 1991)

$$\sigma(T, \lambda) = \sigma_{303K}(\lambda)\exp\left[1268\left(\frac{1}{303} - \frac{1}{T}\right)\right] \qquad (9)$$

where σ is a proton conductivity (S/m), T is temperature (K), and $\sigma_{303K}(\lambda)$ is defined as

$$\sigma_{303K}(\lambda) = 0.005193\lambda - 0.00326 \qquad \text{for } \lambda > 1 \qquad (10)$$

The thermal conductivity of Nafion$^®$ membrane, k^{eff}, based on a steady state measurement method of dry Nafion$^®$ membrane over a range of temperatures from 17 to 65°C. It was observed that the thermal conductivity decreases

inversely with temperature. This phenomena results from the phonon transport behavior. When temperature is increased, the phonon mean free path decreases. Thus the thermal conductivity, which is proportional to the mean free path, decreases inversely with temperature (Choy et al., 1999).

The effect of humidity on thermal conductivity of the Nafion® membrane can be theoretically estimated by the volume averaging method. The thermal conductivity of a humidified membrane can be estimated as

$$k^{eff} = \frac{(\lambda/\rho_w)k_w + (1/c_{SO_3} - M_w)k_{nf}}{1/c_{SO_3} - M_w + \lambda/\rho_w} \tag{11}$$

where λ is the water content in Nafion® (mol H_2O/mol SO_3^{-1}), ρ_w the density of liquid water (kg m^{-3}), k_w the thermal conductivity of liquid water (W m^{-1} K^{-1}), M_w the molecular weight of water (kg kmol^{-1}), k_{nf} and is the thermal conductivity of dry Nafion® membrane (W m^{-1} K^{-1}). The estimated variation of thermal conductivity of humidified Nafion® membrane with temperature was calculated, and is shown in **Figure 9**.

b) Catalyst layer

All electrochemical reactions in a fuel cell consist of two separate reactions: an oxidation half-reaction at the anode and a reduction half-reaction at the cathode. Normally, the two half-reactions would occur very slowly at the low operating temperature of the PEM fuel cell. Thus each of the membrane is coated on one side with a catalyst layer, usually made of platinum powder, that speeds up the reaction of oxygen and hydrogen. The catalyst is rough and porous so that the maximum surface area of the platinum can be exposed to the hydrogen or oxygen. The platinum-coated side of the catalyst faces the membrane. Platinum-group metals are critical to catalyzing reactions in the fuel cell, because platinum is unique and it is sufficiently reactive in bonding H and O intermediates as required to facilitate the electrode processes, and also capable of effectively releasing the intermediate to form

the final product. However platinum is very expensive material. The thickness of the catalyst layers depends upon how much platinum (Pt) is used in each electrode. Therefore, the goal of this research is to reduce the use of platinum in PEM fuel cell.
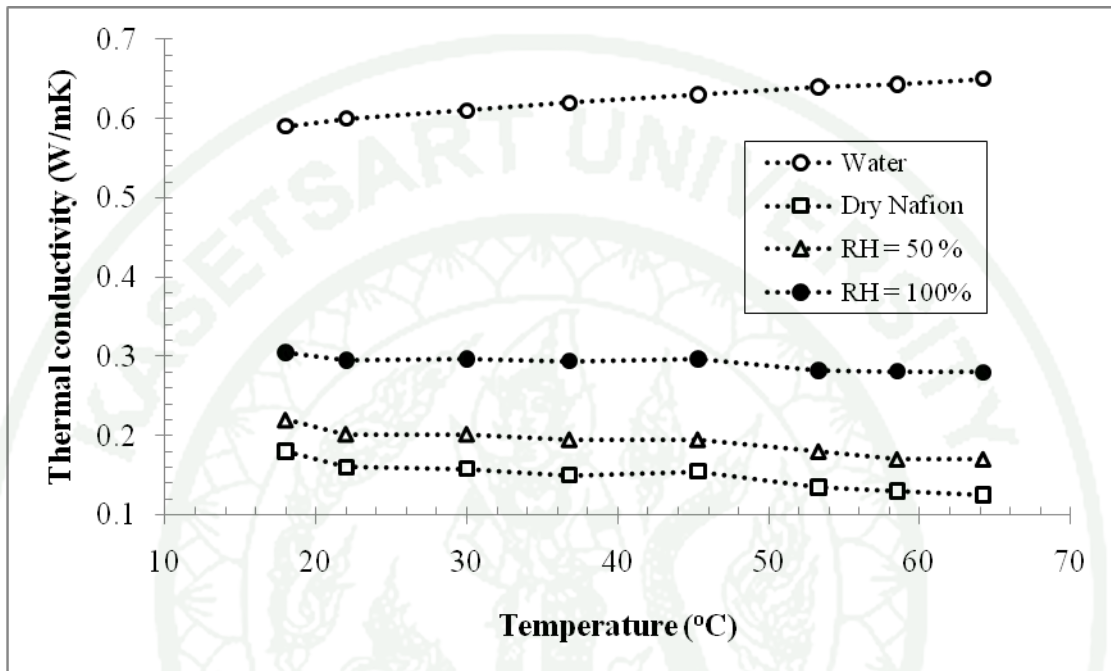
Figure 9 Estimated thermal conductivity of Nafion® 112 and 117 at different humidity ratios. The thermal conductivity variation of pure water is shown as an upper bound for the theoretical moist Nafion® thermal conductivity.

Source: Khandelwal and Mench (2006)

c) Gas Diffusion Layer (GDL)

The GDL, one next to the catalyst anode and the other next to the catalyst cathode, gas diffusion layers are typically fabricated from porous conductive carbon-based materials. The structure allows the gas to spread out as it diffuses so that the gas will be in contact with the entire surface area of the catalyzed membrane. The most common materials are carbon cloth with a layer of carbon powder bonded to it and carbon paper, typically 100-300 μm thick. The micrograph of gas diffusion layer

is shown in **Figure 10.** In this study, the SIGRACET GDL 10 BA from SGL Technologies was used. The properties of GDL for SIGRACET 10 BA are shown in **Table 2**.
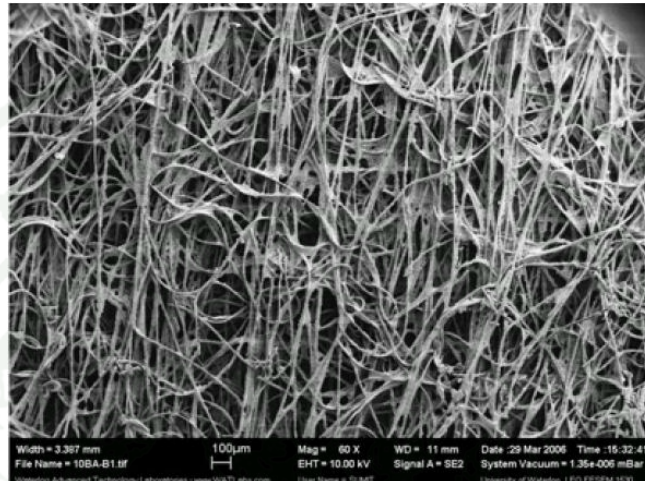
Figure 10 Micrograph of SIGRACET GDL 10 BA.

Table 2 Properties of SIGRACET GDL 10BA

GDL type	Thickness (μm)	Porosity (%)	Electronic Resistance (Through plane), (mΩcm^2)
SIGRACET GDL 10BA	400	88	<12

Source: SGL Technologies

The GDL thermal conductivity was experimentally measured by Khandelwal et al. (2006). The effect of PTFE content on diffusion media thermal conductivity was reported in **Table 3**. It was observed that thermal conductivity decreases with increasing PTFE content. Since the thermal conductivity of PTFE (11.7 W m^{-1} K^{-1}) is lower than carbon fibers (129 W m^{-1} K^{-1}), the thermal conductivity of the PTFE treated diffusion media reduce.

Table 3 The thermal conductivity of GDL with differences PTFE loading

Material	Measured thermal conductivity, $(W\ m^{-1}\ K^{-1})$
SIGRACET 0 wt.% PTFE (AA series at 56°C)	0.48 ±0.09
SIGRACET 5 wt.% PTFE (BA series at 58°C)	0.31±0.06
SIGRACET 20 wt.% PTFE (DA series at 58°C)	0.22±0.04

Source: Khandelwal *et al.* (2006)

3. Flow field with flow channel

The bipolar plate is made of graphite or metal, that is a strong, gas-impermeable and electron conducting material. The channels are used to carry the reactant gas from the point at which it enters the fuel cell to the point at which the gas exits. Flow fiend design also affects water supply to the membrane and water removal from the cathode.

4. Current collector plate

A current collector plate is a flat plate located between a flow field and end plate, see **Figure 4**. It contacts directly to a flow field while it is separated from the end plate with Teflon sheet. The current collector plate conducts current from cathode, through external circuit to anode. It is made of high electric conducting material such as copper.

5. End plate

The parts which hold all of the parts of the fuel cell together is called end plate. The end plate articulate each fuel cell parts with compressing force. It made from a metal such as aluminum or stainless steel.

3. Fuel Cell Operation

The cross-sectional view of a planar fuel cell is shown in **Figure 11**. The steps involved in producing electricity in fuel cell consist of these steps as follows:

1. Reactant transport into the fuel cell
2. Electrochemical reaction
3. Ionic conduction through the electrolyte and Electron conduction through the external circuit
4. Product removal from the fuel cell

Step 1 Reactant transport into the fuel cell: The reactants are fed to the gas flow channel on each side. After that, its diffuse through the gas diffusion layer to the catalyst layer. A concentration of reactant at catalyst surface depends on how the reactant transport into the fuel cell. It is affected form the flow channel configuration and gas diffusion layer characteristics.

Step 2 Electrochemical reaction: The reactants reach the catalyst. After that the electrochemical reactions take place. The current generated is related to how fast the electrochemical proceed.

Step 3   Ionic and Electronic conduction: The electrochemical reactions occurring in step 2 either produce or consume ions and electrons. Ions produced at one electrode must be consumed at the other electrode. The same holds for electrons. To maintain charge balance, these ions and electrons must be transported from the

locations where they are generated to the locations where they are consumed. For electrons this transport process in rather easy. As long as an electrically conductive path exists, the electrons will be able to flow from one electrode to the other.

Step 4 Product removal: The product from the electrochemical reaction, such as water, carbon dioxide, etc., can be strangled the fuel cell if it is not removed out. The new fuel and oxidant are unable to react at catalyst surface. This can be a major issue in PEMFC's problem called "flooding".
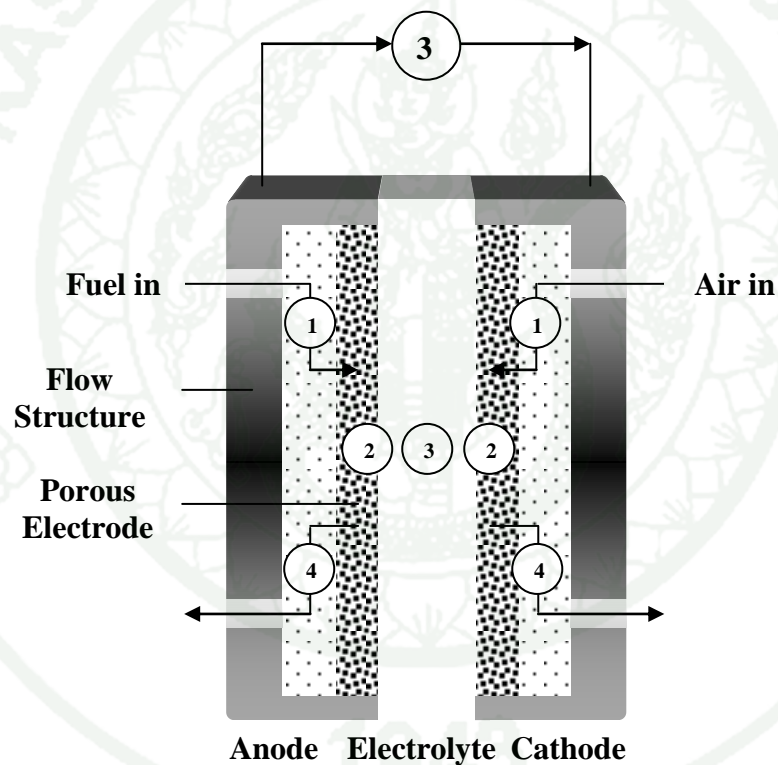
Figure 11   Cross-section of fuel cell illustrating major steps in electrochemical generation of electricity: step 1 Reactant transport, step 2 electrochemical reaction, step 3 ionic and electronic conduction, step 4 product removal.

4. Fuel cell performance

The performance of a fuel cell can be summarized in a plot of its current-voltage characteristics. This plot, called polarization curve, shows the voltage output of the fuel cell for a given current output. A typical polarization curve for a PEMFC is shown in **Figure 12**. The current has been normalized by the active area of fuel cell, giving a current density, i, A m^{-2}.

An ideal fuel cell would supply any amount of current while maintaining a constant voltage determined by thermodynamics. In practice, however, the actual voltage output of a real fuel cell is less than the ideal thermodynamically predicted voltage. The more current that is drawn from a real fuel cell, the lower the voltage output from the fuel cell, limiting the total power that can be delivered. The power, P, delivered by a fuel cell is given by the product of current density and voltage:

$$P = iV_{cell}$$ (12)

where P is power density (W/m^2), i is current density (A/m^2) and V_{cell} is fuel cell voltage (V). The combined fuel cell polarization and power density curves is shown in **Figure 13**. Fuel cell power density increases with increasing current density, reaches a maximum, and then falls at still higher current densities. Fuel cell is designed to operate at or below the power density maximum. At current densities below the power density maximum, voltage efficiency improves but power density falls. At current densities above the power density maximum, both voltage efficiency and power density fall.

The voltage output of a real fuel cell is less than thermodynamically predicted voltage output due to irreversible losses. The more current is drawn from the cell, the greater decreasing of voltage output. Each of these losses is associated with these steps discussed in the next section:

1. Activation losses (losses due to electrochemical reaction)
2. Ohmic losses (losses due to ionic and electronic conduction)
3. Mass transport losses (losses due to mass transport)
4. Cross-over losses (losses due to hydrogen cross-over and internal current short circuit)
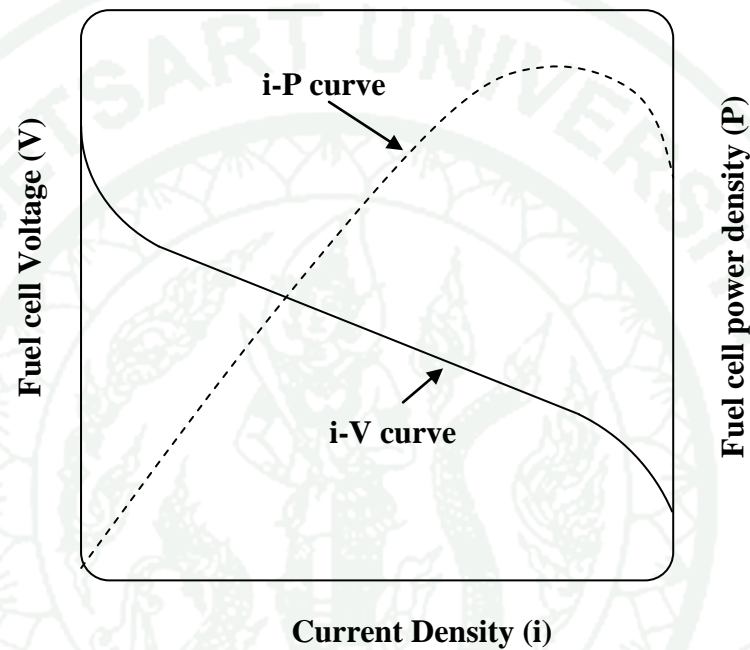
Figure 12 Combined fuel cell polarization curve and power density curve.

The real voltage output for a fuel cell can thus be written by starting with thermodynamically predicted voltage output of the fuel cell and then subtracting the voltage drops due to the various losses:

$$V_{cell} = E_{eq} - \eta_{act} - \eta_{ohm} - \eta_{con} - \eta_{cross} \qquad (13)$$

where V is real output voltage of fuel cell, E_{eq} is thermodynamically predicted fuel cell voltage output, η_{act} is activation losses due to reaction kinetics, η_{ohm} is ohmic losses from ionic and electronic condition, η_{con} is concentration losses due to mass transport and η_{cross} is losses due to reactant gases cross-over and internal short circuit of electron.
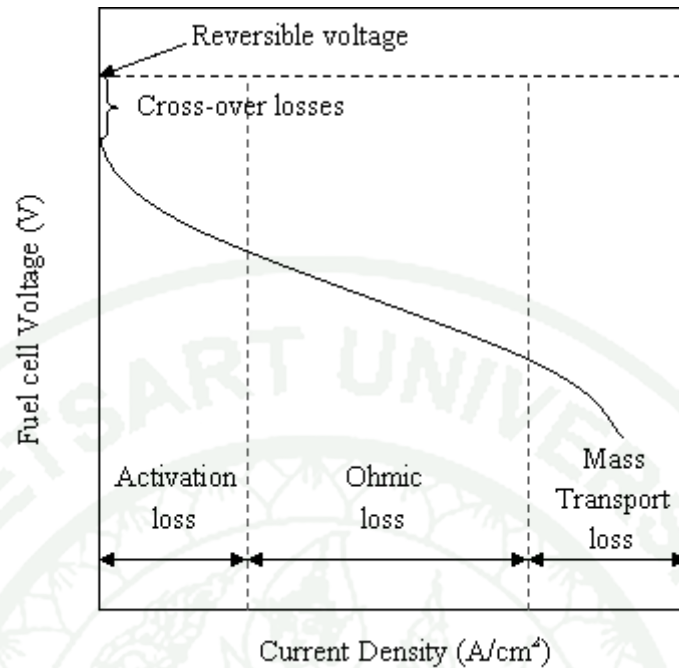
Figure 13 Polarization curve of fuel cell with the four major types of fuel cell losses: activation losses, ohmic losses, mass transport losses and cross-over losses.

5. Fuel cell modeling and simulation

Modeling are pivotal to the development and advancement of fuel cell technology. The simulation and modeling study allow us to better understand how fuel cells work, cover the way toward further improvements.

Fuel cells convert chemical energy directly into electricity via electrochemical reaction at cathode and anode sides. In PEMFC, hydrogen flows into the flow channel and diffuses through the gas diffusion layer (GDL) to the anode electrode. Catalyst particles facilitate fuel oxidation into protons and electrons. The hydrogen oxidation reaction is

$$H_2 \rightarrow 2H^+ + 2e^- \tag{2}$$

Protons migrate through the polymer electrolyte membrane (PEM). Electrons reach the cathode side over bipolar plates and external circuit (load) where power can be drawn. On cathode side, oxygen diffuses into the catalyst layer and is electrochemically combined with protons and electrons according to reduction reaction

$$\frac{1}{2}O_2 + 2H^+ + 2e^- \rightarrow H_2O \tag{3}$$
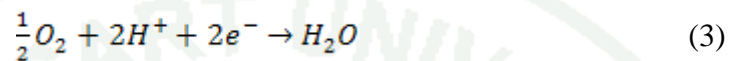
Both equations are called half-cell reactions, equations (2) and (3), do not describe the entire physical phenomenon occurring within a PEMFC. Many more equations for adequate momentum, heat, mass and charge transfers modeling are needed.

A. PEMFC modeling equations

1. Darcy's law

Darcy's law is used for modeling the flow in porous media with a pressure gradient as a driving force. In a porous structure, the global transport of momentum by shear stresses in the fluid is negligible because the pore walls impede transport of this momentum to the fluid outside the individual pores. Because a detailed description at the resolution of the porous and fluid media is a common approach. Darcy's law is based upon homogenization of the porous and fluid media into one single medium and does not required a detailed geometrical description of the pore structure.

Darcy's law states that the velocity field is determined by the pressure gradient, the fluid viscosity, and the structure of the porous media

$$u = -\frac{\kappa}{\mu}\nabla p \tag{14}$$

where u is fluid velocity vector (m/s), κ is permeability of porous media (m^2), μ is viscosity of fluid (Pa·s) and p is a pressure (Pa).

The permeability of gas diffusion layer was measured in three perpendicular directions by Gostick et al. The in-plane permeability was foundto be twice as high as the through-plane value which is in agreement with Ihonen et al. findings. The permeability of SIGRACET GDL 10BA is shown in **Table 4.**

Table 4 The permeability (κ) of SIGRACET GDL 10BA

Material	In-plane permeability (m^2)	Through-plane permeability (m^2)
SIGRACET GDL 10BA	5.3 x 10^{-11}	3.74 x 10^{-11}

Source: Gostick *et al.* (2002)

The viscosity is a measurement of the resistance of a fluid which is being deformed by either shear stress or tensional stress. In PEMFC, the viscosities at anode and cathode side must be determined as a mixture of reactant gas and water from humidified processes. However, there are an approximate equation proposed by R.C. Reid, J.M. Prausnitz and B.E. Poling. The viscosities of gases mixture is assumed to be a function of temperature only. At anode side, the fluid viscosity is

$$\eta_a = 1.378 \times 10^{-5} \left(\frac{T}{298}\right)^{1.02} \qquad (15)$$

and at the cathode side, the viscosity is

$$\eta_c = 1.094 \times 10^{-5} \left(\frac{T}{298}\right)^{1.05} \qquad (16)$$

where η is the viscosity of fluid (Pa · s) and T is local temperature (K). The subscript a and c refer to anode and cathode side, respectively.

2. Mass Conservation

For multi-component diffusion in gasses at low density, the Stefan-Maxwell is a good approximation.

$$\nabla x_i = -\sum_{j \neq i}^{N} \frac{(x_j N_i - x_i N_j)}{c D_{ij}} \tag{17}$$

where D_{ij} is the binary diffusivity of component i and j (m^2 s^{-1}), c is the concentration (mol m^{-3}), x_i is the mole fraction of component i, and N_i is the molar flux vector of component i (mol m^{-2} s^{-1}). The combination between mass balance equation and Stefan-Maxwell diffusion was derived by Curtiss and Bird (1999).

$$\frac{\delta \rho w_i}{\delta t} + \nabla \cdot \left(-\rho w_i \sum \left(D_{ij} \nabla x_j + (x_j - w_j) \frac{\nabla p}{p} \right) + \rho w_i u - D_i^T \frac{\nabla T}{T} \right) = R_i \tag{18}$$

The first term on the left hand side is an accumulation of specie i. Second term is the diffusion term due to concentration and pressure gradient. Third is convection term and forth is thermal diffusion term. The last term on the right hand side is reaction term.

Experimentally obtained binary diffusivities, $D_{ij}^0(T_0, p_0)$ at atmospheric pressure p_0 and reference temperature T_0 shown in **Table 5** are scaled to operating temperature and pressure according to (Berning, T., 2003)

$$D_{ij} = D_{ij}^0(T_0, p_0) \frac{p_0}{p} \left(\frac{T}{T_0} \right)^{1.5} \tag{19}$$

Since the porous structure of the electrodes the binary diffusivities need to be corrected for the porosity ε of the electrode media. This is done with the Bruggeman correlation (Bernardi, D.M., 1992)

$$D_{ij}^{eff} = D_{ij}\varepsilon^{1.5} \tag{20}$$

where D_{ij}^{eff} is effective binary diffusivity (m²/s), D_{ij} is binary diffusivity (m²/s) and ε is porosity.

Table 5 Binary diffusivities and reference temperatures at 1 atm

Gas pair	Reference temperature T_0 (K)	Binary diffusivity D_{ij}^0 (m²s⁻¹)
$D_{H_2-H_2O}^0$	307.1	9.15 x 10⁻⁵
$D_{O_2-H_2O}^0$	308.1	2.82 x 10⁻⁵
$D_{O_2-N_2}^0$	293.2	2.2 x 10⁻⁵
$D_{H_2O-N_2}^0$	307.5	2.56 x 10⁻⁵

Source: Berning *et al.* (2003)

3. Energy conservation

The energy conservation equation describes the thermal balance within the fuel cell (O'Heyre, 2006)

$$\frac{\delta(\varepsilon\rho h)}{\delta t} + \nabla \cdot (\varepsilon\rho uh) = \nabla \cdot k^{eff}\nabla T + \varepsilon\frac{\delta p}{\delta t} - i\eta + \frac{i\cdot i}{\sigma} + \dot{S}_h \tag{21}$$

The h and k^{eff} stand for the enthalpy of fluid flowing through the fuel cell and its effective thermal conductivity respectively. The first term on the right hand side accounts for the rate of energy change due to thermal conduction. We use an effective thermal conductivity (k^{eff}) to account for heat conduction through porous domains such as the electrode. The second term ($\varepsilon\frac{\delta p}{\delta t}$) on the right hand side

accounts for the rate of energy change due to mechanical work of the fluids. The third term $(i\eta)$ is the heat generation due to charge transfer. The forth term $\left(\frac{i \cdot i}{\sigma}\right)$ represents joule heating due to ohmic losses. The last term $(\dot{S}_h)$ accounts for entropy losses associated with the electrochemical reaction

$$\dot{S}_h = \Delta \hat{s}_{rxn} \frac{i}{nF} \tag{22}$$

Solving energy conservation equation permits to obtain the temperature profile throughout our fuel cell model.

4. Charge conservation

From the continuity of current in a conducting material,

$$\nabla \cdot \boldsymbol{i} = 0 \tag{23}$$

Two type of charges present in fuel cell systems, electrons and ions. Since both types of charge are generated from originally neutral species, overall charge neutrality must be conserved.

$$\nabla \cdot \boldsymbol{i}_{elec} = \nabla \cdot \boldsymbol{i}_{ion} = 0 \tag{24}$$

Rearrangement of equation (24) relates it to local current density $(\dot{\boldsymbol{I}})$.

$$-\nabla \cdot \boldsymbol{i}_{ion} + \nabla \cdot \boldsymbol{i}_{elec} = \dot{\boldsymbol{I}} \tag{25}$$

By incorporating Ohm's law into equation (25), we get

$$-\nabla \cdot (\sigma_{ion} \nabla \varphi_{ion}) = \nabla \cdot (\sigma_{elec} \nabla \varphi_{elec}) = \dot{\boldsymbol{I}} \tag{26}$$

where σ is electric conductivity, φ is electric potential.

This equation can be universally applied to all domains in a fuel cell by simply setting a proper value σ for in each domain.

5. Electrochemical reaction : Butler-Volmer equation

The Butler-Volmer equation describes the charge transfer reaction process in the catalyst layer of a fuel cell.

$$i = i_0 \left[\frac{c_R^*}{c_R^{ref}} exp\left\{ \frac{n\alpha F}{RT} \eta \right\} - \frac{c_P^*}{c_P^{ref}} exp\left\{ \frac{-n(1-\alpha)F}{RT} \eta \right\} \right] \qquad (27)$$

where i is current density, i_0 is exchange current density, c is concentration, subscript P and R represent product and reactant respectively. n is number of electron in rate determining step, α is charge transfer coefficient, F is faraday's constant, R is gas constant, T is temperature, and η is activation overpotential.

Since the reactant and product concentration in each side of reaction is hard to determine, the concentration ratio can be replace with mole fraction ratio instead.

$$i = i_0 \left[exp\left\{ \frac{n\alpha F}{RT} \eta \right\} - exp\left\{ \frac{-n(1-\alpha)F}{RT} \eta \right\} \right] \prod_{i=1}^{N} \left(\frac{x_i}{x_i^0} \right)^{\beta_i} \quad (28)$$

where X is mole fraction of reactant specie, and β is stoichiometric number at rate determining step.

Recall that the activation overpotential, η, represents the potential difference between the ionic and electron conducting phases during an electrochemical reaction. Thus, the difference between these two potential is the overpotential.

$$\eta = \varphi_{ion} - \varphi_{elec} \tag{29}$$

Substitute equation (29) into equation (28).

$$i = i_0 \left[\begin{array}{c} exp\left\{ \frac{n\alpha F}{RT}(\varphi_{ion} - \varphi_{elec}) \right\} \\ -exp\left\{ \frac{-n(1-\alpha)F}{RT}(\varphi_{ion} - \varphi_{elec}) \right\} \end{array} \right] \prod_{i=1}^{N} \left(\frac{X_i}{X_i^0} \right)^{\beta_i} \tag{30}$$

The equation (23) is represented by O'Hayre et al.(2006).

6. Water balance in membrane

In PEMFC, the water concentration in membrane has a significant effect on proton conductivity. The electrolyte membrane should be always wet to improve the proton conductivity. Usually, the hydration level is achieved by humidifying the fuel and oxidant gases provisioned to the fuel cell.

The model of water balance in the membrane is in a similar form of the continuity equation.

$$\nabla \cdot N_{H_2O} = 0 \tag{31}$$

where N_{H2O} is water flux vector.

The positive value of N_{H_2O} means net water flux from anode to cathode, and negative value means cathode to anode.

The mass flux of water in the membrane is govern by three processes: electro osmotic drag, water back diffusion, and convective flow due to pressure gradient. The last term can be neglect since the membrane permeability of gases is very low. The water mass flux due to electro-osmotic drag is simplified by the model

$$N_{H_2O,drag} = 2n_{drag}\frac{i}{2F} \qquad (32)$$

The quantity $\frac{i}{2F}$ is the H_2 flux. The factor 2 in front of the equation then converts from hydrogen flux to proton flux.

At open circuit voltage, the electrochemical is at equilibrium because there is no net current flux output from fuel cell. The water concentration will be equal on each side (anode and cathode). When the fuel cell is operated, there is a net current output. The water will generated at cathode side. The concentration gradient is increased due to the generated water from electrochemical reaction and water mass transfer due to electro-osmotic drag. The water diffusion take place at this situation so-called back diffusion of water. The back diffusion flux can be determined by Fick's law of diffusion.

$$N_{H_2O,back\ diffusion} = -D_\lambda \nabla C_{H_2O} \qquad (33)$$

Since the total water flux in Nafion® is simply the addition of electro-osmotic drag and back diffusion, the model for water balance in Nafion® membrane is defined as

$$N_{H_2O} = 2n_{drag}\frac{j}{2F} - D_\lambda \nabla C_{H_2O} \qquad (34)$$

VI. Development of PEMFC modeling and simulation

A one-dimensional non-isothermal model of PEMFC has been developed by Rowe *et al.* (2001) to investigate of various design and operating condition on the cell performance, thermal response, and water management. It is found that the temperature distribution within PEM fuel cell is affected by the water content in the PEM fuel cell especially at low operating temperature. The reduction of cell performance is mainly affected by lower anode gas humidifier while the reduction of

relative humidity of cathode gas do not effect to the performance of PEM fuel cell at high current density. Thus the hydration level is important for maintain at suitable value for a cell. Guvelioglu and Stenger (2005) presented a two-dimensional computational fluid dynamics model of a polymer electrolyte membrane fuel cell. The mass transport, momentum transport, and electrochemical processes occurring in the membrane electrolyte and catalyst layers have been modeled. It is found that a smaller sized channels and bipolar plate shoulders are required to obtain higher current densities. The increasing porosity of the gas diffusion layer helps the mass transport if the application required a bigger channel and shoulder sizes. The effect of the relative humidity of the anode gas stream was found to be the most critical condition affecting the performance of the fuel cell. These results agree well with Rowe et al. A three-dimensional computational fluid dynamics model of a PEM fuel cell with serpentine flow field channels is presented by Nguyen *et al*. (2003). The comprehensive model accounts for the major transport phenomena in a PEM fuel cell: convective and diffusive heat and mass transfer, electrode kinetics, and potential fields. A unique feature of the model is the implementation of a voltage-to-current (VTC) algorithm that solves for the potential fields and allows for the computation of the local activation overpotential. It is found that the predicted distributions at high load show current density maxima under the gas channel area, low load simulations exhibit local current maxima under the collector plate land areas. Baschuk *et al.* (2009) developed a comprehensive, consistent, and systematic model used with an isothermal, steady state, and two-dimensional PEMFC. The model simulations show that the length of the gas flow channel has a significant effect on the current production of the PEMFC, with a longer channel length having a lower performance relative to a shorter channel length. This lower performance is caused by a greater variation in water content within the longer channel length. In 2006, A new problem solving algorithm is presented by Guvelioglu and Stenger to integrate component balances along polymer electrolyte membrane fuel cell (PEMFC) channels to obtain three-dimensional results from a detailed two-dimensional finite element model. This approach, of integrating a detailed two-dimensional across-the-channel model is a promising method for fuel cell design due to its low computational cost compared to three-dimensional computational fluid dynamics models. The studying about the

reactants flow rate and humidification level was investigated and found that the reactants flow rate and humidification level are critical to current density, membrane dry-out, and electrode flooding. Gwang-Soo Kim *et al.* (2010) had compared results from a hierarchy of reduced-dimensional models to the results from a comprehensive three-dimension CFD model for a single, straight-channel unit cell. The quality of the simulation results from reduced-dimensional models, including the cell voltage and the distributions of current density and relative humidity, are assessed. The 2 + 1D approach is optimal in terms of both efficiency and accuracy.

For the recent work, the two-dimensional (2D) non-isothermal simulation for two channel PEM fuel cell was investigated with FEMLAB 3.0a which can solve by coupling the involved variables and solve together. This software can give a realistic solution for each local point in the geometry. The simulation was done by couple variables in momentum, heat, mass, and charge transfer model for investigated the local parameters and values inside the PEM fuel cell. The study to learn more about the ability of the model in an implementation at various operating condition is investigated. The effect of operating temperature and pressure is studied and compare with known experimental results. The results will can be used for optimization of the fuel cell components, design, and operating conditions for different application.

RESEARCH METHODOLOGY

1. Assumptions

The system is steady state and non-isothermal. Assume that the heat transfer out from the control volume occurs at the boundary in contact with the rib only (the rest of the boundaries are adiabatic walls). All fluids is in gas phase and ideal gas mixture is applied. The resistance at interface and the cross-over losses are negligible. The porosity of GDL is homogeneous. The heat content of the gas is neglected. The gravitational force does not effect to the gas.

2. Geometry

The length and width of a typical active area of 5 cm^2 single cell is between 2 and 3 cm. A typical cell thickness is in the range of 4-5 mm, this includes the number of the flow channel and the rib of the flow field, cathode and anode GDL, catalyst layers and electrolyte membrane. The thickness of the active catalyst layers is about 10 μm, which is very small with respect to other cell components. Therefore, the thickness of the catalyst layer can be treated as reactive boundaries for simplification catalyst layer.

A schematic illustration of a PEM fuel cell in this study divided into three sub geometry consists of anode gas diffusion layer, polymer electrolyte membrane, and cathode gas diffusion layer. The gas diffusion layers have a thickness of 400 μm for each of anode and cathode side (Type 10 BA of SIGRACET GDL). The width of channel and rib are 1 mm. The Nafion membrane has a thickness of 100 μm (Nafion 112). The catalyst layer is treated as a reactive boundary layer. The schematic diagram of geometry is shown in **Figure 14**. The gas diffusion layer is affected by hot pressing and the recess is 0.1 mm. For convenience, the boundary of the geometry is labeled as shown in **Figure 15**.
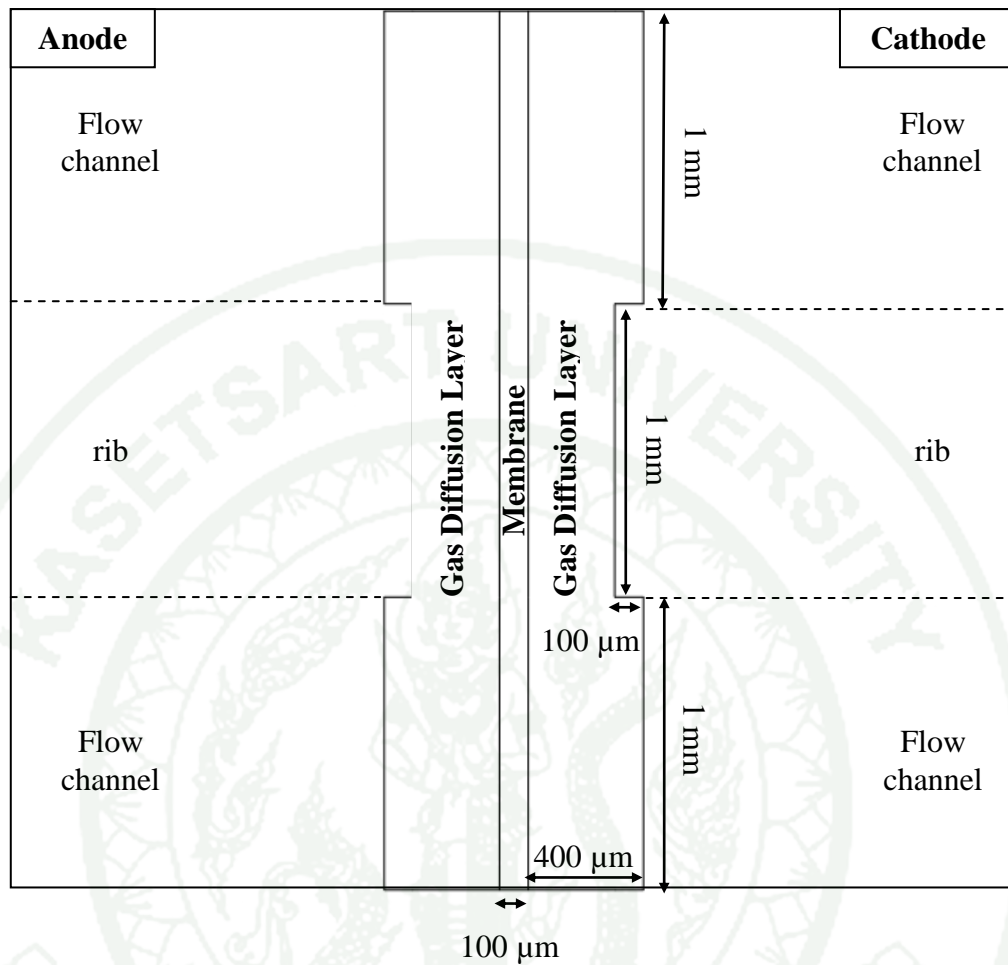
Figure 14 The geometry of proton exchange membrane fuel cell component consist
of gas diffusion layer at anode, Nafion membrane and gas diffusion layer
at cathode, respectively (from left side to right side)
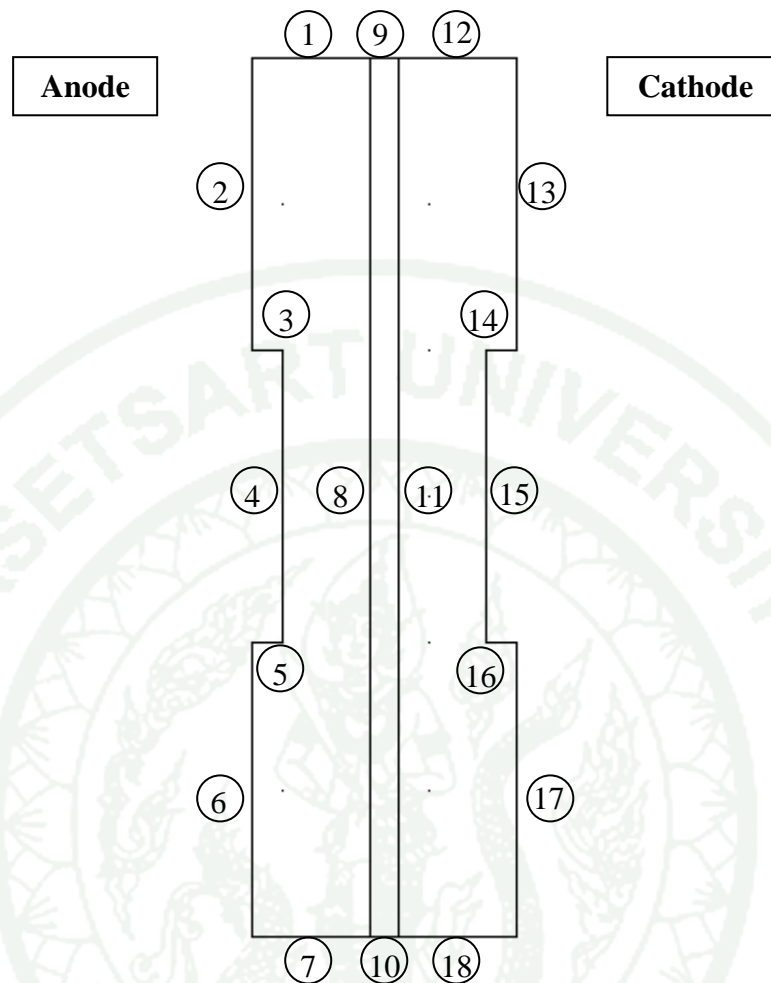
Figure 15 The boundary layers with labels

3. Mesh generation

The mesh is generated with normal predefined mesh size (maximum element size is ~0.16 mm). The maximum element sizes at boundaries 8 and 11 are 0.05 mm. Rib corners have 0.1 μm maximum element size. The shape of the element is triangle.

The summary of mesh parameters after mesh generation process is shown in **Table 6**. The number of degree of freedom is 36,531. There are 4,426 elements with 2,339 mesh points. Number of boundary elements is 370 and The number of vertex elements is 24. The minimum element quality is 0.8 with an element area ratio of 3.34 $\times 10^{-7}$. The mesh visualization is presented in **Figure 16**.

Table 6 The global mesh parameters

Mesh parameters	Values
Number of degree of freedom	36,531
Number of mesh points	2,339
Number of elements (triangular)	4,426
Number of boundary elements	370
Number of vertex elements	24
Minimum element quality	0.800
Element area ratio	3.34×10^{-7}
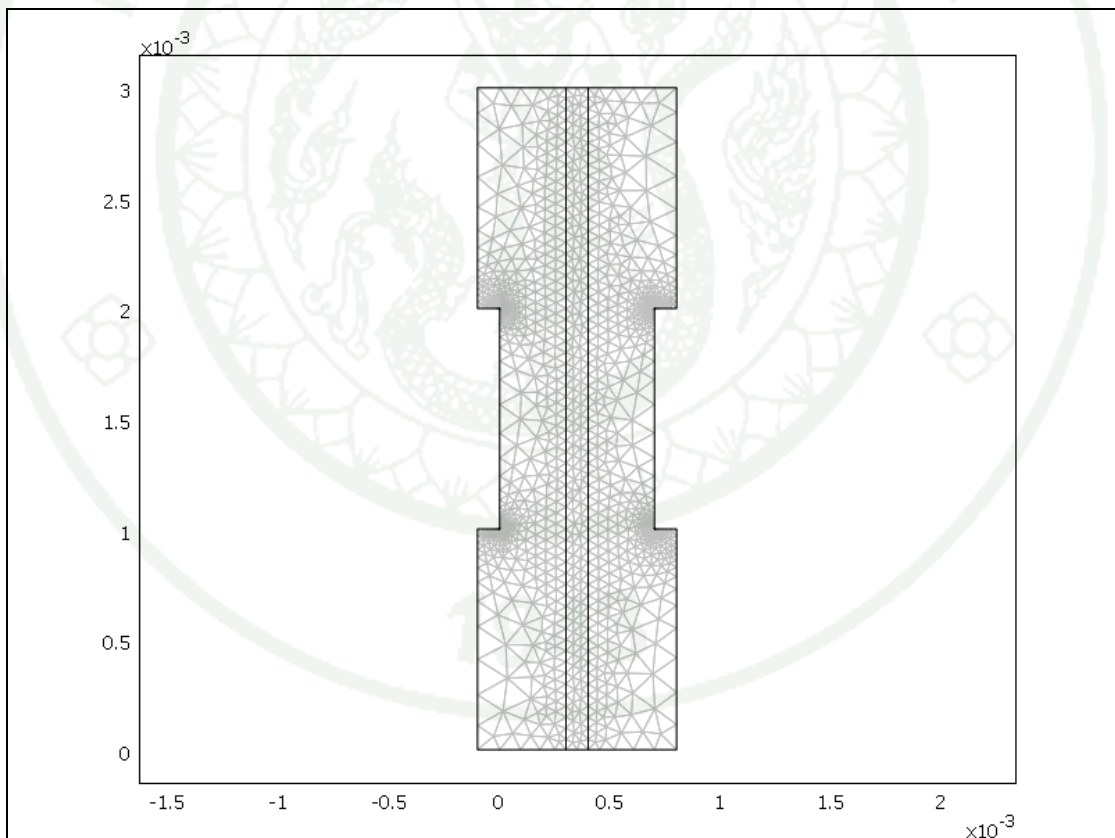
Figure 16 The visualization of mesh element generated by FEMLAB 3.0a.

4. Solution procedure

All of the governing equations were solved by FEMLAB 3.0a. A stationary non-linear solver was used together with Direct (UMFPACK) linear system solver. The relative tolerance for the error criteria was 1×10^{-6}. The operating conditions including the open circuit voltage of the fuel cell are used as initial condition of the dependent variables for the software (global input to the software). Because the dependent variables vary greatly in magnitude, the unconverged solutions were manual adjusted and used as initial condition for the software input to improve numerical convergence.

The summary of solution procedure is shown in **Figure 17**. First, the geometry was defined, after that, the equation was setup in the model navigator. The constants and expressions were defined in the option setup. The mesh was generated before setting up the solver parameters. The PARADISO linear system solver is used for momentum, energy, and charge transport equations, and the UMFPACK linear system solver is used for mass transport equation.

Solving process can be separated into two steps. In the first step the open circuit voltage is input condition, the solution at open circuit voltage is solved starting with the parameters at open circuit voltage. The solution procedure follows the solution process as described before. The parameters are calculated at open circuit voltage and input as an initial condition for solver. The charge transport and momentum balance are solved together and resulted in current density profile and pressure distribution. This part solved for only one fuel cell voltage at a time. The parameters obtained are kept and used as initial guess for calculation of the next lower fuel cell voltage. The software calculates the charge balance first. Then the charge transport and momentum balance are solved together resulted in current density and pressure inside the cell. Next, the temperature profile is solved by using the solution from the previous step as an initial guess. Finally, the mass transport is solved by coupling all of variables from momentum, heat, and charge transport together. The solution process was repeated until the solution errors are in the convergence criteria.

Then, the next lower voltage is input to the software and solved as described previously. All of the variables are adjusted to local points by software and used together in every calculation of local solutions. The solution at higher voltage acted as an initial value of the next solution process. In this way, the solution is solved at near OCV (1.15 v) first, then the fuel cell voltage is reduced by 0.05 volt on each step until reach 0.5 v where the software stops. The second step is the generations of polarization curve from the voltages and current densities data. The problem is solved by a parametric solver with UMFPACK as a non-linear solver.

The 2D simulation for each operating cell potential converged in 30–400 s. The larger values were for the high current density or limiting reactant cases. The calculation were completed under 150 s on an DELL PRECISION, Intel[®] Xenon[®] 3.2 GHz 2 CPUs with 16GB of DDRam.
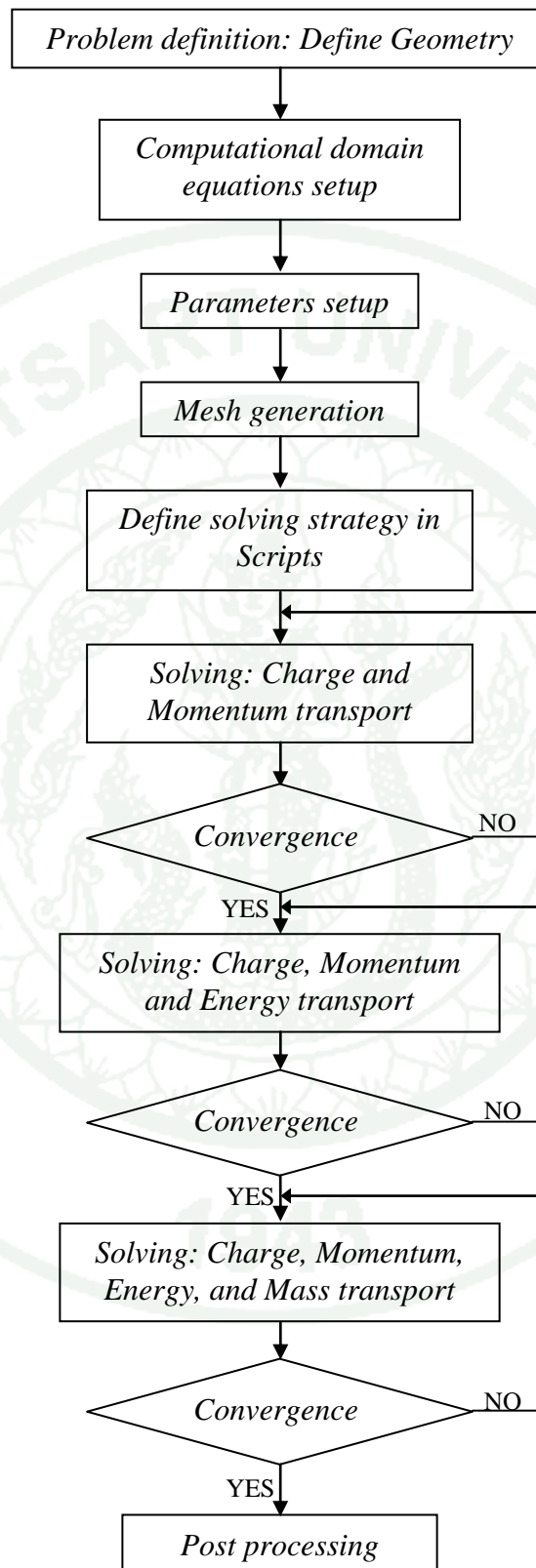
Figure 17 The schematic diagram represent the solution process

5. Modeling: Mathematical

In the fuel cell, the fuel gas flow along the flow channel. The gas goes through the GDL to the catalyst layer and reacts. The gas is transport through the GDL by diffusion and convection. The convection can be described by the momentum equation in terms of the Darcy's law and the diffusion can be represented by Fick's law. The reacted product (H^+) from anode catalyst layer diffused through the membrane to react with oxygen at the cathode catalyst layer. The reaction product at cathode is water which can back diffuse to anode side. In modeling, the catalyst layer is treated as boundary conditions. Therefore the modeling will involve the GDLs and the membrane.

A. Gas diffusion layer

The convection of gas in the GDL can be explained by Darcy's law. The momentum balance equation is a combination of Darcy's law and the continuity equation. Velocity vector is determined by the pressure gradient, the fluid viscosity, and the structure of the porous media represented with the equation (14):

$$u = -\frac{\kappa}{\mu}\nabla p \qquad (14)$$

where u is velocity vector, κ is permeability, μ is viscosity, and p is pressure. The continuity equation is

$$\frac{\partial}{\partial t}(\rho\varepsilon) + \nabla \cdot (\rho u) = F \qquad (35)$$

The velocity vector in equation (35) is substituted by equation (14)

$$\frac{\partial}{\partial t}(\rho\varepsilon) + \nabla \cdot \left(\rho(-\frac{\kappa}{\mu}\nabla p)\right) = F \qquad (36)$$

At steady state, the time dependent term is neglected. The governing equation for GDLs in anode and cathode are represented by

$$\nabla \cdot \left(\rho_a \left(-\frac{\kappa_a}{\mu_a} \nabla p_a \right) \right) = 0 \tag{37}$$

$$\nabla \cdot \left(\rho_c \left(-\frac{\kappa_c}{\mu_c} \nabla p_c \right) \right) = 0 \tag{38}$$

where μ is viscosity of gas, p is pressure, and ρ is density of gas. Subscripts a and c represent anode and cathode respectively.

Since the ideal gas law is applied, the density of the gas mixture was calculated from

$$\rho_a = \frac{p_a M_a}{RT} \tag{39}$$

$$\rho_c = \frac{p_c M_c}{RT} \tag{40}$$

where M is an average molecular weight and subscripts a and c represent the anode and cathode respectively. Average molecular weight (M_a and M_c) of anode and cathode gases are calculated from the relations

$$M_a = x_{H_2} M_{H_2} + x_{H_2O} M_{H_2O} \tag{41}$$

$$M_c = x_{O_2} M_{O_2} + x_{H_2O} M_{H_2O} \tag{42}$$

For multi-component transport, a species balances in the gas diffusion layers are solved with the equation (18). At steady state, the governing equation is

$$\nabla \cdot \left(-\rho_a w_i \sum \left(D_{ij}^{eff} \nabla x_j + (x_j - w_j) \frac{\nabla p_a}{p_a} \right) + \rho_a w_i u_a \right) = 0 \tag{43}$$

$$\nabla \cdot \left(-\rho_c w_i \sum \left(D_{ij}^{eff} \nabla x_j + (x_j - w_j)\frac{\nabla p_c}{p_c} \right) + \rho_c w_i u_c \right) = 0 \tag{44}$$

where i is either H_2 or H_2O for anode, and O_2 or H_2O for cathode. The effective binary diffusivity is calculated from equation (20) for the fluids flow in porous media.

$$D_{ij}^{eff} = D_{ij}\varepsilon^{1.5} \tag{20}$$

The binary diffusivity is calculated from equation (19) and the porosity is obtained from **Table 2**.

Since the average heat flux across the solid phase is dominated, the convective heat transfer in GDL is negligible (Hwang, J.J., et at., 2006). The temperature profiles are solved by assuming that there is only heat transfer by conduction in GDL subdomain. Since the ohmic losses due to electron transport also include in this region, the heat generation from joule heating must be included in the model. From equation (21), the governing equation at steady state is

$$-\nabla \cdot k^{eff} \nabla T_s = \frac{\vec{i} \cdot \vec{i}}{\sigma_s} \tag{45}$$

where the effective thermal conductivity, k^{eff}, and electronic conductivity, σ_s, of gas diffusion layer are obtained from **Table 4** and **Table 2**, respectively.

In addition to mass, momentum, and energy balances in the porous GDL the charge balance is also solved in the electrodes with the continuity relationship (Kovetz, A., 1990):

$$\nabla \cdot (\sigma_s \nabla \phi_s) = 0 \tag{46}$$

The Darcy's law, mass transfer, heat transfer, and charge balance equations are coupled through the velocity vector, u, pressure, p, fluid gas density, ρ, average molecular weight, M, temperature, T_s, and current density flux, i.

B. Nafion® membrane

The gas permeability of the membrane is very low and can be neglected. Thus, only water and proton can be transported through this region.

The proton transport is simulated using the equation (Kovetz, A., 1990):

$$\nabla \cdot (\sigma_m \nabla \phi_m) = 0 \tag{47}$$

where the proton conductivity of Nafion® is estimated from equation (9)

$$\sigma(T, \lambda) = \sigma_{303K}(\lambda)\exp\left[1268\left(\frac{1}{303} - \frac{1}{T}\right)\right] \tag{9}$$

The water balance in the membrane is the result from the total water flux passing through the membrane. At steady state, water flux through the membrane is shown in equation (31).

$$\nabla \cdot N_{H_2O} = 0 \tag{31}$$

The total water flux in Nafion is the addition of electro-osmotic drag and back diffusion of water. From equation (34),

$$N_{H_2O} = 2n_{drag}\frac{j}{2F} - D_\lambda \nabla C_{H_2O} \tag{34}$$

At steady state, the equation (34) is substituted into equation (31). The governing equation is

$$\nabla \cdot \left(2n_{drag}\frac{j}{2F} - D_\lambda \nabla C_{H_2O}\right) = 0 \tag{35}$$

where the electro-osmotic drag coefficient is calculated from equation (7), and water diffusivity is calculated from equation (8). The value of C_{H2O} depends on the membrane temperature (O'Hayre, 2006)

The temperature distribution in the membrane is solved with energy balance equation. At steady state, there are heat transfers by conduction from anode to cathode sides and joule's heating term in the membrane, thus the governing equation is

$$-\nabla \cdot k^{eff} \nabla T_m = \frac{\vec{i} \cdot \vec{i}}{\sigma_m} \tag{48}$$

The water balance, energy transport, and charge balance equations are coupled through the water concentration, $C_{H_2 O}$, temperature, T_m, and current density flux, i.

6. Boundary condition

A. Gas diffusion layer

The reactant gases were fed at inlet channel, diffuse through the gas diffusion layer, react at catalyst layer, and then leave to the flow channel. The inlet boundaries are the boundary 2 for anode and 13 for cathode as shown in **Figure**.

At boundary 2, the boundary condition is

$$p = p_{inlet,a} \tag{49}$$

And the boundary condition at cathode boundary (boundary 13)

$$p = p_{inlet,c} \tag{50}$$

And at the outlet boundary layer, boundaries 6 and 17, the pressure is atmospheric pressure on both sides.

$$p_c = p_a = p_{atm} \tag{51}$$

At a catalyst surface, the reactive boundary layer, the velocity was solve from

At anode side:
$$\boldsymbol{n} \cdot \boldsymbol{u} = \frac{\left(\frac{i_a \cdot M_{H_2}}{2F} + \frac{i_a \cdot n_{drag} \cdot M_{H_2O}}{F}\right)}{\rho_{local}} \tag{52}$$

At cathode side:
$$\boldsymbol{n} \cdot \boldsymbol{u} = \frac{\frac{i_c \cdot M_{O_2}}{4F} - \left(\frac{i_c \cdot M_{H_2O}}{2F} + \frac{i_c \cdot n_{drag} \cdot M_{H_2O}}{F}\right)}{\rho_{local}} \tag{53}$$

The first term in equation of anode side represents to flux of hydrogen consumption, and the second term is a flux of water due to electro-osmotic drag. For the cathode side, the first term represent the oxygen consumption flux. The second and third terms represent flux of water produce from reaction and flux of water due to electro-osmotic drag, respectively. The flux is divided by local density to results of velocity profile in a normal direction to boundary. The others boundaries was treated as an insulate. There are no flux through those boundary.

$$\boldsymbol{n} \cdot \boldsymbol{u} = 0 \tag{54}$$

The reactant gases were fed with humidity at 100%RH. At saturation level, the mole fraction of water in the vapor was determined by Raoult's law. Thus, the mole fraction of hydrogen at inlet is

$$x_{H_2} = 1 - \frac{p_{SAT}}{p_{inlet}} \tag{55}$$

The reactant at cathode is oxygen gas. Similarly, the mole fraction of oxygen at inlet is

$$x_{O_2} = 1 - \frac{P_{SAT}}{P_{inlet}} \qquad (56)$$

The conversion of mole fraction to mass fraction is determined by the relation

$$w_{H_2} = \frac{x_{H_2} \cdot M_{H_2}}{x_{H_2} \cdot M_{H_2} + x_{H_2O} \cdot M_{H_2O}} \qquad (57)$$

$$w_{O_2} = \frac{x_{O_2} \cdot M_{O_2}}{x_{O_2} \cdot M_{O_2} + x_{H_2O} \cdot M_{H_2O}} \qquad (58)$$

The boundary layer at outlet (boundaries 6 and 17) were assumed that mass passing through this boundary is convective-dominated. The diffusion term in equation (43) and (44) become zero.

$$\boldsymbol{n} \cdot \left[-\rho w_i \sum_{j=1}^{n} \overline{D}_{ij} \left(\nabla x_j + (x_j - w_i) \frac{\nabla p}{p} \right) \right] = 0 \qquad (59)$$

The flux of reactant consumption at catalyst boundary was determined from the current density flux that fuel cell produce. The hydrogen is reacted at boundary 8. The flux of hydrogen flow through the boundary is.

$$\boldsymbol{n} \cdot \boldsymbol{N}_{H_2} = \frac{i_a \cdot M_{H_2}}{2F} \qquad (60)$$

where $\boldsymbol{n}$ represent the normal vector to the boundary 8. And also, at cathode reactive boundary layer, where the reduction reaction take place, the flux of oxygen flow into the catalyst layer is

$$\boldsymbol{n} \cdot \boldsymbol{N}_{O_2} = \frac{i_c \cdot M_{O_2}}{4F} \qquad (61)$$

where $\boldsymbol{n}$ represent the normal vector to the boundary 11. The others boundary conditions are insulation, no mass flux pass through those boundaries.

$$\boldsymbol{n} \cdot \boldsymbol{N_{H_2}} = \boldsymbol{n} \cdot \boldsymbol{N_{O_2}} = 0 \tag{62}$$

The current density at catalyst surface was solved by equation (30).

$$i = i_0 \left[\begin{array}{c} exp\left\{ \frac{n\alpha F}{RT}(\varphi_{ion} - \varphi_{elec}) \right\} \\ -exp\left\{ \frac{-n(1-\alpha)F}{RT}(\varphi_{ion} - \varphi_{elec}) \right\} \end{array} \right] \Pi_{i=1}^{N} \left(\frac{x_i}{x_i^0} \right)^{\beta_i} \tag{30}$$

The current density at anode is a result from oxidation reaction of hydrogen at catalyst surface. The activation overpotential at anode catalyst layer is defined as

$$\eta_a = \varphi_s - \varphi_m - E_{eq,a} \tag{63}$$

Thus, the current density distribution for anode oxidation reaction was solved from

$$\boldsymbol{n} \cdot \boldsymbol{I} = i_a = i_{0,a} \left[\begin{array}{c} exp\left\{ \frac{n_a \alpha_a F}{RT}\eta_a \right\} \\ -exp\left\{ \frac{-n_a(1-\alpha_a)F}{RT}\eta_a \right\} \end{array} \right] \frac{x_{H_2}}{x_{H_2}^0} \tag{64}$$

In similar way, the activation overpotential at cathode catalyst layer and current density distribution were defined as

$$\eta_c = \varphi_s - \varphi_m - E_{eq,c}$$
$$\tag{65}$$

$$\boldsymbol{n} \cdot \boldsymbol{I} = -i_c = -i_{0,c} \left[\begin{array}{c} exp\left\{ \frac{n_c \alpha_c F}{RT}\eta_c \right\} \\ -exp\left\{ \frac{-n_c(1-\alpha_c)F}{RT}\eta_c \right\} \end{array} \right] \frac{x_{O_2}}{x_{O_2}^0} \tag{66}$$

where $E_{eq,a}$, $E_{eq,c}$ is the thermodynamics reversible voltage for anode and cathode, respectively. The hydrogen oxidation reaction is a standard electrode potential, thus $E_{eq,a} = 0\ V$. For cathode, $E_{eq,c}$ was calculated using Nernst's equation.

$$E_{eq,c} = 1.229 - 8.46 \times 10^{-4}(T - 298.15) + \frac{RT}{2F} ln \left[\frac{1}{p_{H_2} p_{O_2}^{1/2}} \right] \qquad (67)$$

where n_c and n_a are the electron transfer numbers in the rate determining steps for cathodic oxygen reduction and anodic hydrogen oxidation reactions, respectively. The value of n_a is 1.0, which has been reported in many literature. The value of n_c should be considered in two case. The first case is oxygen reduction in the low current density range, where the Tafel sloped is ~60 mV/decade at 25°C. The electrode surface is partially covered by PtO (Parthasarathy *et al.*, 1992), corresponding to a n_c value of 2.0 for $\alpha \approx 0.5$. For the second case, the Tafel slope is around 120 mV/decade with a n_c value of 1.0, corresponding to a cathode potential range where the electrode surface is pure Pt. In this work, the pure Pt electrode surface was assumed.

The electron transfer coefficient, α_c and α_a, is temperature dependent parameter. α_c can be expressed by Zhang et al.

$$\alpha_c = \alpha_c^0 T \qquad (68)$$

where $\alpha_c^0 = 0.00168$ K^{-1} in temperature range of 25-250°C. The value of α_a was assumed to be 0.5 and independent with temperature.

The exchange current density for the anodic hydrogen oxidation reaction, $i_{0,a}$, was assumed to be a constant value of 1 A m^{-2}. However, the exchange current density for the cathodic oxygen reduction reaction, $i_{0,c}$, is given by Leelasupakorn (2008).

$$i_0 = (7.657 \times 10^6) exp\left(-\frac{7366}{T}\right) exp\left(1.315 L_{Pt}\right) \qquad (69)$$

where L_{Pt} is an amount of catalyst loading (mg cm^{-2}), and T is temperature in Kelvin.

The current is drawn from the fuel cell at rib-GDL contacted region. Thus, the output potential was determined at boundary 4 and 15.

$$\text{Boundary layer 4:} \qquad E = 0 \qquad (70)$$

$$\text{Boundary layer 15:} \qquad E = V_{cell} \qquad (71)$$

The reactive catalyst boundary layers are boundary 8 for anode and boundary 11 for cathode. Thus, the boundary conditions for cathode and anode reactions are

$$\boldsymbol{n} \cdot \boldsymbol{I} = i_a \qquad (72)$$
$$\boldsymbol{n} \cdot \boldsymbol{I} = i_c \qquad (73)$$

The others boundary condition is electric insulation.

$$\boldsymbol{n} \cdot \boldsymbol{I} = 0 \qquad (74)$$

The fuel cell temperature is constant at boundary 1, 4, 7, 9, 10, 12, 18, and 15. The boundary conditions are

$$T = T_{cell} \qquad (75)$$

The heat generations at reactive catalyst boundary caused from the activation overpotential. The heat is generated in the catalyst layer between the GDL and membrane, thereby the boundary condition is

$$\text{Boundary layer 8:} \qquad -\boldsymbol{n}_{GDL} \cdot \boldsymbol{q}_{GDL} - \boldsymbol{n}_m \cdot \boldsymbol{q}_m = i_a \eta_a \qquad (76)$$

$$\text{Boundary layer 11:} \qquad -\boldsymbol{n}_{GDL} \cdot \boldsymbol{q}_{GDL} - \boldsymbol{n}_m \cdot \boldsymbol{q}_m = i_c \eta_c \qquad (77)$$

Since the terms on right hand side in equation (76) and (77) are heat source, thus the negative sign refer to the heat flux flows into the GDL and membrane. The local current density and activation over-potential are calculated from charge balance equations. The others boundary condition is insulated and defined as

$$\mathbf{n} \cdot (-k\nabla T\ ) = 0 \tag{78}$$

Note that the energy balance in GDL and membrane are calculated in the same domain equation.

B. Nafion$^{\circledR}$ membrane

The water concentration, C_{H_2O}, at boundary 8 and 11 were calculated from the relation

$$C_{H_2O} = \lambda \frac{\rho_{dry}}{M_m} \tag{79}$$

where C_{H_2O} is water concentration (mol/m^3), λ is water content in Nafion$^{\circledR}$ membrane (H_2O/SO_3^-), ρ_{dry} is dry density of Nafion® membrane (1980 kg m^{-3}), M_m and is equivalent weight of Nafion® membrane. λ was calculated from equation (6), where the water activity, a_w, defined as equation (5).

$$a_w = \frac{x_w P}{P_{sat}} \tag{5}$$

$$\lambda = \begin{cases} 0.043 + 17.81a_w - 39.85a_w{}^2 + 36.0a_w{}^3 & for\ 0 \leq a_w \leq 1 \\ 14 + 1.4(a_w - 1) & for\ 1 < a_w \leq 3 \end{cases} \tag{6}$$

The boundary conditions at boundaries 9 and 10 were insulated, no mass flux passed through these boundaries.

$$\mathbf{n} \cdot N_{H_2O} = 0 \tag{80}$$

The current density is produced from hydrogen oxidation reaction at boundary 8. The current density was calculated from equation (64)

$$n \cdot I = -i_a \tag{81}$$

and at the boundary 11, the current density is calculated from equation (66)

$$n \cdot I = i_c \tag{82}$$

The negative sign in equation (81) refer to the current density flow into the boundary 8 in normal direction, while the positive sign in equation (82) represent the current density flow out of boundary 11. The boundaries 9 and 10 were insulated. Thus,

$$n \cdot I = 0 \tag{83}$$

7. Operating condition

In simulation, the fuel cell operating parameters were obtained from the experimental works in KU-CHE laboratory. The Pt-catalyst loading is 0.2 mg/cm^2. The fuel cell is operated by use hydrogen at anode and oxygen at cathode. The humidification temperature is equal to cell temperature to maintain the humidity saturation level. The outlet pressure is atmosphere. In an experiment, hydrogen flow rate is 0.2 l/min while oxygen flow rate is 0.1 l/min. In the simulation, since either the pressure or velocity at inlet boundary do not investigated, the inlet pressure was assumed to be 1.1 times of outlet pressure (atmosphere). The effects of operating temperature and back pressure are investigated. Fuel cell operating temperatures vary from 80 - 60°C. with 100% relative humidity. Then the back pressures vary from 1 to 3 atm at 80°C.

8. Post processing

In the simulation, a voltage needed from fuel cells was an input value. The current density, gas velocity, fluid composition and temperature distribution inside the cell were output values obtained from solution process. The operating conditions were specified.

In the simulation, the polarization curve was a plot between fuel cell output voltage and current density. The current density at each voltage was calculated by averaging the local current densities over the whole catalyst active area, as shown in equation (87).

$$I_{avg} = \frac{\int_0^{l_{cat}} I(y)dy}{l_{cat}} \tag{87}$$

where l_{cat} is catalyst boundary length (m), the summation of flow channel length and rib channel length. From **Figure 14**, the flow channel length is 1.0 mm and the rib channel length is 1.0 mm. The geometry consist of 2 flow channel plus 1 channel rib, thus l_{cat} is 2(1.0 mm) + 1 mm = 3 mm.

The reversible voltage of fuel cell was calculated from equation (67) for each local temperature point at cathode reaction surface. The average reversible voltage was calculated in similar form of equation (87), equation (88)

$$\bar{E}_{eq,c} = \frac{\int_0^{l_{cat}} E_{eq,c}(y)dy}{l_{cat}} \tag{88}$$

The activation overpotential was calculated for each of half reaction, anode and cathode. The activation overpotential at anode was simulated and average from each point at anode reaction surface. Thus,

$$\bar{\eta}_{act,a} = \frac{\int_0^{l_{cat}} \eta_{act,a}(y)dy}{l_{cat}} \tag{89}$$

The activation overpotential at cathode was also simulated and average from each point at cathode reaction surface.

$$\bar{\eta}_{act,c} = \frac{\int_0^{l_{cat}} \eta_{act,c}(y)dy}{l_{cat}} \qquad (90)$$

The activation overpotential losses is a combination from anode and cathode side.

$$\bar{\eta}_{act} = \bar{\eta}_{act,c} + \bar{\eta}_{act,a} \qquad (91)$$

Since this simulation did not include a model of concentration losses and cross-over losses, therefore the equation (13) is reduced. Thus the fuel cell voltage is followed as

$$V_{cell} = \bar{E}_{eq} - \bar{\eta}_{act} - \bar{\eta}_{ohmic} - \eta_{cross} \qquad (92)$$

Since the values of V_{cell}, $\bar{E}_{eq}$, $\bar{\eta}_{act}$, and η_{cross} were known. The ohmic losses (η_{ohm}) can be calculated from equation (92).

$$\bar{\eta}_{ohmic} = \bar{E}_{eq} - \bar{\eta}_{act} - \eta_{cross} - V_{cell} \qquad (93)$$

RESULTS AND DISCUSSIONS

The simulation consists of three sections. Begin with the discussion of momentum, heat, and mass transfer in PEMFC at various operating voltage. Second is the discussion about the performance of PEMFC at various operating temperatures. Then follow by the discussion of the performance of PEMFC at various operating pressures.

1. Momentum, Heat, and Mass transport in PEMFC

The hydrodynamics of gas transport in PEMFC were obtained to understand of its behavior. The results are shown in terms of velocity profiles, temperature distribution, hydrogen distribution at anode, oxygen distribution at cathode, water content in membrane, current density distribution in GDL, and current density distribution in membrane.

A. Velocity profile in gas diffusion layers.

The velocity profile and pressure distribution in gas diffusion layer with the coordinate system are shown in **Figure 18**. The gas velocity at anode is higher than the gas velocity at cathode under the same pressure condition because the average gas viscosity at anode ($\bar{\mu}_a = 1.17 \times 10^{-5}$ Pa·s at no load concentration of 1.15 v) is lower than the average gas viscosity at cathode ($\bar{\mu}_c = 1.95 \times 10^{-5}$ Pa·s at no load concentration of 1.15 v). The discussion is separated into two sections. The hydrodynamic behavior is discussed at anode GDL and cathode GDL, respectively.

1. Velocity profile at anode GDL

The no load gas velocity is shown in **Figure 18**(a). At the anode, the gas mixture from the channel flows into GDL with the average velocity equal to -2.90 m/s normal to inlet boundary (x = 1.00, y = 0.00 - 1.00 mm), the negative sign represent the flowing of gas into the GDL towards the catalyst layer. The average velocity

increase to 10.64 m/s at the region between flow channel rib and reaction surface (x = 0.00 - 0.75, y = 1.00 - 2.00 mm). When the anode gas flow to the exit boundary (x = 1.00, y = 2.00 - 3.00 mm), the average gas velocity decrease to 3.34 m/s normal to the boundary, the positive value represents the gas flowing out from the GDL to the flow channel. The average velocity at the region between flow channel rib and reaction surface is about three times of the inlet velocity, thus the high mass transfer capabilities is observed here and the low velocity of reactant gas and water is observed at the entrance and exit region comparing to the behind the rib region.

At the entrance region (x = 1.00, y = 0.00 - 1.00 mm), it is observed that the axial velocity (y-direction) increases while the gas flows towards the GDL and is maximum at the reaction surface, as shown in **Figure 19**. The horizontal velocity is maximum at the entrance boundary and decrease when the anode gas flows to the reaction surface. The lower axial and horizontal velocity is observed near the GDL edge (x = 0.00, y = 0.00 - 0.50 mm), therefore the mass transfer capability is reduced in this zone.

The flow of gas in the region located between channel rib and reaction surface (x = 0.75, y = 1.00 - 2.00 mm) is almost go downward, see **Figure 20**, because the average axial velocity is much more than the average horizontal velocity. From **Figure 18**, the high gas velocity is observed near the corners of rib channel. It is affected from high pressure gradient at the corner of the rib channel. The average axial velocity is increased about 2 times comparing with the axial velocity at the entrance region (from 5 m/s at y = 0.90 mm to 10.79 m/s at y = 1.10 mm, see **Figure 19 and 20**). The higher axial velocity is located near the rib corner and gradually decreases when the gas reach the reaction surface as observed in **Figure 20** at y = 1.10 mm and 1.90 mm. The axial velocity behind the rib GDL is nearly uniform by the axial velocity at rib channel is slightly higher than at the reaction surface.

In contrast, the average horizontal velocity is decreased from -4.5 m/s (at y = 0.90 mm in **Figure 19**) to -0.78 m/s (at y = 1.10 mm in **Figure 20**). This result effects to lower convective mass transfer to the reaction surface in this region. In the

lower part of this region (x = 0 - 0.75, y = 1.50 - 2.00 mm), the direction of horizontal velocity becomes inverse, this means that the gas flows out from the reaction surface, see **Figure 20** at y = 1.50 mm. The magnitude of horizontal velocity increase when the anode gas flows to the channel rib. The increasing of velocity in the flow direction is observed because the decreasing of local pressure cause the expansion of gas. When anode gas flow into exit region (x = 0.00 - 1.00, y = 2.00 - 3.00 mm), the horizontal velocity increase because of the high pressure gradient at the rib corner. Both of axial and horizontal velocities decrease when the gas flow to the lower edge of the GDL.

(a)   (b)
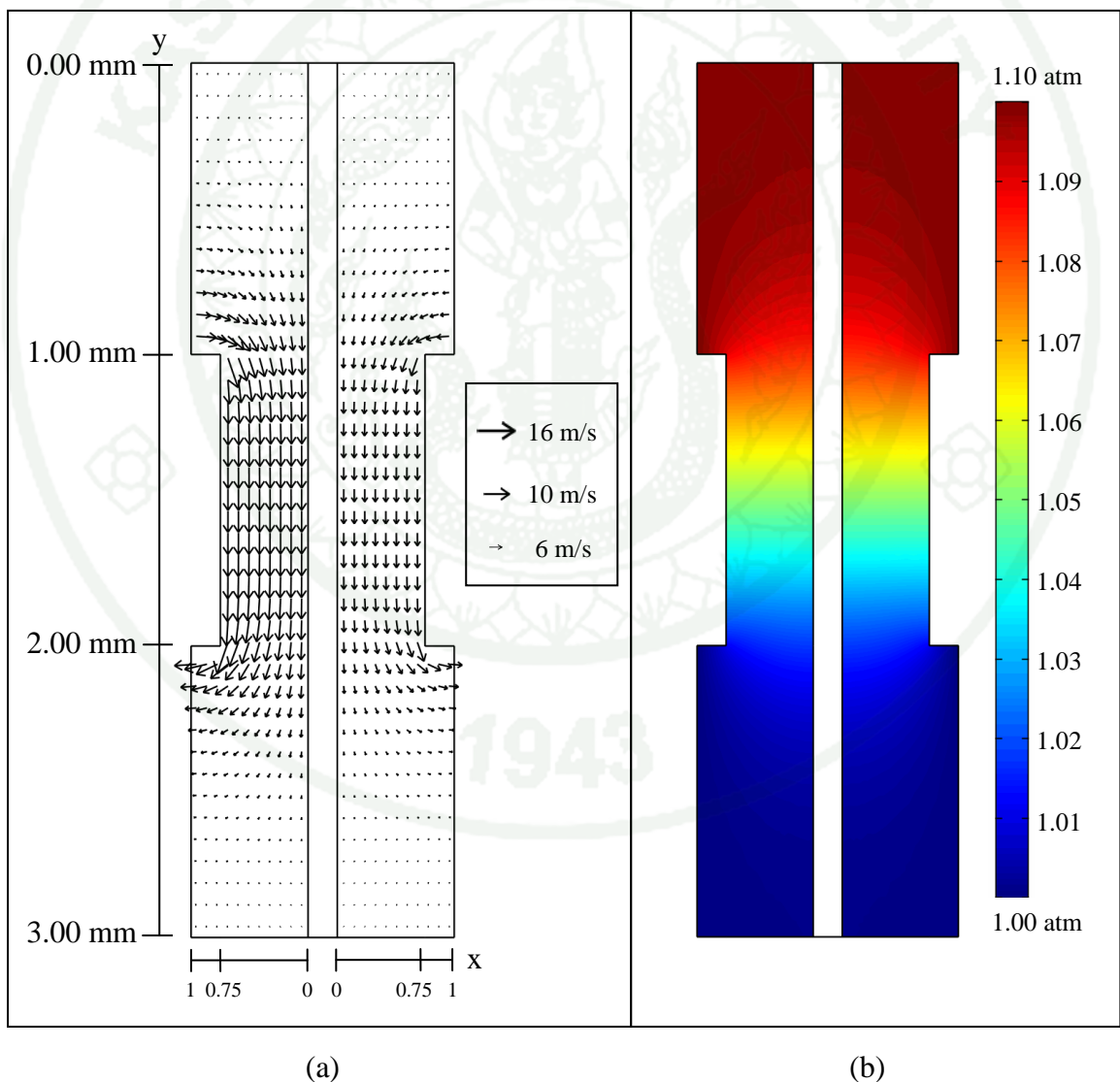
Figure 18 (a) The velocity profiles and (b) pressure distributions at anode and
        cathode gas diffusion layer, at no load condition.
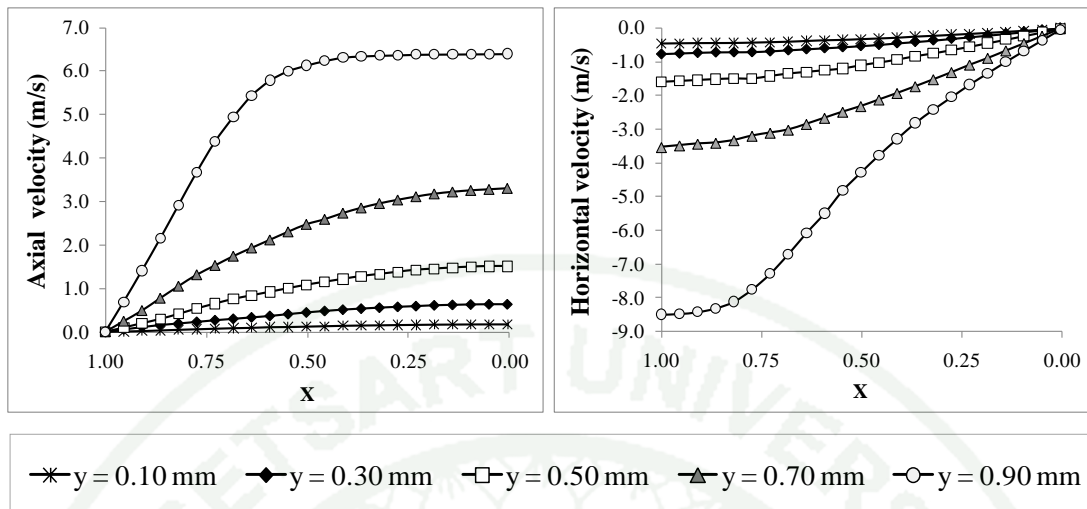
Figure 19 The axial and horizontal velocity profiles at difference position in entrance
region of anode GDL at no load condition. Note that the horizontal
velocity is in negative direction, i.e. flowing towards the catalyst layer.

With no load condition, no gas is consumed in the catalyst layer. Therefore,
all the gas flows into the GDL will flow out from the exit region. When some
electrical loads are applied, the horizontal velocity profiles at anode reaction surface
at various operating voltages are shown in **Figure 22**. The negative sign represents the
flow direction into the reaction surface. It is observed that the velocity at entrance
region is higher than the velocity at exit region. At high operating voltage, 1.15 - 0.9
V, the maximum velocity locates near the corner of channel rib. At low operating
voltages, the maximum velocity is observed at the region between channel rib and
reaction surface (x = 0.00 - 0.75, y = 1.00 - 2.00).

The high convective mass transfer capability can be observed at the region
between channel rib and reaction surface while the low convective mass transfer
capabilities can be observed near the GDL edge. The gas flowing into the catalyst
surface is observed at the upper part of GDL (y = 0.00 - 1.50 mm) while the gas at the
lower part (y = 1.50 - 3.00 mm) is forced by convection to flow out from the reaction
surface. However, the gas in anode GDL can reach the reaction surface by diffusion.
At the anode reaction surface, the direction of gas flows into the reaction surface and

the flow rate is maximized at the region between channel rib and reaction surface. The discussion of diffusion flux is presented in mass transfer section.
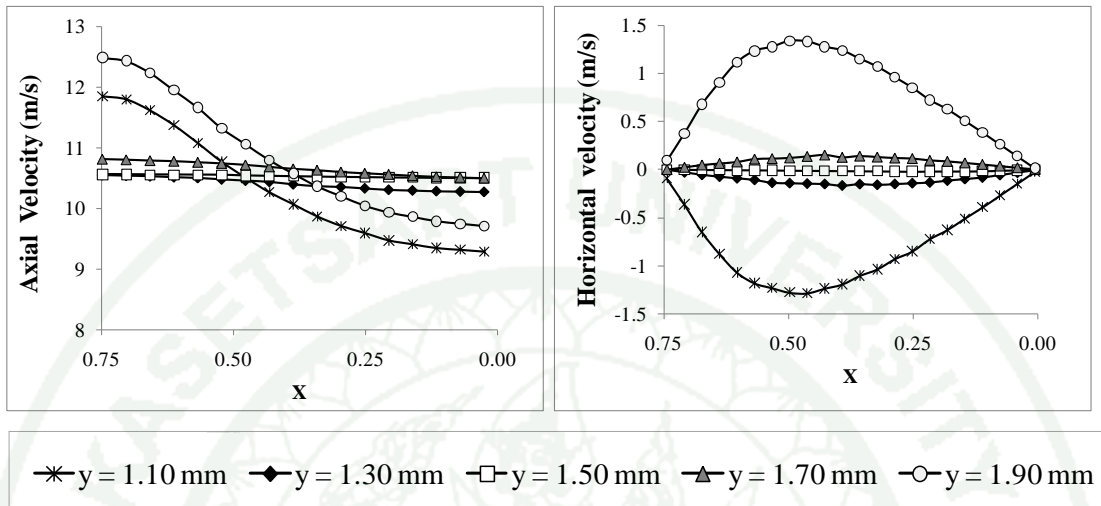
Figure 20 The axial and horizontal velocity profiles at different positions in a region between channel rib and reaction surface of anode GDL at no load condition.
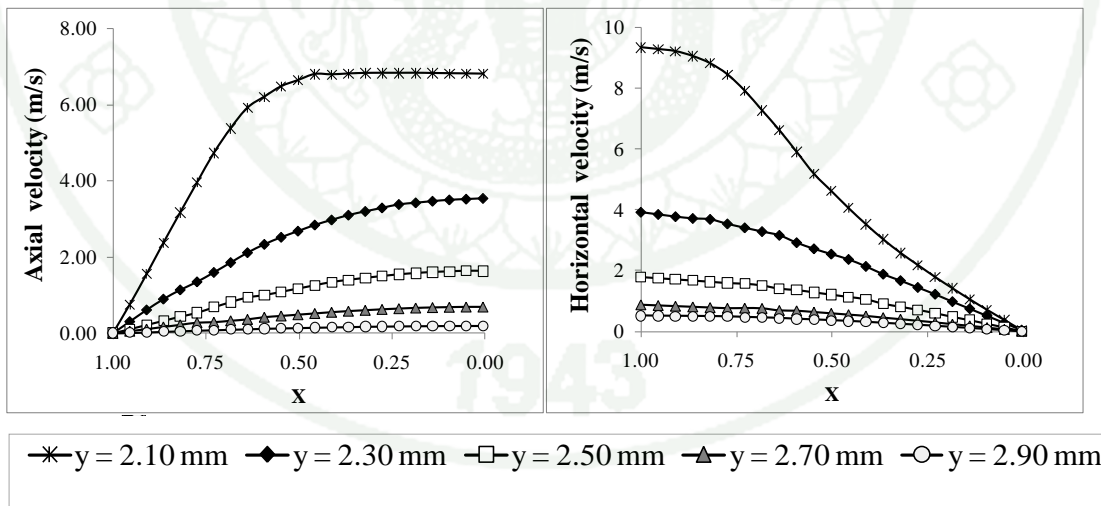
Figure 21 The axial and horizontal velocity profiles at different positions in exit region of anode GDL at no load condition.
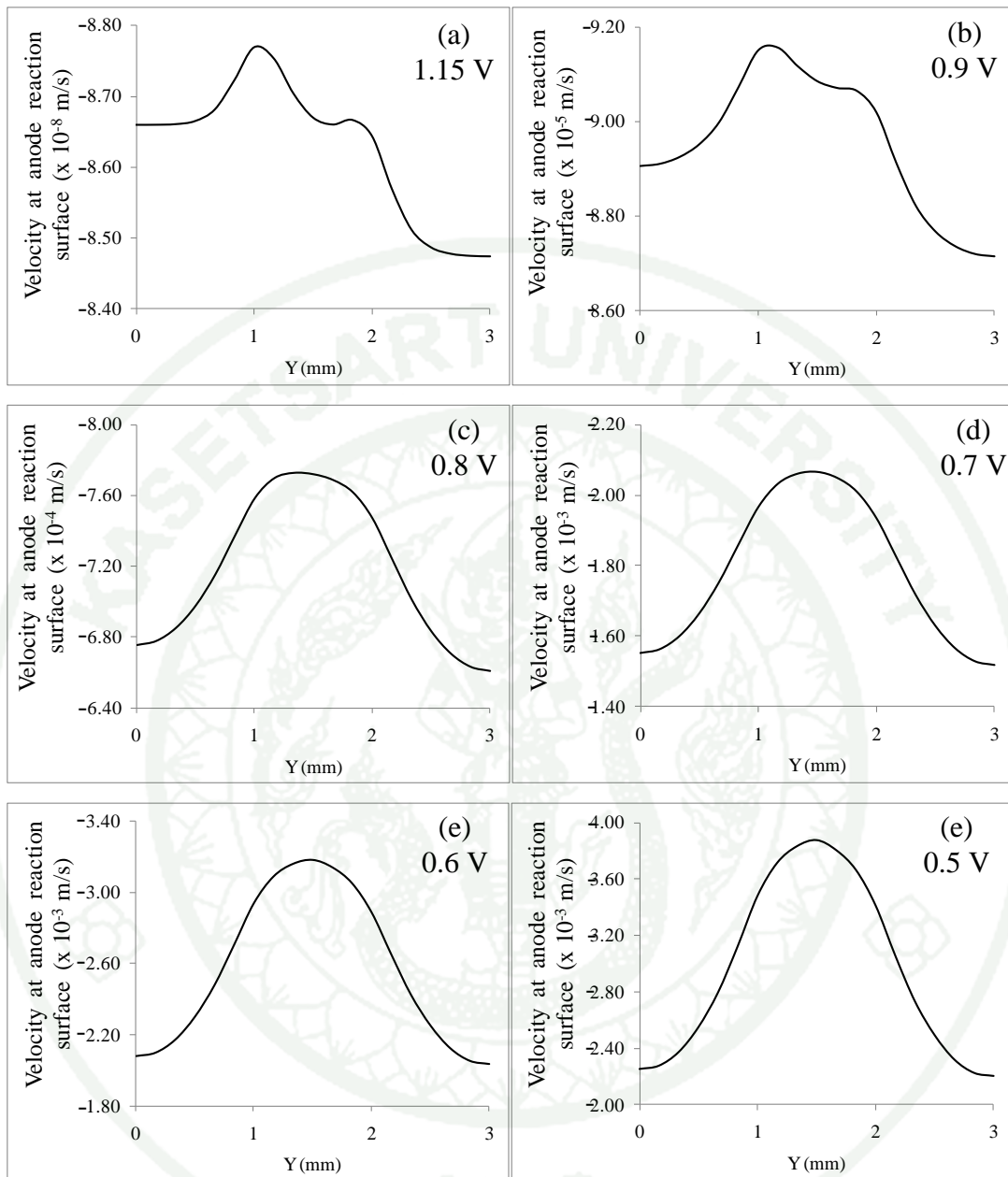
Figure 22 The horizontal velocity profiles of gas flowing into anode reaction surface;
(a) 1.15 V, (b) 0.9 V, (c) 0.8 V, (d) 0.7 V, (e) 0.6 V, and (f) 0.5 V.

2. Velocity profile at cathode GDL.

The results at no load condition are observed as follow. The average velocity at the entrance of GDL (x = 0.00 - 1.00, y = 0.00 - 1.00 mm) is -1.82 m/s in the normal direction to the boundary. The negative sign represents the flow direction

towards the reaction surface. The average velocity in the region between channel rib and reaction surface (x = 0.00 - 0.75, y = 1.00 - 2.00 mm) is 6.34 m/s and the average velocity at the exit region (x = 0.00 - 1.00, y = 2.00 - 3.00 mm) is 2.0 m/s. The high velocity is also observed at the region between channel rib and reaction surface. Thus the high mass transfer capability is observed here. The low velocity near the upper and lower edges of GDL shows the reducing of the ability to replenish the reactant gas and the removal of water.

At the entrance region (x = 0.00 - 1.00, y = 0.00 - 1.00 mm), it is observed that the axial velocity (downward direction) is low at near the GDL edge (y = 0.10 mm) and can increase to more than 4 m/s (at y = 0.90 mm), as shown in **Figure 23**. The horizontal velocity is maximum at the entrance boundary (x = 0.00 - 1.00, y = 0.90 mm) and decreases when it flows inside the GDL. The gas near the channel rib flows faster than the gas near the edge of GDL (x = 0.00 - 1.00, y = 0.1 mm). Therefore the replenishing of reactant is better in this zone while the capability to refresh the reactant at the edge of GDL is low. They are the same as in the anode side.

At the region between channel rib and reaction surface (x = 0.00 - 0.75, y = 1.00 - 2.00 mm), the axial gas velocity increases for 2 times of the axial velocity in the entrance region (from 3.0 m/s at y = 0.90 mm to 6.1 m/s at y = 1.10 mm. The high gas velocity observed near the corners of rib channel is affected from high pressure gradient at the corner of rib channel. The higher axial velocity is located near the rib corner (x = 0.75, y = 0.90) and gradually decrease when the gas flows through GDL near the reaction surface (x - 0.00) as observed at y = 1.10 mm and 1.90 mm. The axial velocity in the GDL behind the rib is nearly uniform. However, the axial velocity near the rib (x = 0.75) is slightly higher than near the reaction surface (x = 0.00).
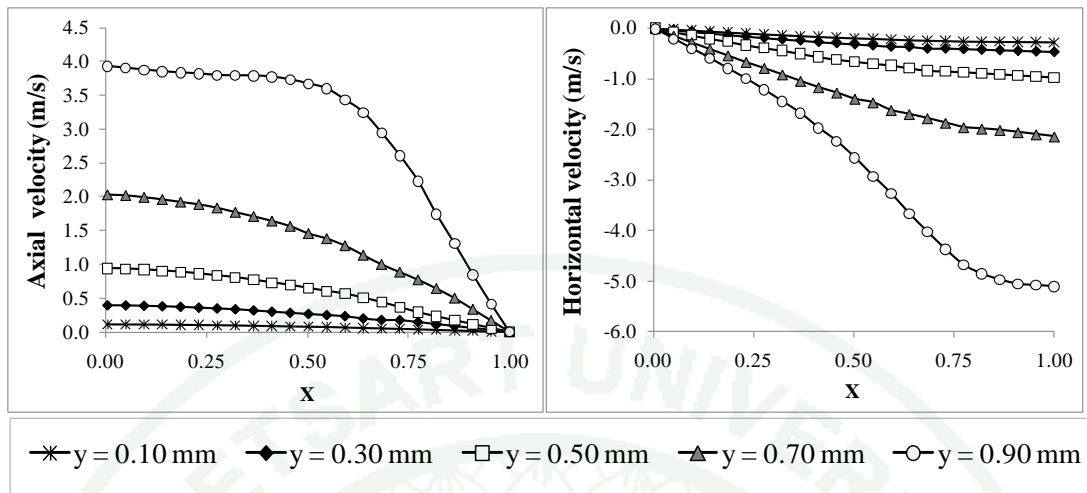
Figure 23 The axial and horizontal velocity profiles at various positions in the
entrance region (x = 0.00 - 1.00, y = 0.00 - 1.00 mm) of cathode GDL, at
no load condition.
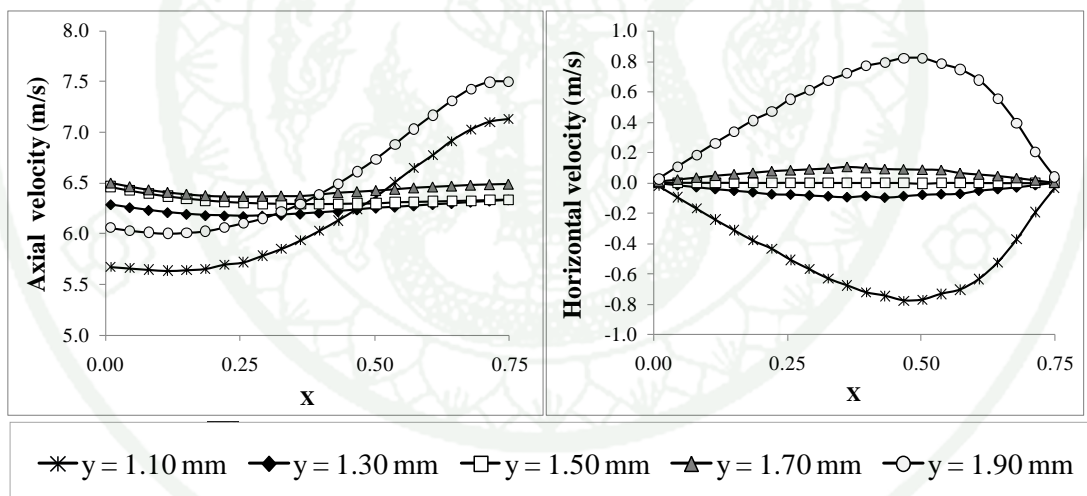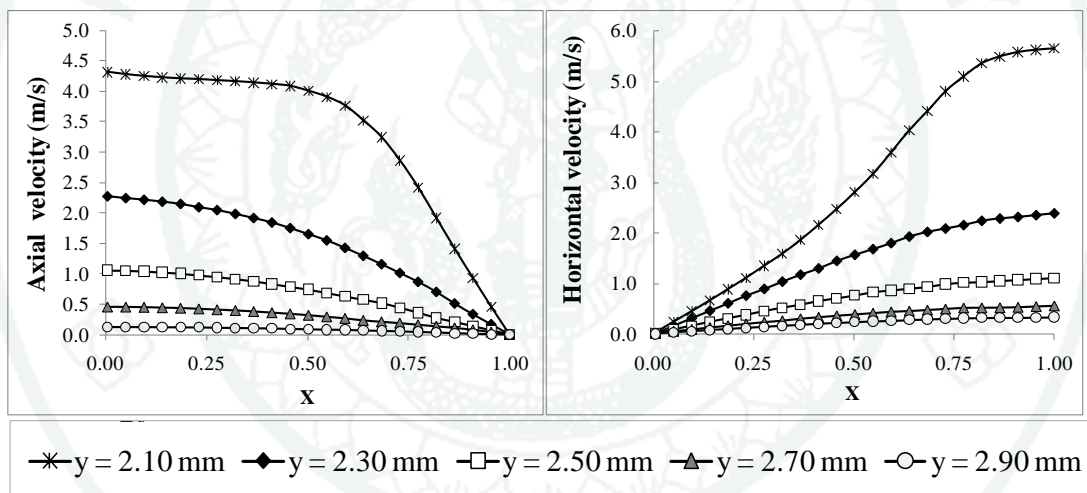

Figure 24 The axial and horizontal velocity profiles at various position in a region
between channel rib and reaction surface (x = 0.00 - 0.75, y = 1.00 - 2.00
mm) of cathode GDL, at no load condition.

The average horizontal velocity at the middle point of the region between
channel rib and reaction surface is decreased from -2.71 m/s (at x = 0.50, y = 0.90 mm
in **Figure 23**) to -0.47 m/s (at x = 0.50, y = 1.10 mm in **Figure 24**). This result shows
lower convective mass transfer to the reaction surface in this region. In the lower part

of this region (y = 1.50 - 2.00 mm), the direction of horizontal velocity is reversed. This represents the gas flowing out from the reaction surface, see **Figure 24** at y = 1.50 mm. The magnitude of horizontal velocity in the middle (x = 0.50) increases when the cathode gas flows through the GDL behind the channel rib. The gas velocity increases due to the expansion of gas at lower pressure.

When cathode gas flows into exit region (y = 2.00 - 3.00 mm), the horizontal velocity increases due to the high pressure gradient at the rib corner. The horizontal velocity decreases when the gas flow into the GDL lower edge in the exit region (y = 2.90 mm) as shown in **Figure 25**. The axial velocity also decreases when the gas flows inside the exit region.

Figure 25 The axial and horizontal velocity profiles at different position in exit region of cathode GDL, at no load condition.

When the electrical load is applied, the cathode gas velocity profiles are the same as shown in the anode side, but with lower magnitude due to less of oxygen feeding according to the stoichiometry. The velocity profiles at cathode reaction surface (x = 0.00) at various operating voltages are shown in **Figure 26**. The positive values represents the flow direction is out from the reaction surface to the GDL. Therefore, the total flux, which is resulted from the summation of the oxygen consumption flux, water production flux, and water dragging flux from anode to

cathode, is flowing out from the cathode reaction surface to the cathode GDL. It is also observed that the velocity at the entrance region is higher than the velocity at the exit region, the same as in anode side. However, at high operating voltage region of 1.15 - 0.9 V, the velocity is maximum in the entrance region (y = 0.00 - 1.00 mm) and gradually decreases to the exit region (y = 2.00 - 3.00 mm). At lower operating voltages of 0.8 - 0.5 V, the lower velocity at the entrance region (y = 0.00 - 1.00 mm) is observed. The maximum velocity occurs at the region behind the channel rib where y = 1.00 to 2.00 mm.

At cathode GDL, the high convective mass transfer can be observed at the region between channel rib and reaction surface (y = 1.00 - 2.00 mm) whereas the low convective mass transfer can be observed near the GDL upper and lower edges. The gas flowing into the catalyst surface is observed at the upper part of GDL (y = 0.00 - 1.50 mm) and the gas at the lower part (y = 1.50 - 3.00 mm) flow out from the reaction surface by convection. At the cathode reaction surface, the direction of gas flows out from the reaction surface. The velocity at reaction surface is maximized at the region between channel rib and reaction surface when fuel cell is operated at 0.8 - 0.5 V. For higher operating voltages, the maximized velocity is observed at the entrance region.

In both of anode and cathode GDLs, the high convective mass transfer are observed at the region between channel rib and reaction surface (y = 1.00 - 2.00 mm) while the low convective mass transfer are observed near the GDL upper and lower edges (y = 0.00 and 3.00 mm). The gas flowing into the catalyst surface by convection is observed at the upper part of GDL (y = 0.00 - 1.50 mm) while the gas at (y = 1.50 - 3.00 mm) flowing out from the reaction surface by convection is observed in the lower part. However, the reactant can reach the reaction surface by diccution and will be discussed later. Because of the lower gas velocity in the cathode GDL, the performance of reactant replenishing and water removing are lower.
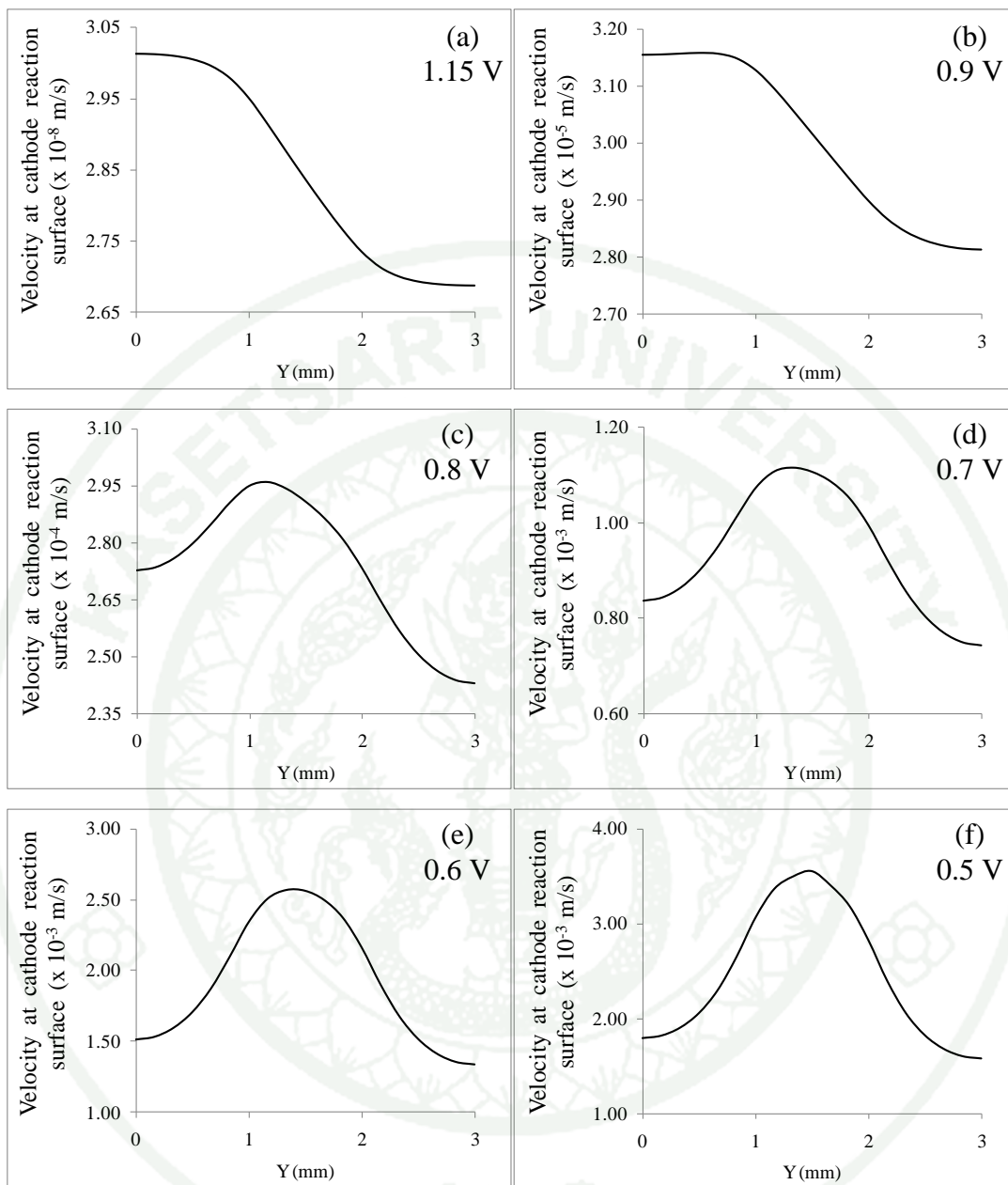
Figure 26 The velocity of gas flowing out from cathode reaction surface; (a) 1.15 V, (b) 0.9 V, (c) 0.8 V, (d) 0.7 V, (e) 0.6 V, and (f) 0.5 V.

B. Temperature distribution

The temperature distributions at various voltages are shown in **Figure 27**. The temperature distributions are in the same pattern for all operating voltages. The temperature at the cathode is higher than the temperature at the anode due to higher heat generated from electrochemical reaction at cathode side. The high heat generated is observed at the reaction surface behind the channel rib (y = 1.00 - 2.00 mm) on both anode and cathode, as shown in **Figure 28**. However, the high temperature zone occurs at the reaction surface behind upper and lower channels. The heat flux vector profiles in GDLs and membrane at operating voltage of 0.5 V are shown in **Figure 29**. In the anode and cathode GDLs, the heat flux are from reaction surfaces to the channel ribs on both anode and cathode side. The higher heat flux is observed near the channel rib and the upper and lower edge while the lower heat flux is observed in GDL opposite the upper and lower flow channels. Therefore, the removals of heat at the reaction surface near the upper and lower flow channels are less than the other regions. Since the heat removal rates behind the flow channels are less than the heat generated at the reaction surfaces in corresponding regions, the temperature behind the flow channels is high. The temperature behind the channel rib is lower because the reaction surface is close to the channel rib. Thus heat removal rates at GDL behind the channel rib are higher than that behind the flow channel.

In the membrane, the heat flows from cathode to anode because the higher temperature is higher at cathode reaction surface. The heat flux direction is toward the membrane surface behind the anode channel rib. The higher heat flux is observed in GDL behind the channel rib while the lower heat flux is observed in GDL behind the upper and lower flow channels. Thus the heat transfer rate behind the flow channels is less than that behind the channel ribs which results in higher temperature behind the flow channels. The maximum temperature is behind the cathode flow channels. The gradient of temperature across the membrane between anode and cathode increases with the fuel cell voltage. Higher energy losses to heat increases inversely with operating voltages which intern decreases inversely with the electrical load applied.
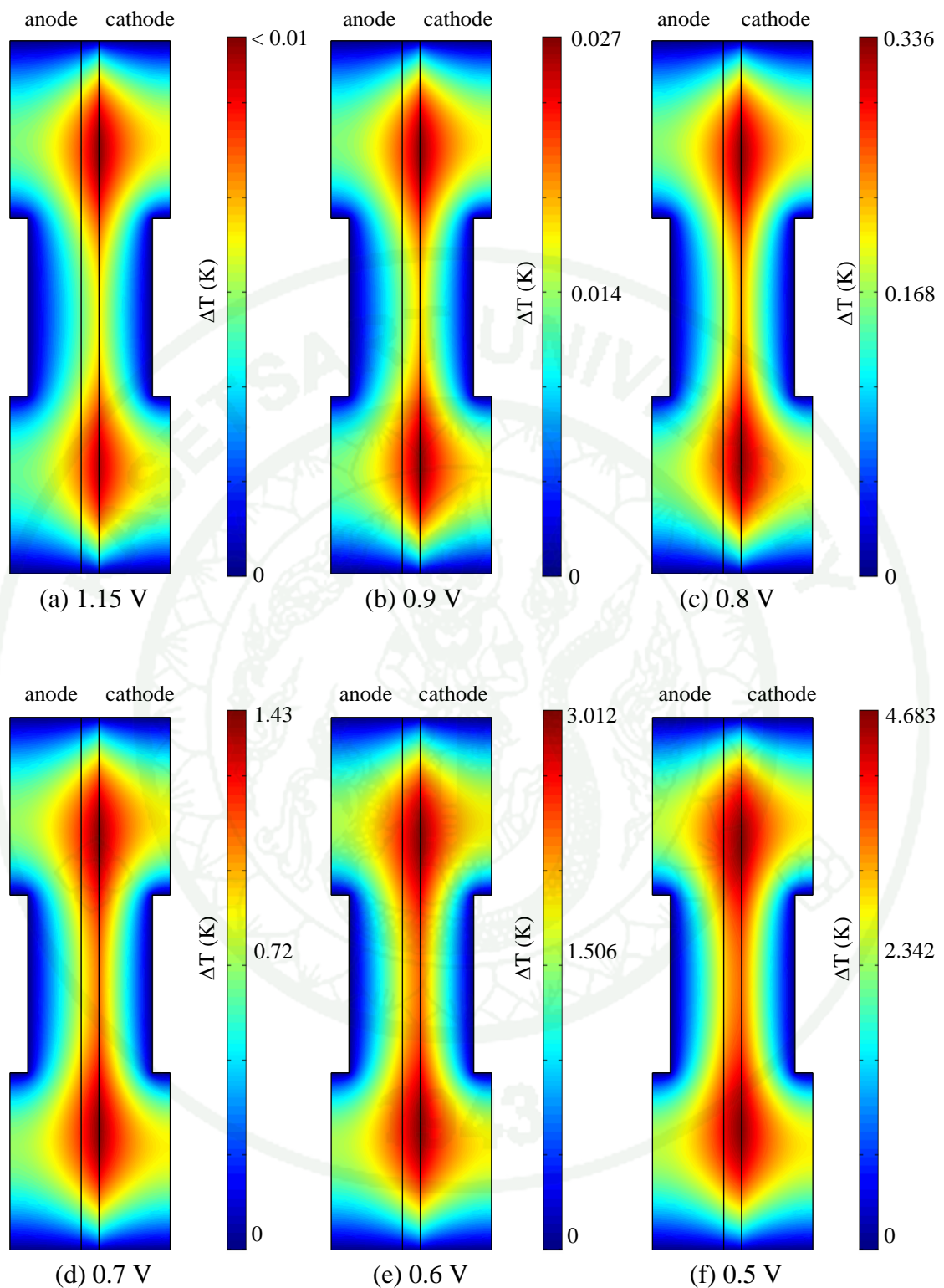
Figure 27 Comparison of temperature distribution at various fuel cell voltages; (a)
1.15 V, (b) 0.9 V, (c) 0.8 V, (d) 0.7 V, (e) 0.6 V, and (f) 0.5 V. Note that
the temperature at the rib is 353.15 K and the color shade shows the
temperature rise above the rib temperature at each point.
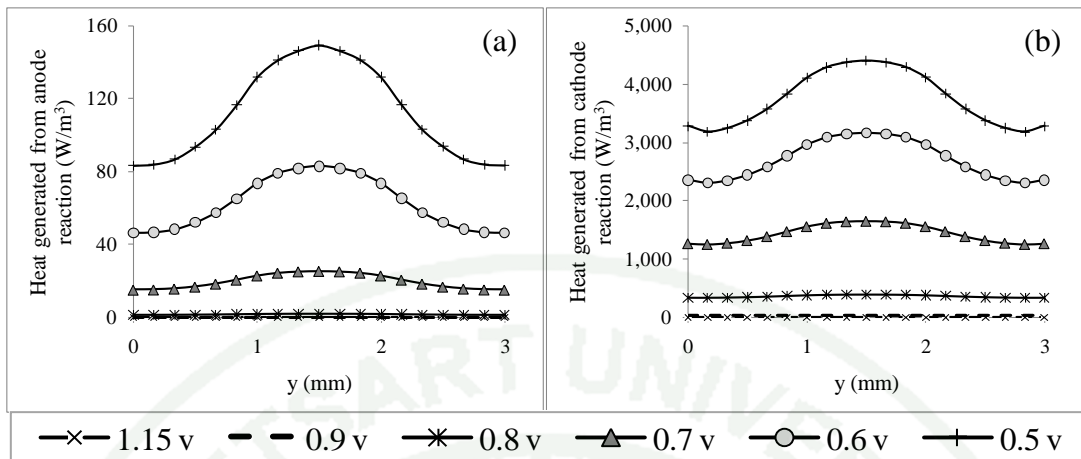
Figure 28 The heat flux reaction surfaces at various operating voltages; (a) anode, and (b) cathode.
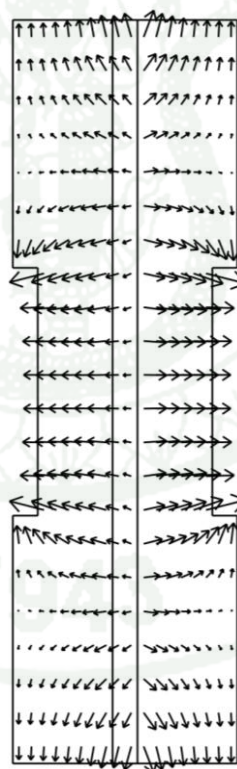

Figure 29 The heat flux vector at operating voltage of 0.5 V. The pattern of heat flux profile is the same for all operating voltages.

C. The distributions of hydrogen and water vapor in anode GDL

The hydrogen mole fraction distributions at various fuel cell voltages in anode gas diffusion layer are shown in **Figure 30**. At high fuel cell voltage (low current density), the hydrogen mole fraction distributions are nearly the same with lower magnitude. For 1.15 V, a hydrogen mole fraction is higher at the reaction surface near the entrance, and decrease to the bottom part of GDL. In the upper part, the hydrogen diffusion flux out from reaction surface to GDL's bulk and then removed by the convection (see **Figure 53, Appendix A**). While in the lower part, the hydrogen diffuses to the reaction surface.

When the current density was increased, more hydrogen was consumed by the electrochemical reaction. The high hydrogen mole fraction near reaction surface is observed although it was consumed at reaction surface (see **Figure 30** (c)-(f)) due to the water transport in the PEM fuel cell. When the current density is increased, the more water molecules were dragged from anode to cathode via electro-osmotic drag. These cause the decreasing of water fraction and the increasing of hydrogen mole fraction near the reaction surface behind the channel rib at high current density. The hydrogen diffusive flux out from the reaction surface is also observed and increases when the fuel cell voltage drop (see **Figure 54, Appendix A**). This can decrease the hydrogen mole fraction at reaction surface and cause the mass transport loss at higher current density, however, this study did not go to that limitation. The diffusive flux of hydrogen into the reaction surface is observed near reaction surface in exit region but decrease with current density (see **Figure 55**, **Appendix A**).

The water mole fraction in anode GDL is shown in **Figure 31**. At high operating voltage (low current density), the higher water mole fraction is observed near reaction surface behind the lower flow channel. When the operating voltage decreases (higher current density), the concentration of water is decrease due to the transport of water from anode to cathode. Theses cause the increasing of the water back diffusion from the cathode.
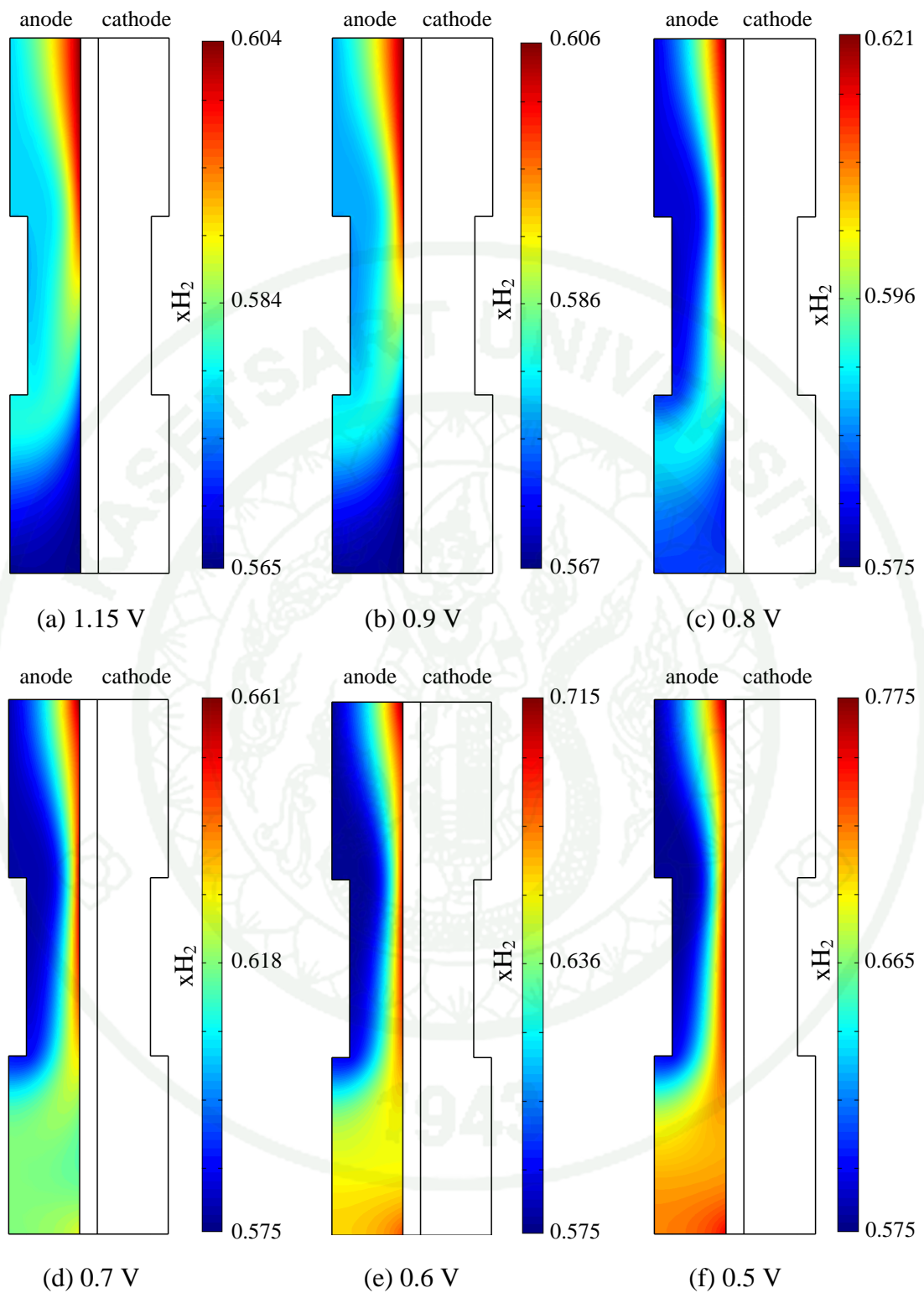
Figure 30 The comparison of hydrogen mole fraction at various fuel cell voltages; (a) 1.15 V, (b) 0.9 V, (c) 0.8 V, (d) 0.7 V, (e) 0.6 V, and (f) 0.5 V.
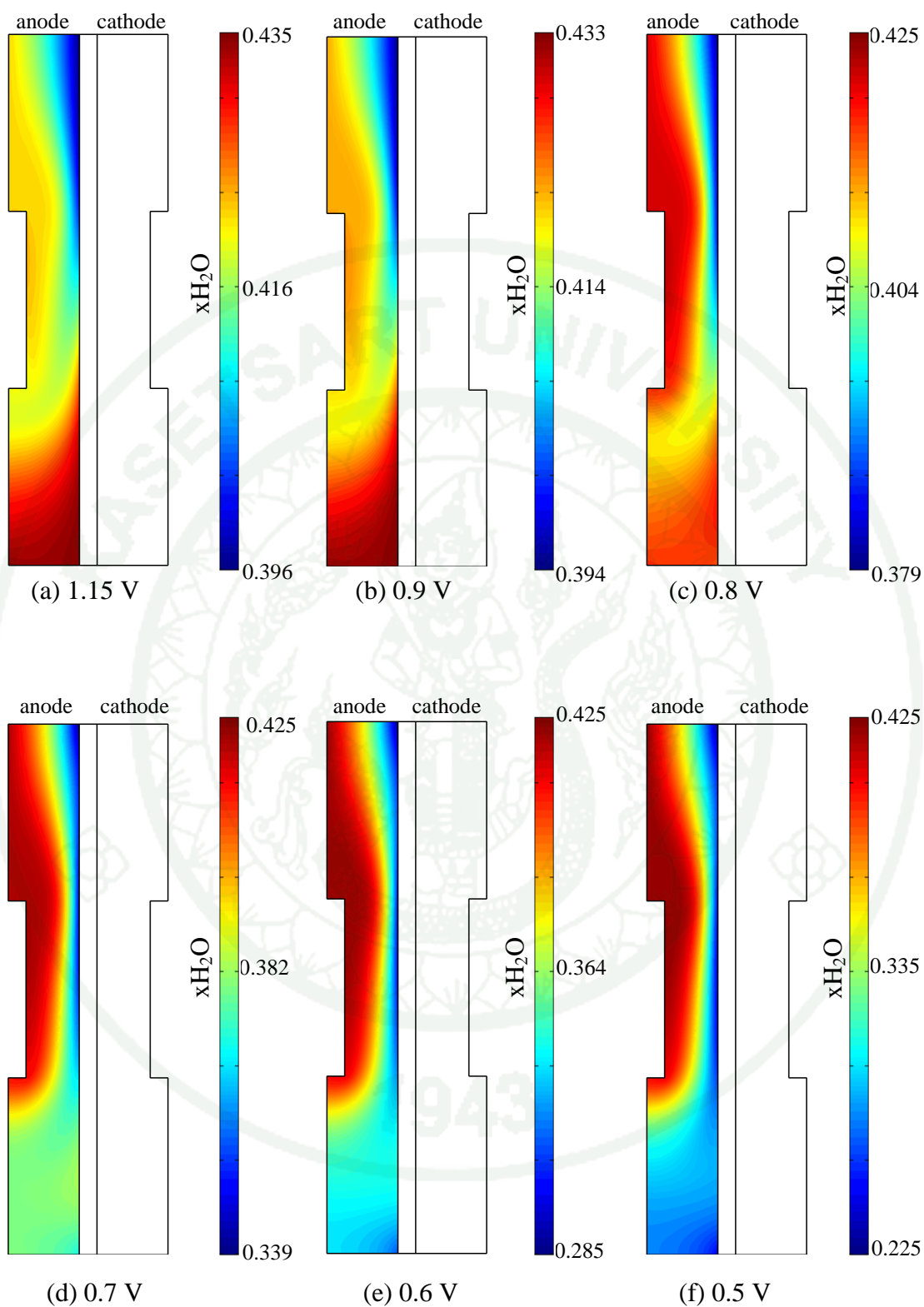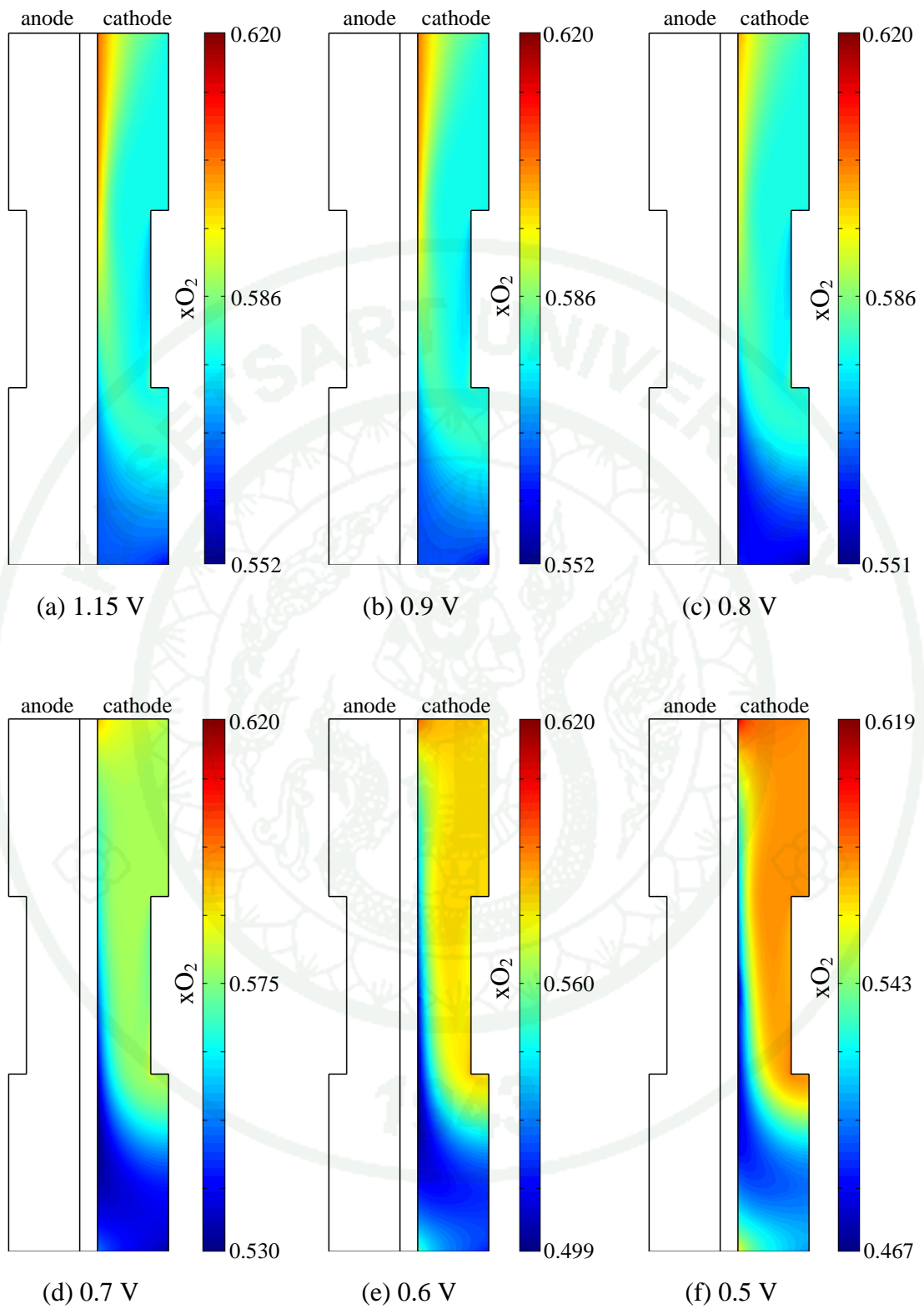
Figure 31 Water mole fraction in anode GDL at various operating voltage;(a) 1.15 V, (b) 0.9 V, (c) 0.8 V, (d) 0.7 V, (e) 0.6 V, and (f) 0.5 V.

D. The distributions of oxygen and water vapor in cathode GDL

The oxygen mole fraction distribution in cathode GDL is shown in **Figure 32**. In **Figure 32** (a)-(b), the high oxygen mole fraction are observed at the reaction surface near the entrance. When the operating voltage is decreased, the consumption of oxygen gas is increased and causes the decreasing of oxygen mole fraction as observed in **Figure 32** (c) - (f). The decreasing of oxygen mole fraction at the entrance and exit region are more rapid than the core region because the low gas convective flow near the edge zone cannot replenish the fresh gas effectively. However, the oxygen mole fraction nears the inner corner of GDL not much lower at low voltage. The decreasing of oxygen at near reaction surface improves the diffusion of oxygen into the reaction surface. The oxygen diffusion flux into the reaction surface increase when increase the current load and the high oxygen diffusive flux is observed near the reaction surface behind the channel rib (**Figures 62-64, Appendix A**).

The water concentration distribution in cathode GDL is show in **Figure 33**. While the water mole fraction in the bulk of GDL is nearly constant at saturation level, the higher water concentration region is observed in the GDL near the reaction surface and near the bottom edge at low voltage. Therefore there is high chance to observe that the water produced from the reaction and the electro-osmotic drag form a water droplet at the reaction surface and cause the water flooding effect in these zones. Due to the lower mole fraction of water in the bulk GDL, the water fluxes into the bulk GDL by diffusion and can be removed out by the convective flux of bulk gas. Thus the removal of water can be improved by decrease the water mole fraction in the bulk GDL which can increase the diffusive flux of water out from the reaction surface.

Figure 32 The comparison of oxygen mole fraction at various operating voltage;
(a) 1.15 V, (b) 0.9 V, (c) 0.8 V, (d) 0.7 V, (e) 0.6 V, and (f) 0.5 V.
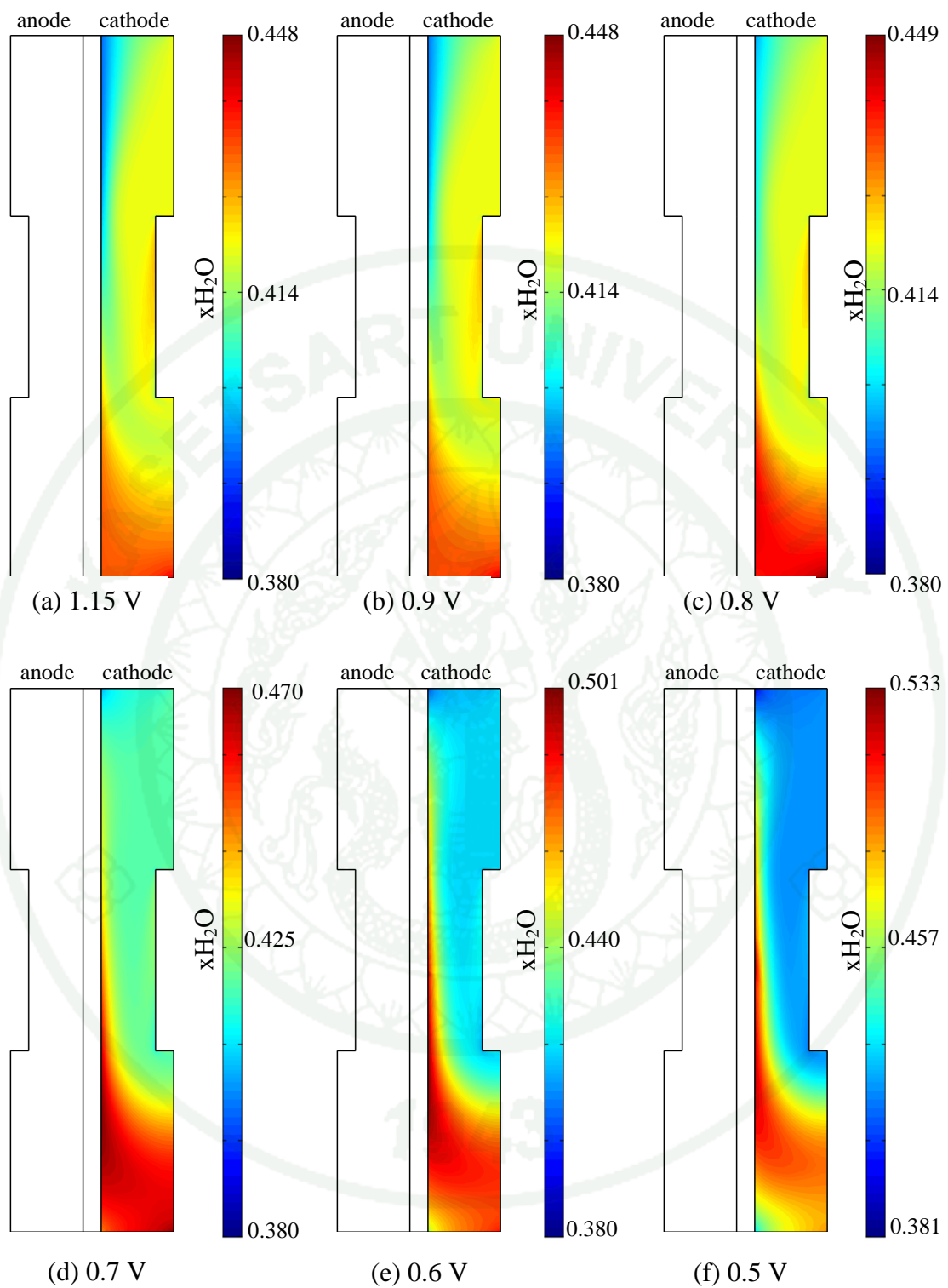
Figure 33 Water mole fraction in cathode GDL at various operating voltage;
(a) 1.15 V, (b) 0.9 V, (c) 0.8 V, (d) 0.7 V, (e) 0.6 V, and (f) 0.5 V.
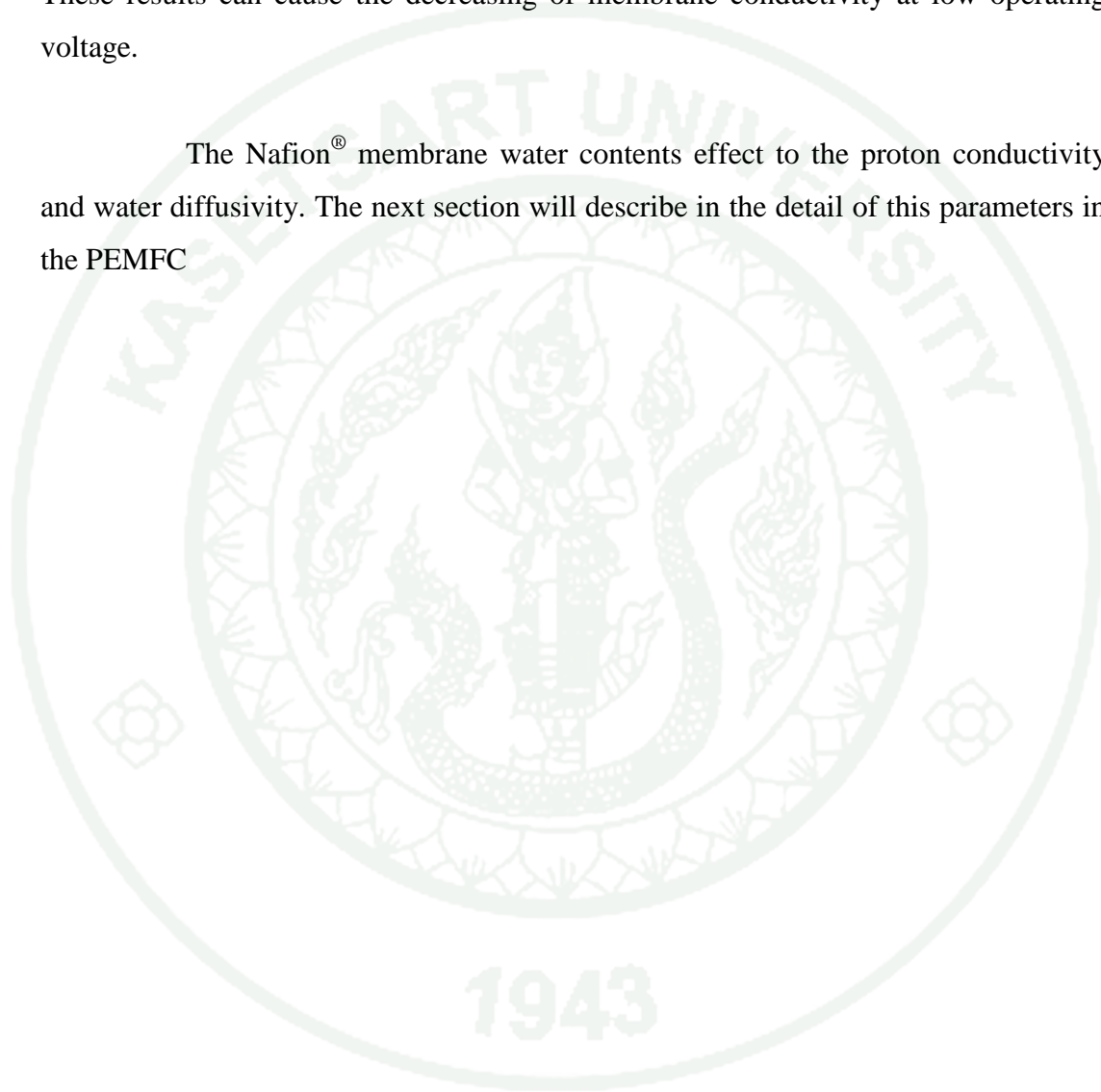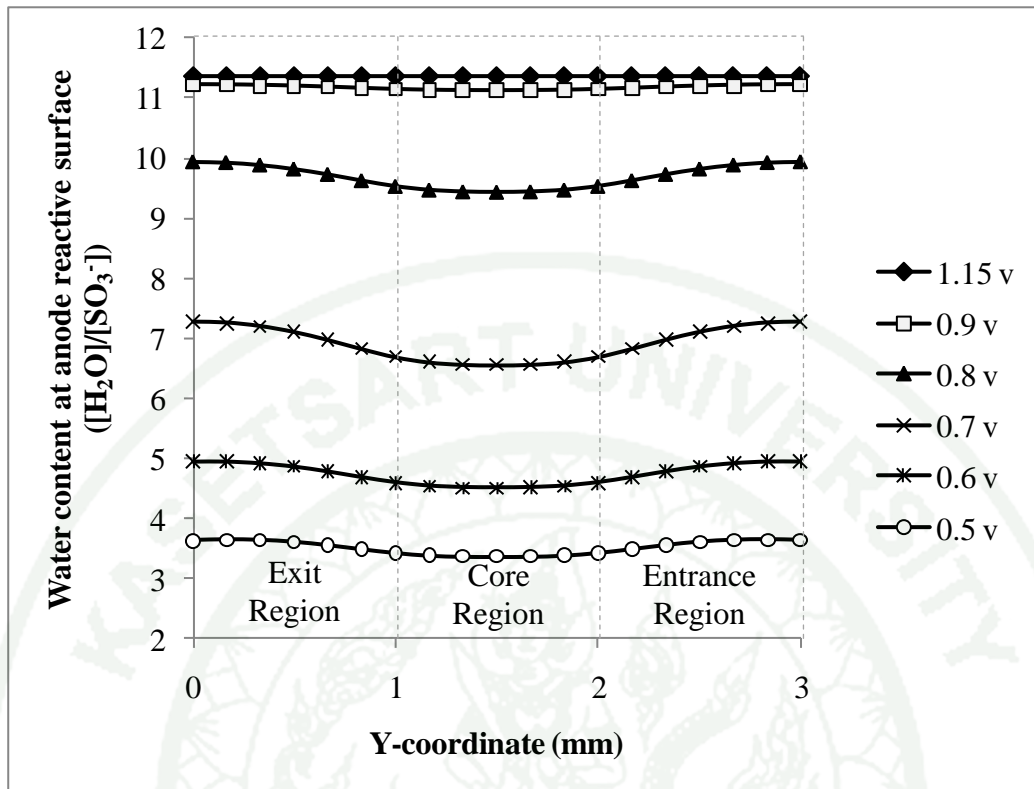
E. Water content in Nafion® membrane

Water content in Nafion® membrane is defined as a ratio between the number of water molecules per a sulfonate ion, $[H_2O]/[SO_3^-]$. The water content in Nafion® membrane at various voltages is shown in **Figure 34**. At fuel cell voltage of 1.15 V, the water content in membrane is distributed fairly regularly. The average water content is 11.363. Distribution of water content in membrane is more distracting when fuel cell voltage is decreased, see **Figure 34** (b) - (f). When fuel cell voltage is decreased lower than 0.9 V, the water content decrease at anode side and increase at cathode side, especially at the middle of membrane where almost proton current pass through.

The water contents at the membrane surface at various operating voltages are shown in **Figures 35** and **36** for anode and cathode side. The water content at anode membrane surface is decreasing in the same manner when the operating voltage is decreased. The water content at the middle of membrane is lower than the edge slightly. At cathode side, the water content is increased irregularly when operating voltage is decreased. When operating voltage is decreased from 1.15 - 0.8 V, the water content at cathode membrane surface increase slightly. Whereas if the operating voltages are 0.7 – 0.5 V, the water content at cathode membrane surface is increased at the middle part of membrane and decreased at the entrance and exit region.

The flux of water flowing through the membrane cause from the electro-osmotic drag which drag water molecules from anode to cathode, and water back diffusion which conduct water molecules from cathode to anode. When the water back diffusion is dominated, the water content at cathode membrane surface decrease slightly from 1.15 - 0.9 V. When fuel cell operated at 0.8 - 0.5 V, the electro-osmotic drag is dominated and results in net water transport from anode to cathode in the core region. Therefore the water content at cathode membrane surface is increased. At entrance and exit regions, the water back diffusion is more effected. Therefore the net water transport is from cathode to anode and cause decreasing of water content at cathode membrane surface in these regions. At fuel cell voltage of 0.5 V, the water

content at core region does not increase anymore because the effect of water back diffusion is high enough for challenging the electro-osmotic drag. Therefore the water content at cathode membrane surface is limited while the water content at anode membrane surface continues to decrease when the operating voltage is decreased. These results can cause the decreasing of membrane conductivity at low operating voltage.

The Nafion[®] membrane water contents effect to the proton conductivity and water diffusivity. The next section will describe in the detail of this parameters in the PEMFC
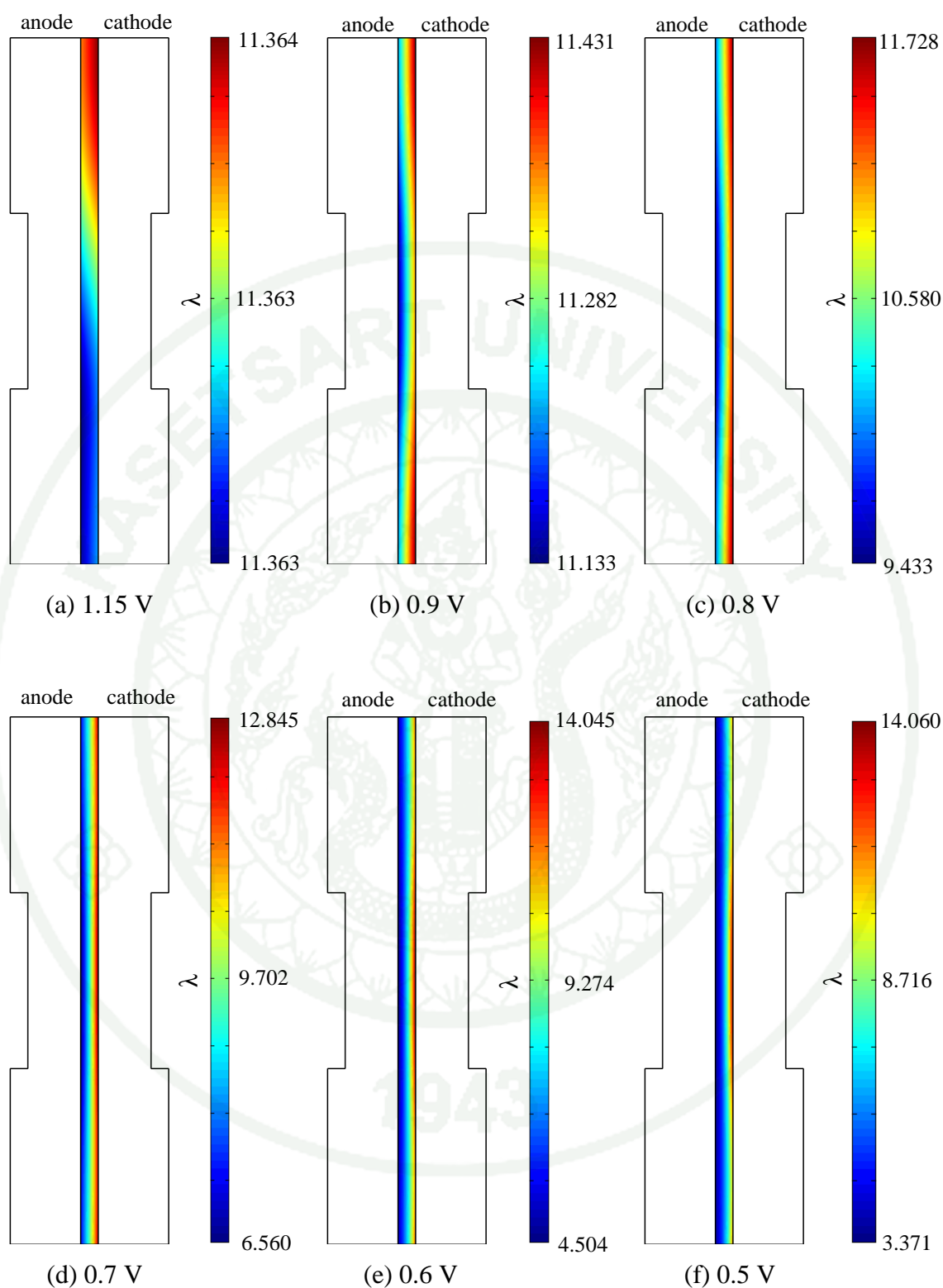
Figure 34 Water content in Nafion® membrane at various operating voltages;
(a) 1.15 V, (b) 0.9 V, (c) 0.8 V, (d) 0.7 V, (e) 0.6 V, and (f) 0.5 V.

Figure 35 Water content (λ) at anode membrane surface.
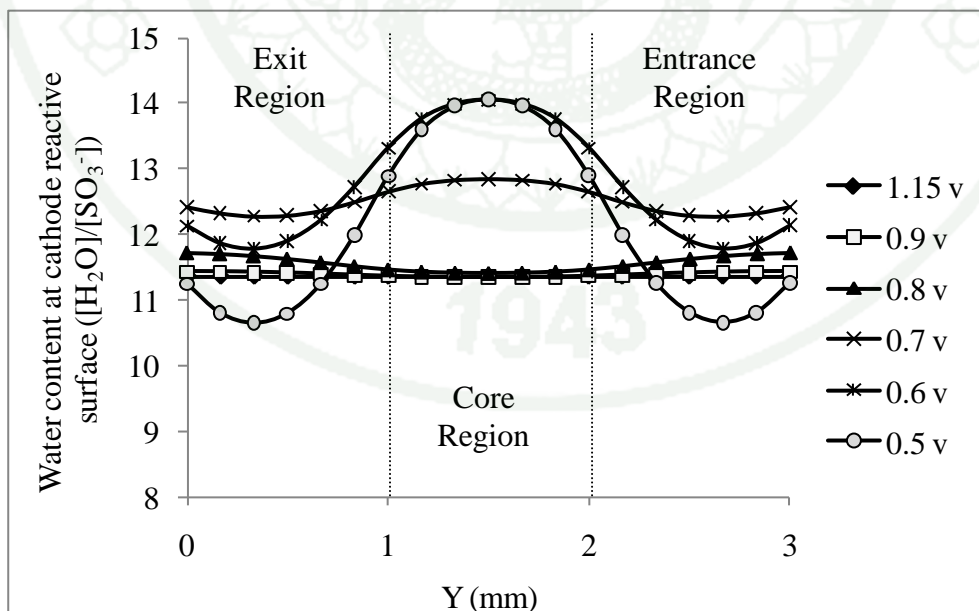
Figure 36 Water content (λ) at cathode membrane surface.

1. The proton conductivity

The conductivity of Nafion® membrane at various operating voltage are shown in **Figure 37**. The distribution of proton conductivity is similar to the membrane water content. The proton conductivity is uniform distribution at 10.1 S/m when the operating voltage at no load condition. When operating voltage is decreased, the proton conductivity decreases at anode, and increases at cathode. The decreasing of proton conductivity causes the increasing of ohmic losses of PEM fuel cell by the increasing of membrane resistance.

2. Water diffusivity (D_λ)

Figure 38 represents the water diffusivity at various fuel cell voltage. The diffusivity is uniform when the operating voltage is 1.15 V. When the operating voltage is decreased to 0.9 V, the water diffusivity at the middle of membrane is slightly decrease at anode side while it increase at the cathode side of membrane near entrance and exit region. The water diffusivity at anode begins to increase at operating voltage of 0.7 V. At 0.7 - 0.5 V, the water diffusivity at anode membrane surface is higher than at the cathode membrane surface along the length of membrane. The high water diffusivity is observed near the entrance and exit region on anode side.
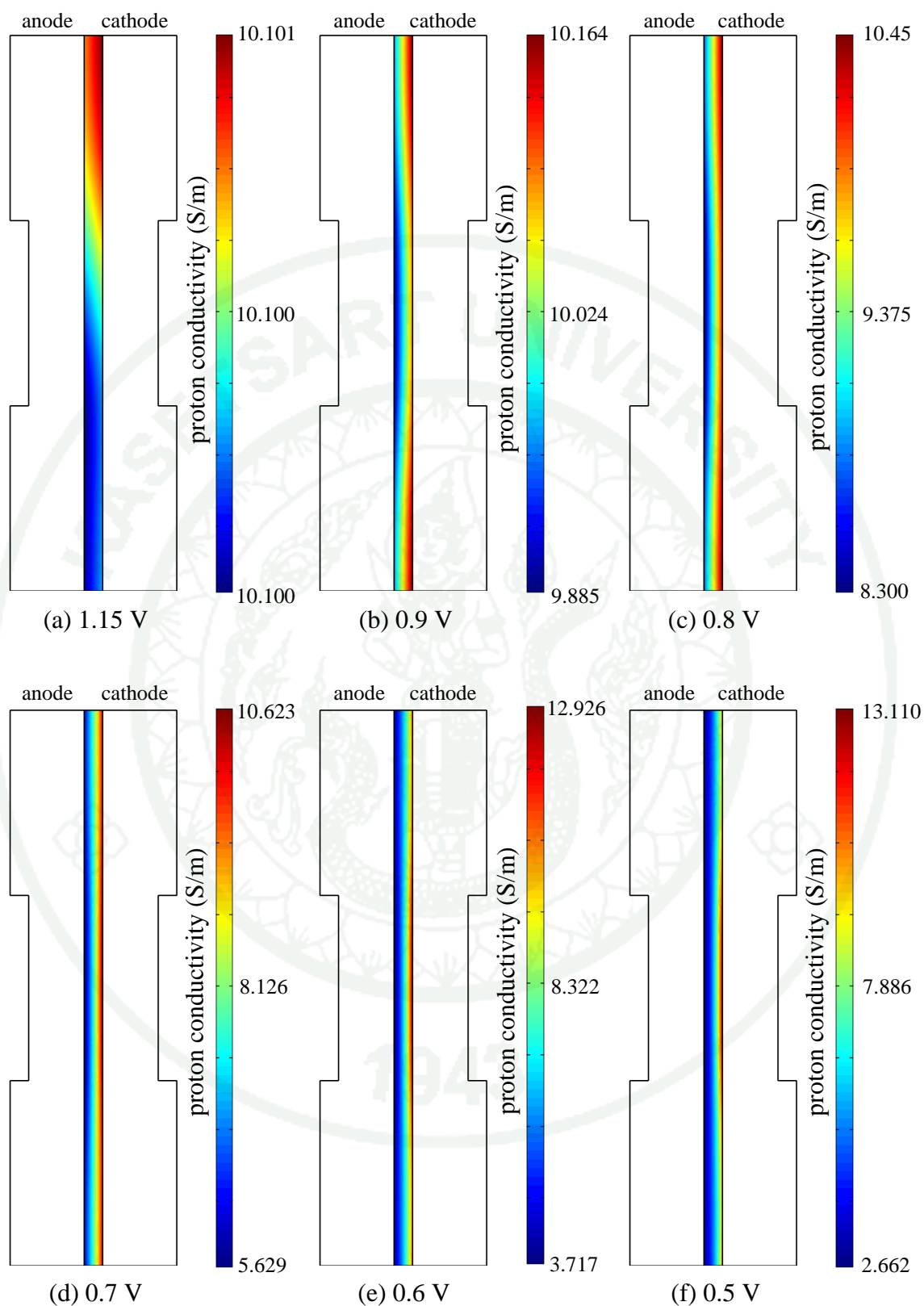
Figure 37 The proton conductivity in membrane at various operating voltages;
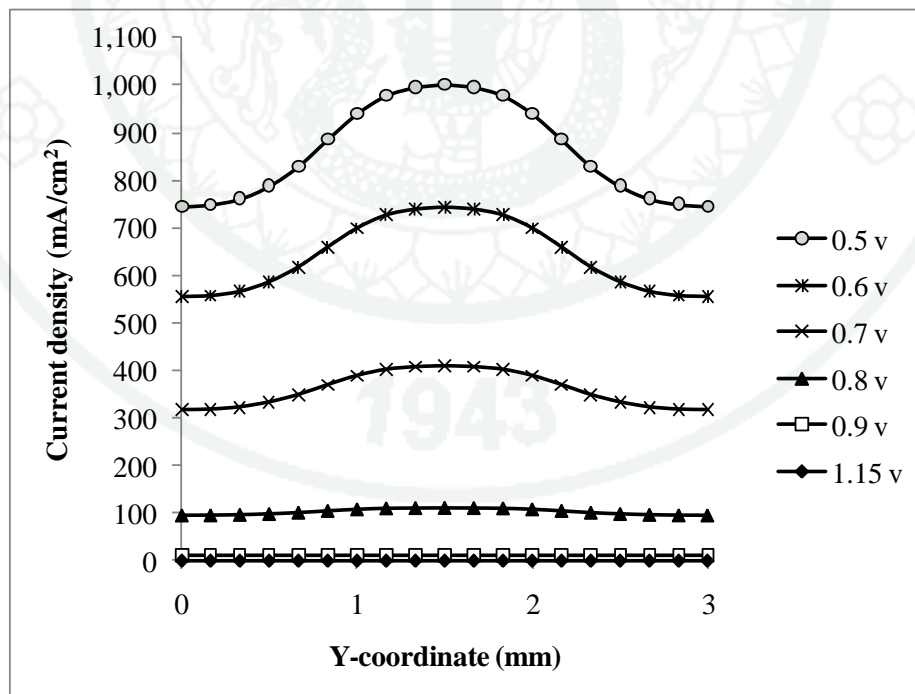(a) 1.15 V, (b) 0.9 V, (c) 0.8 V, (d) 0.7 V, (e) 0.6 V, and (f) 0.5 V.
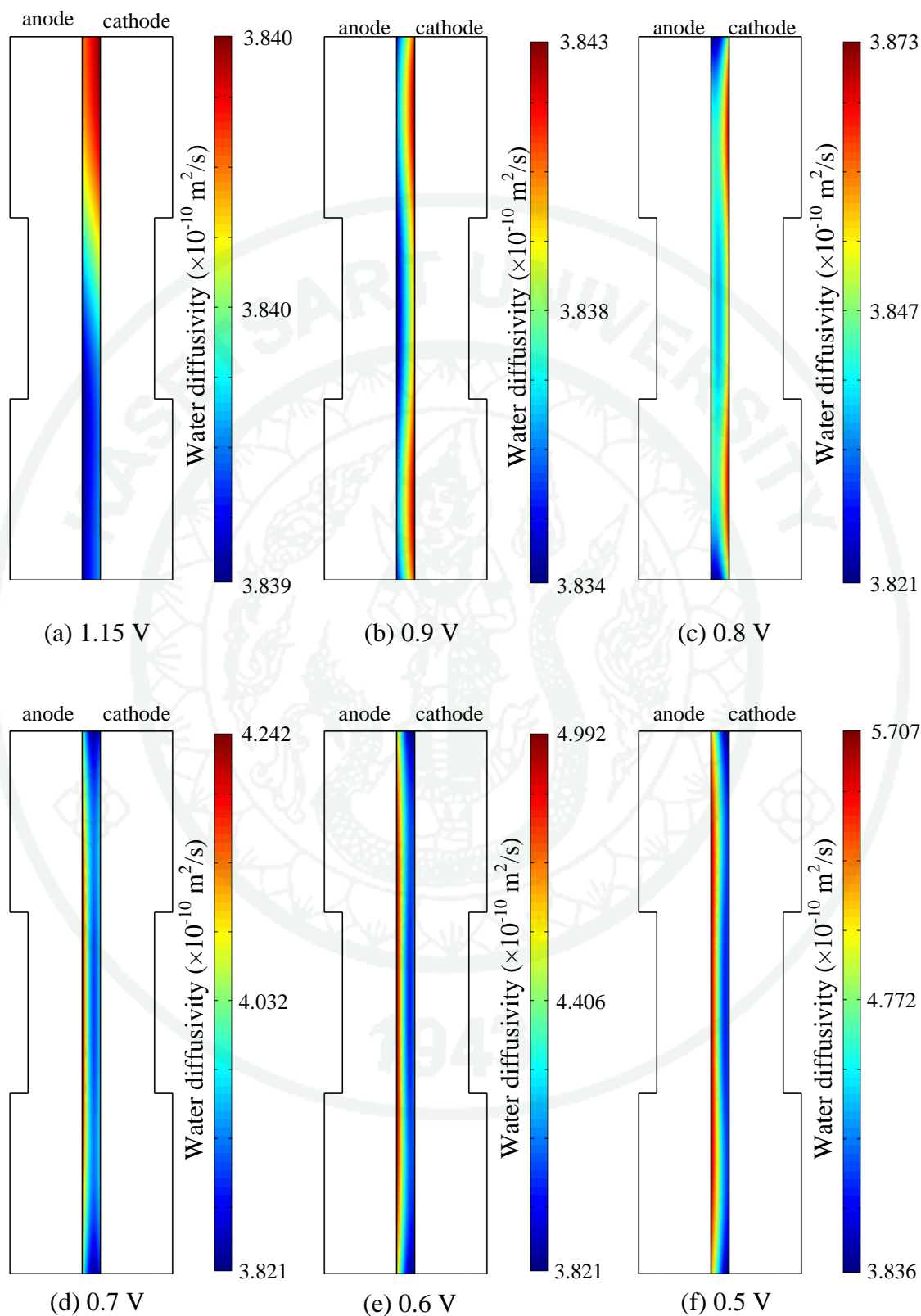
Figure 38 The water diffusivity in Nafion® membrane at various operating voltages;
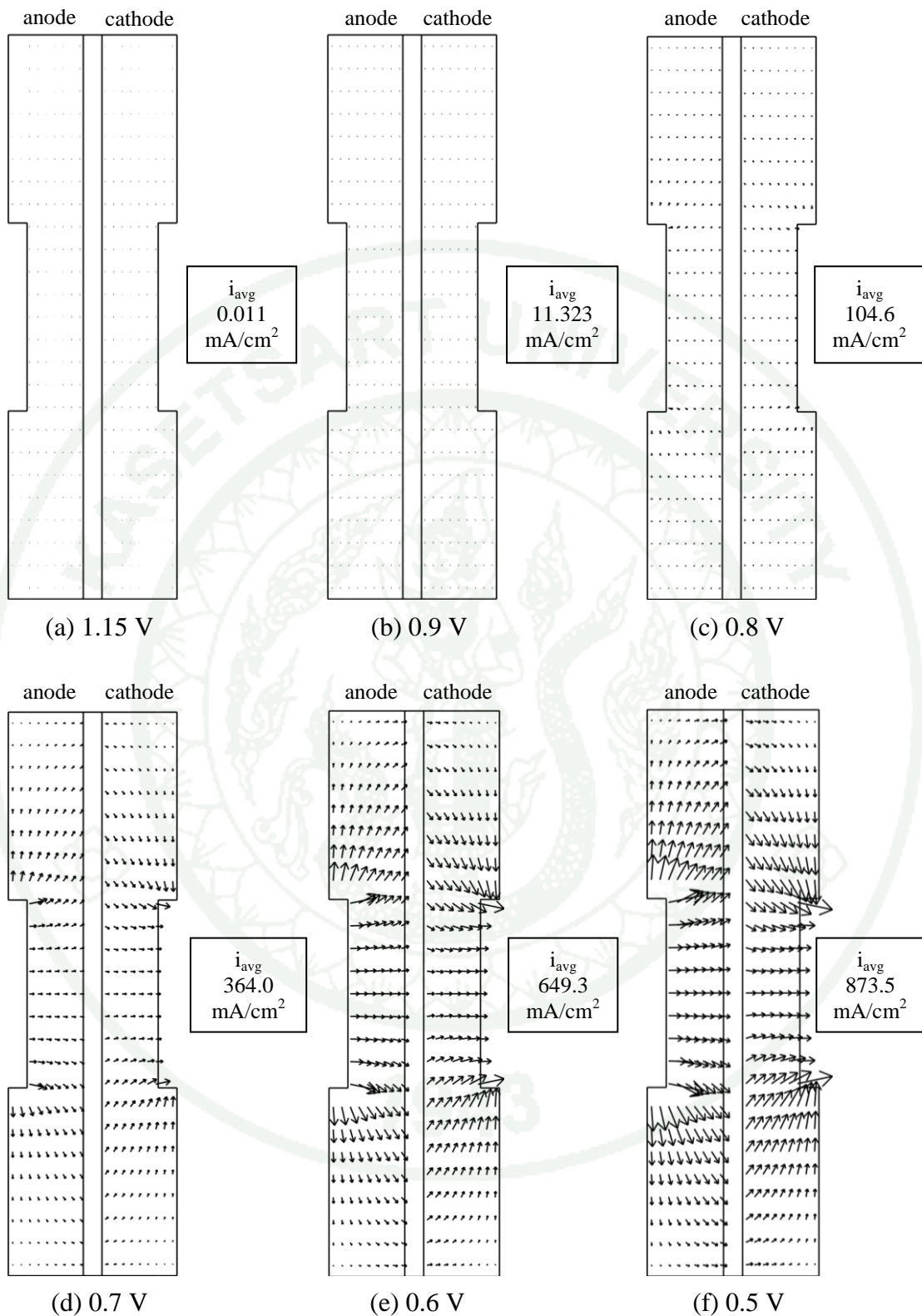(a) 1.15 V, (b) 0.9 V, (c) 0.8 V, (d) 0.7 V, (e) 0.6 V, and (f) 0.5 V.

F. Charge distribution in gas diffusion layer

The current density distribution at reaction surface is shown in **Figure 39**. At 1.15 - 0.9 V, the current density distribution is uniform along the reaction surface. At 0.8 - 0.5 V, the current production rate is higher in the middle zone and lower in the entrance and exit region. The current density at entrance region is slightly higher than the current density at exit region.

The current density vector in gas diffusion layer is shown in **Figure 40**. At anode side, the channel rib act as a current source and reaction surface act as a current sink. On the other side, at cathode, reaction surface act as a current source and the channel rib act as a current sink. The maximum of current flux is observed on the channel rib corner while the minimum current flux is observed near the top and bottom edge of gas diffusion layer. For all operating voltage, trend of current density profile are the same but their magnitude are difference.

Figure 39   The comparison of current density profile over the reaction surface at various voltages.
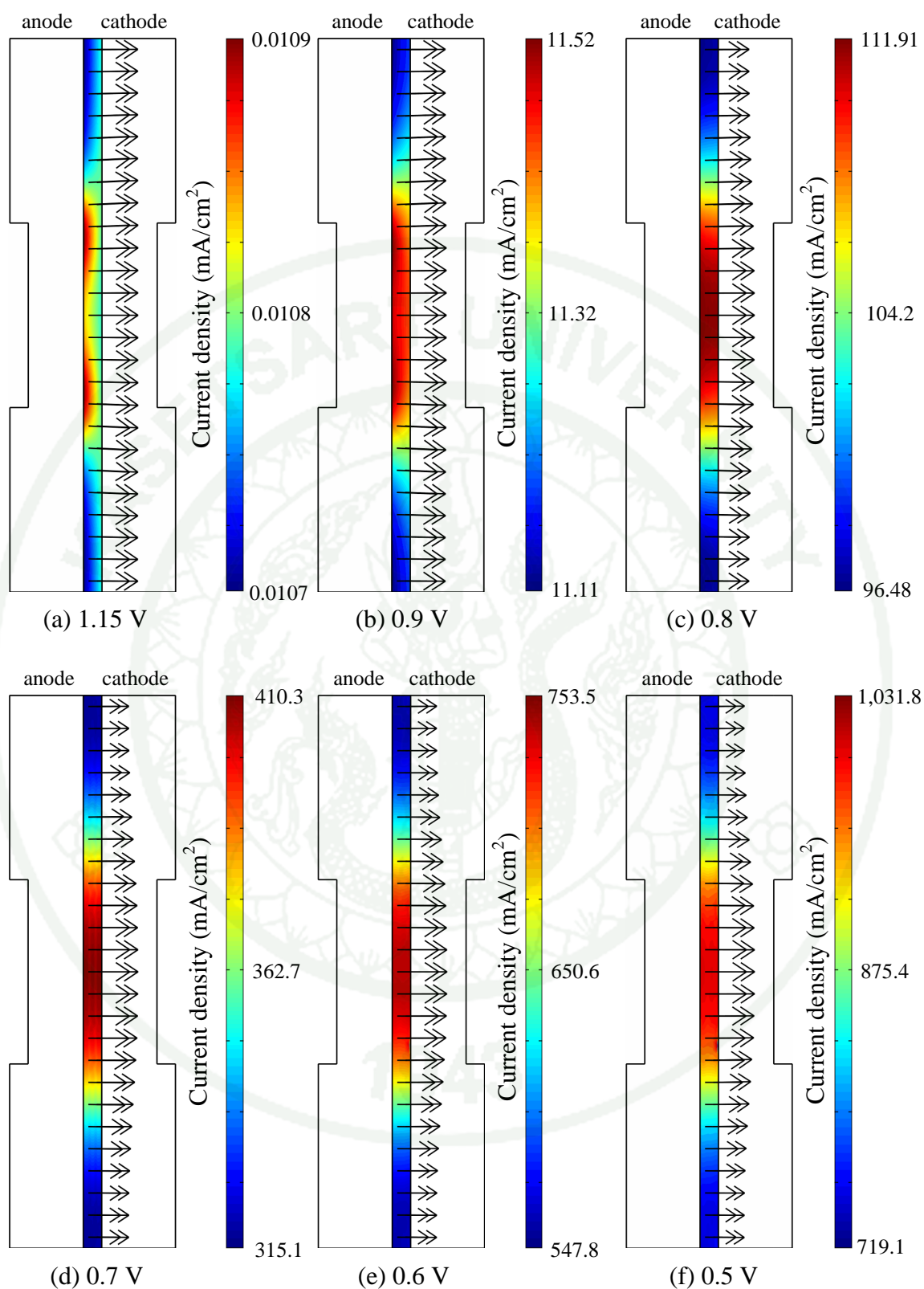
Figure 40 The current density distribution in GDL at various operating voltages;
(a) 1.15 V, (b) 0.9 V, (c) 0.8 V, (d) 0.7 V, (e) 0.6 V, and (f) 0.5 V.

G. Charge distribution in Nafion® membrane

The current density distribution at various operating voltage is shown in **Figure 41**. At 1.15 V, high current density is observed at the membrane near channel rib at anode. In the middle of the membrane, the current density at anode is higher than the current density at cathode. At the top and bottom part of membrane, in contrast, the current density at anode is lower than the current density at cathode. At 0.9 V, the high current density is observed on both anode and cathode side in the middle of membrane. The high current density is observed only at the middle part of membrane which line in the same position with channel rib when the operating voltages are 0.8 − 0.5 V. It also observed that the current density distribution is unchanged in the y-axis in these operating voltages.

The next section is a discussion of polarization at difference operating temperature. Understanding of hydrodynamics is useful in discussion about polarization in each region

Figure 41 The current density distribution in membrane at various operating
voltages; (a) 1.15 V, (b) 0.9 V, (c) 0.8 V, (d) 0.7 V, (e) 0.6 V, and (f) 0.5
V.

2. PEMFC performance at difference operating temperature.

The polarization curves of simulation and experimental results (Leelasupakorn, H., 2008) at various operating conditions are shown in the **Figure 42** and the power densities at various current densities of simulation and experimental results are shown in **Figure 43**. The polarization curves at different operating temperature are presented. The fuel cells are operated at $80^{\circ}C$, $70^{\circ}C$ and $60^{\circ}C$ with 100% relative humidity for both anode and cathode gases. The catalyst loading is 0.2 mg/cm^2. Fuels are hydrogen and oxygen for anode and cathode respectively. In an experiment, hydrogen flow rate was 0.2 l/min while oxygen flow rate was 0.1 l/min. The pressure drop along the flow channel does not affect much to the performance of the fuel cell, see **Appendix E**. For save the computational time, the inlet pressure is assumed to be 1.1 times of outlet pressure (atmosphere) because the solution is more stable at this pressure drop value.

The simulation results do not fit well with the experiment because of the limitation of the Butler-Volmer equation which is used in this simulation. The maximum error obtained is 0.17 volts. Because the reaction is heterogeneous, the decreasing of reactant concentration when it reaches to the catalyst surface can affect to the rate of the reaction. The Butler-Volmer equation should be modified by the term of reactant concentration to get better results.

From the simulation, at low current density (less than 400 mA/cm^2), the fuel cell voltages decrease when the temperature increase. This occurs because the reversible voltage at low temperature is higher than at higher temperature. The discussion of open circuit voltage is presented later in section A. At higher current density (more than 400 mA/cm^2), the performance of fuel cell decreases when the temperature is raised. This cause from the increasing of membrane resistance due to the drying of membrane at anode side. The discussion of the increasing of ohmic losses is presented in section C. The simulation results at current density higher than 400 mA/cm^2 is agree with experiments.

The simulation consists of two kinds of voltage losses, activation and ohmic losses, thus the polarization curves do not go to mass transport region. However, there are the other losses such as hydrogen cross-over loss, internal short-circuit current loss, mixed potential at open-circuit voltage, and contact resistance. The voltage losses had not been cleared up yet. In this simulation, the effects of open circuit voltages, activation losses, and ohmic losses to the performance of fuel cell are discussed.
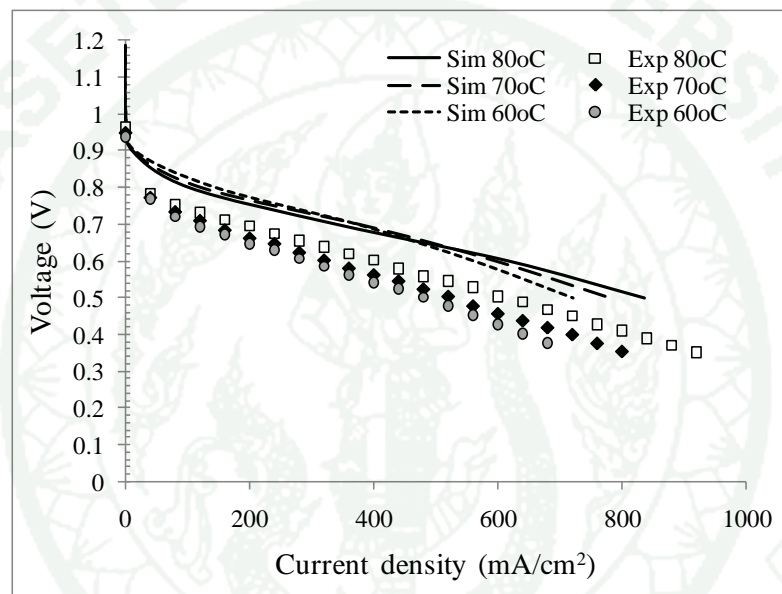
Figure 42 The polarization curves from simulation and experimental results. The operating temperatures are as follow: 80°C, 70°C, and 60°C. Note that the humidified temperature is the same as operating temperature. The experimental result is obtained from Leelasupakorn (2008).

The open circuit voltages from simulation and experiment at various temperatures are shown in **Figure 44**. The theoretical open circuit voltages are higher than actual operating open circuit voltages for temperatures range between 333.15 – 353.15 K. At OCV, the activation loss and ohmic loss is minimum, therefore the decreasing of open circuit voltage occurs by the other losses. Theoretically, open circuit voltage is decreased with increasing of temperature. However, the experiment

results in opposite way, the actual open circuit voltage is increase with operating temperature.
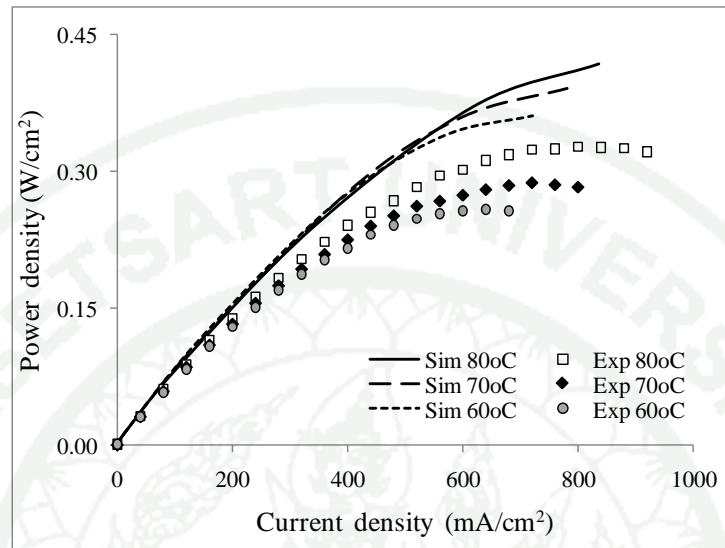
Figure 43 The power density of simulation and experimental results. The operating temperatures are as follow: 80°C, 70°C, and 60°C. Note that the humidified temperature is the same as operating temperature. The experimental result is obtained from Leelasupakorn (2008).

A. Open Circuit Voltage (OCV)

The explanation about the decreasing of open circuit voltage from the theoretical value does not clear up yet. There are many literatures propose the cause of this problem and can be conclude as follows;

1. Laraminie and Dicks (2000) suggest that the electrolyte supports an amount of electronic conductivity, so that small short-circuiting currents are possible. They propose that hydrogen crossover supports an internal current which can cause activation overpotential of around 0.3V at the cathode.
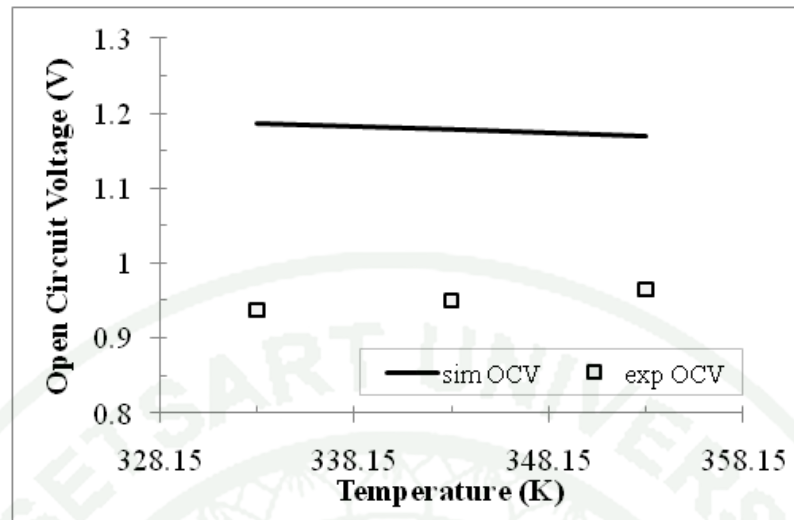
Figure 44 Comparison of experimental results and simulation results of open circuit voltage at difference operating temperature. The experimental result is obtained from Leelasupakorn (2008).

2. Zhange et al (2006) have done the experimental investigation on the effect of temperature on OCV and concluded that the decreasing of OCV is due mainly (135mV at 80 ∘C) to the Pt/PtO catalyst surface, called mixed potential, and secondarily (56mV at 80 ∘C with Nafion 112) to hydrogen crossover. And the total amount of overpotential at OCV about 0.2 V.

3. Sompalli et al (2007) have studied on membrane degradation and OCV. They found that membrane thinning and pinhole formation leads to an increase in hydrogen crossover and consequently a decline in OCV. The OCV is higher at lower relative humidity, due to the lower hydrogen crossover rate.

4. Vilekar and Datta (2010) provide a simple model that predicts the effect of fuel permeation on open-circuit voltage in PEM fuel cells. They conclude that the electrical short-circuit current is an order of magnitude smaller than the hydrogen permeation current. Thus, their result show that hydrogen crossover accounts for the observed loss of about 0.2V under open-circuit conditions.

At the present, the mechanism of loss at OCV accepted by many researcher is the internal current crossover because an amount of hydrogen crossover can be determined by the electrochemical-based method (cyclic voltammetry) and the electrical short circuit can be determined by electrical method. The method of mixed potential is still lack of studying results, this mechanism has not receive enough attention yet.

B. Activation losses

The activation losses at operating temperature of 80°C, 70°C, and 60°C are shown in **Figure 45**. The activation losses rise erectly in low current density region (20 mA/cm^2). The increasing rate is less valuable when the activation overpotential reach over 0.2 V. The activation losses at current density lower than 200 mA/cm^2 are not much different. The fuel cell with operating temperature of 80°C has the highest activation loss and at 60°C has the lowest activation loss. Thus, the increasing of operating temperature affects to the increasing of activation loss. This effect is clear up on high current density region.
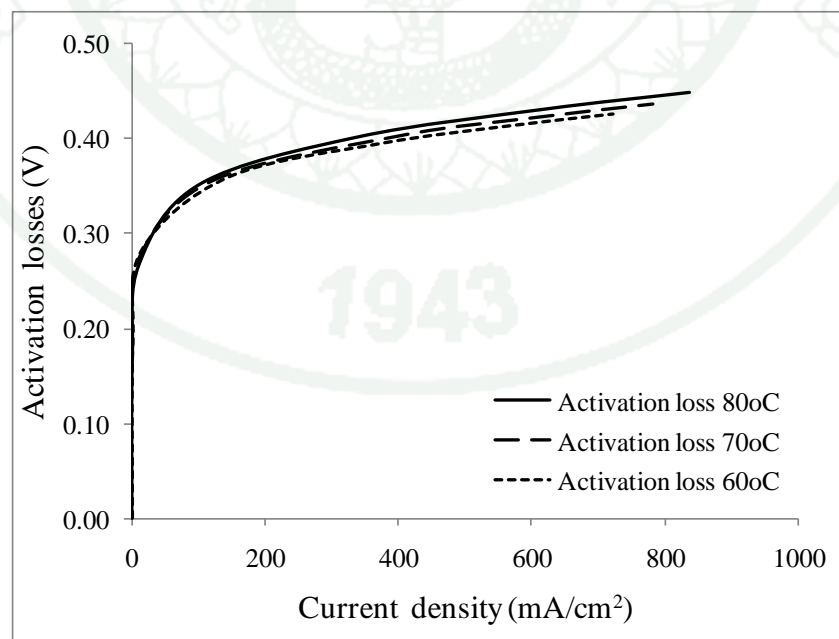
Figure 45 Simulation of activation losses at various operating temperatures.

C. Ohmic losses

The ohmic losses at difference operating temperatures are plotted with current density in **Figure 46**. The ohmic losses increase with decreasing of temperature. The decreasing of temperature causes the membrane drying due to lower humidity of the fuel (see **Figure 47**). The proton conductivity of membrane decreases with the temperature. At low current density, ~0-300 mA/cm^2, the ohmic loss increases linearly with current density. When the current density is more than 300 mA/cm^2, the slope of ohmic losses are slightly increase. The high current density causes drying of membrane surface in contact with anode, as shown in **Figure 33**. The effect of membrane drying is more pronounced at high current density.
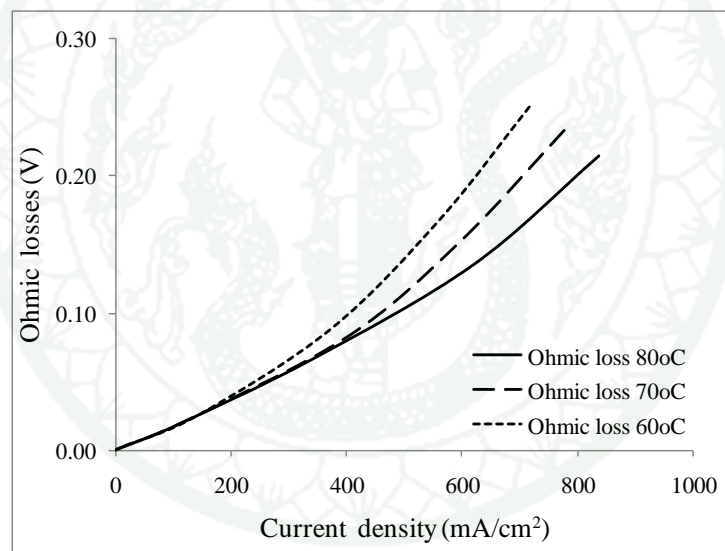
Figure 46 The ohmic losses at difference operating temperatures.
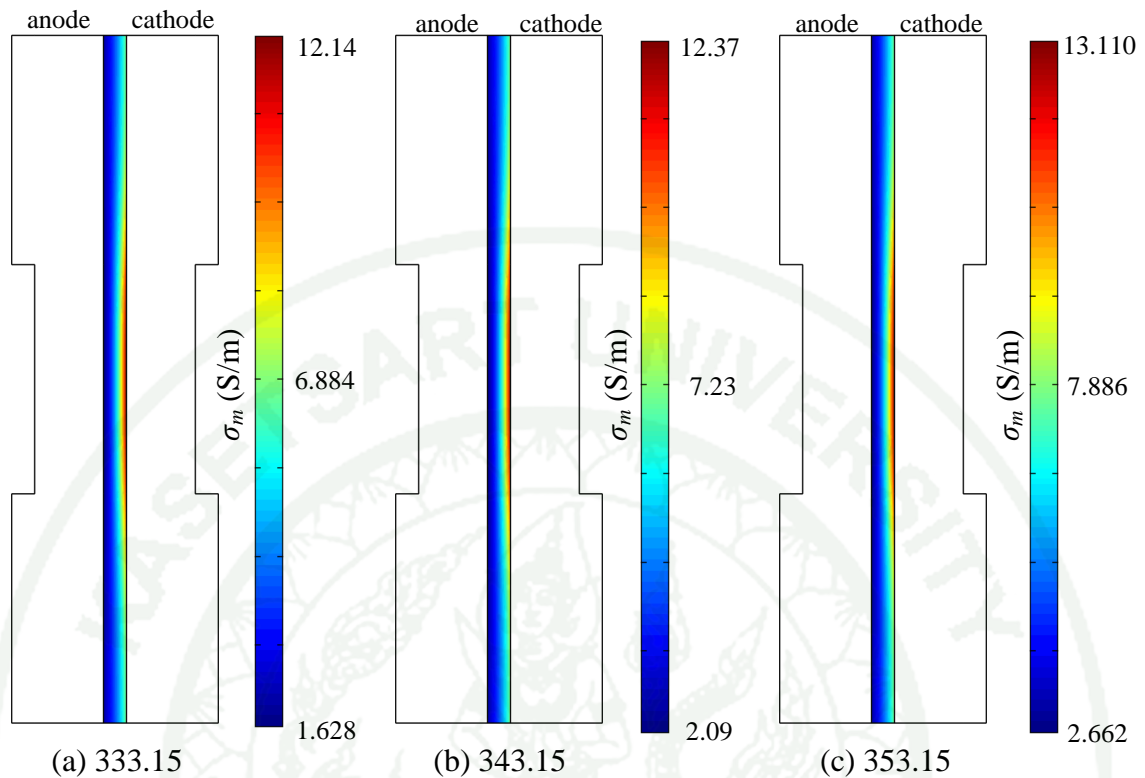
Figure 47 The proton conductivity of Nafion® membrane at various operating
temperature; (a) 333.15 K, (b) 343.15 K, (c) 353.15 K. Note that the
operating voltage is 0.5 V.

3. PEMFC performance at various operating pressure.

The polarization curves of simulation and experimental results at various
operating pressure are shown in the **Figure 48** and the power density curves are
shown in **Figure 49**. The experimental results are obtained from M. Amirinejad
(2006) for a fuel cell with active area of 5 cm^2 with the same properties and
conditions. The fuel cell is operated at 70°C. The hydrogen and oxygen are used as
fuels at anode and cathode sides. The reactants are fed with 100% relative humidity at
70°C to both anode and cathode. The operating pressure is varied from 1 atm to 3 atm.
The simulation results do not fit with the experimental result because of the lack of
some parameters from Amirinejad's experiment, the exchange current density (i_0) and
the charge transfer coefficient (α). Therefore the simulation uses the parameters from

KUCHE lab's experiment instead. The parameters are obtained at 1 atm pressure and are the function of temperature only.

The best performance is observed when the operating pressure is 3 atm and the lowest performance is observed when the operating pressure is 1 atm. Therefore the performance of fuel cell increases with the operating pressure. The simulation results give the same trend as the experimental results but are higher because the simulation does not cover all the parameters affecting the fuel cell performance such as electrical resistances of various fuel cell components and inter layer resistance.
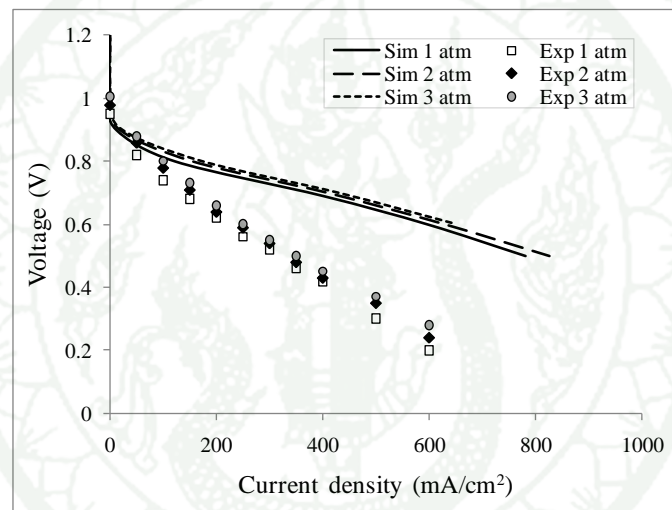
Figure 48 The polarization curve of simulation and experimental results. The
operating pressure are as follow: 1 atm, 2 atm, and 3 atm at operating
temperature of 70°C. Note that the humidified gas temperature is the same
as operating temperature. The experimental result is obtained from M.
Amirinejad (2006).
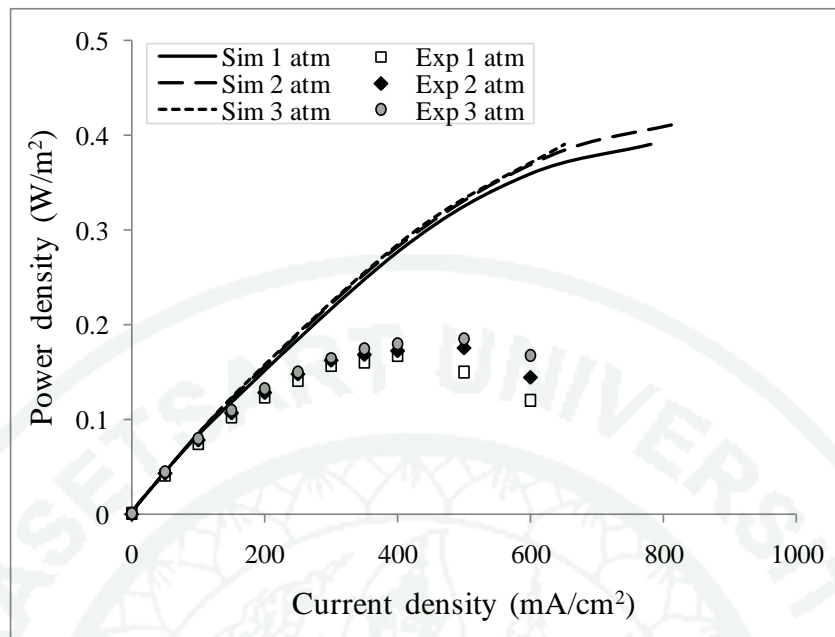
Figure 49 The power density of simulation and experimental results. The operating
pressures are 1 atm, 2 atm, and 3 atm at operating temperature of 70°C.
Note that the humidified temperature is the same as operating
temperature. The experimental result is obtained from M. Amirinejad
(2006).

A. Open Circuit Voltage (OCV)

The open circuit voltages from simulation and experiment at various
operating pressure are shown in **Figure 50**. The theoretical open circuit voltages are
higher than actual operating open circuit voltages. The results from simulation and
experiment are in the same trend, the open circuit voltage increase with operating
pressure. The increasing of reactant partial pressure causes the increasing of open
circuit voltage, thus the performance of fuel cell increase. Increasing the operating
pressure give the same effect as increasing the operating temperature, as shown in
Figure 42. The reason that the loss at open circuit voltage occur is the same as
discussed before.
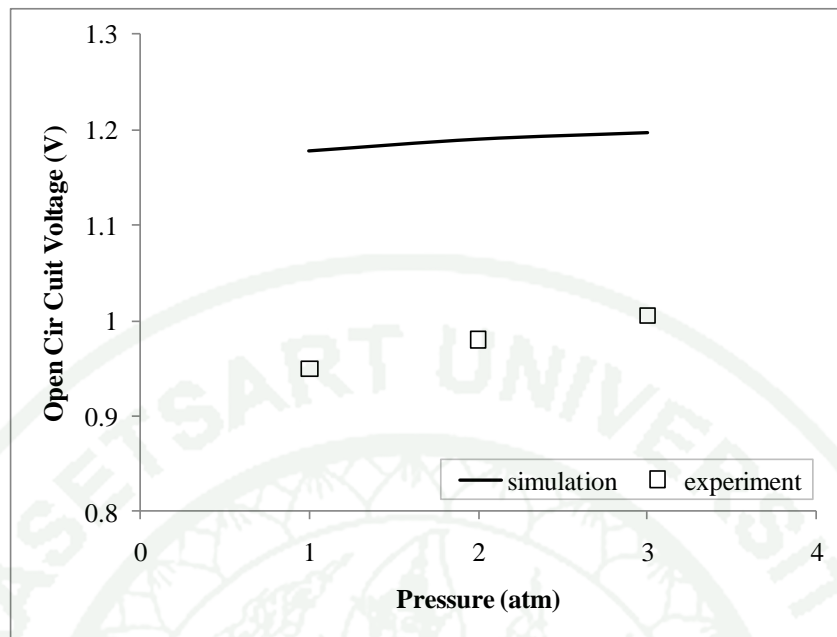
Figure 50 Experimental results and simulation results of open circuit voltages at various operating pressure. The experimental result is obtained from M. Amirinejad (2006).

B. Activation losses

The activation losses at operating pressure of 1 atm, 2 atm, and 3 atm are shown in **Figure 51**. The activation losses are nearly the same value for all operating pressure. Thus the increasing of pressure does not have significant effects on the activation losses. These results come from the limitation of the simulation that reactant concentration is not included into the Butler-Volmer equations, thus the effect of pressure on activation loss does not realize in this work.

C. Ohmic losses

The ohmic losses at difference operating back pressure are plotted with current density in **Figure 52**. The ohmic losses slightly decrease with increasing of operating back pressure. However, it does not have effect much.
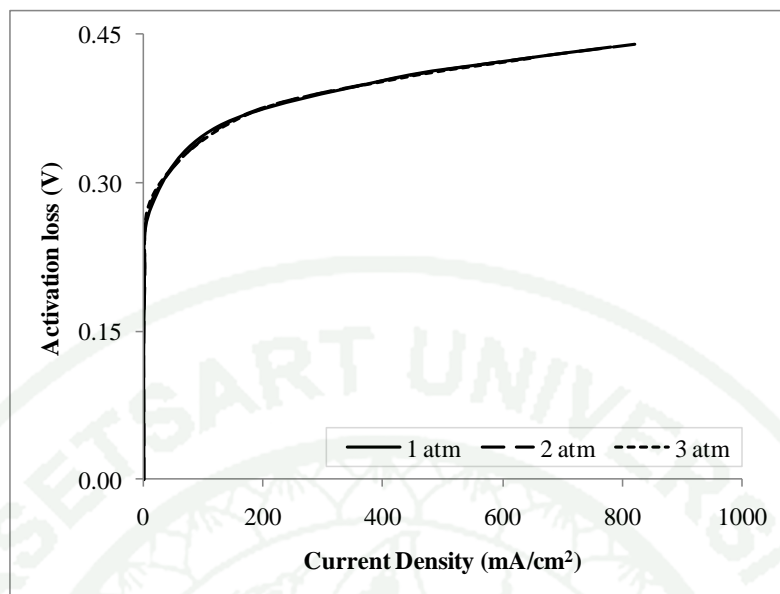
Figure 51 Simulation result of the activation losses at various operating pressures.
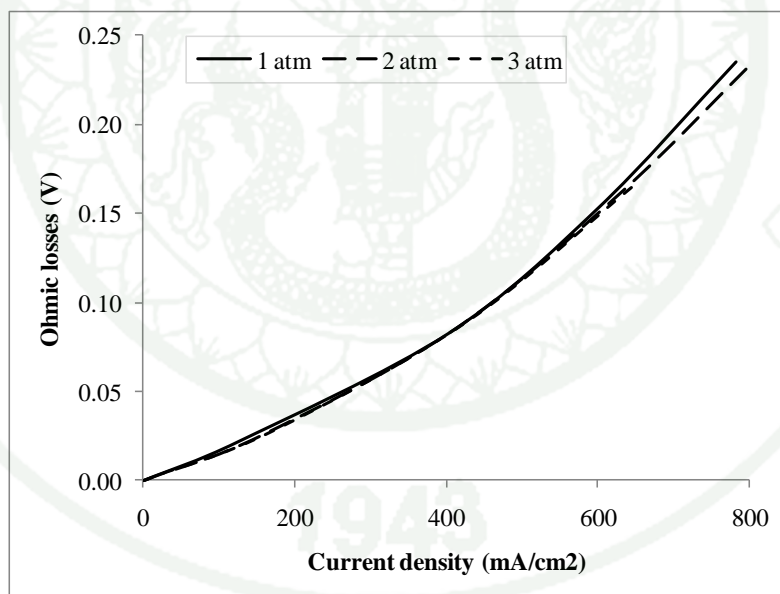
Figure 52 Simulation result of the ohmic losses at difference operating pressure.

CONCLUSIONS

The simulation results represent the hydrodynamic behavior in the proton exchange membrane fuel cell. At the region behind the channel rib, the high fluid velocity is observed and resulted in the high convective mass transfer in this zone. The velocity profiles show that there is low fluid velocity at entrance and exit regions. Thus the convective mass transfer capability is low.

The high temperature zones appear at the reaction surfaces and the gas diffusion layers behind the flow channels which affect to a decreasing of averaged water content at nearby membrane especially when fuel cell operated at high current density. The temperature at cathode side is higher than that at anode side due to higher activation losses.

The gas composition distributions show that the occurrence of water flooding in GDL is difference for anode and cathode. At the anode, the high water concentration is observed near the entrance of the GDL. For low current density, high water concentration al so appears near the anode bottom edge. At the cathode, the high water concentration is observed in the GDL near the reaction surface and near the bottom edge.

The current density distribution shows that the electrochemical reaction rate, which corresponds to current density, in membrane at region behind the channel rib is higher than that at the upper and lower regions opposite the flow channels because of the high proton conductivity of the membrane.

The OCV increases with operating pressure but inversely with temperature. The activation loss increases with operating temperature but the ohmic losses increases inversely with operating temperature. In this simulation, the operating pressure does not have much effect to the activation and ohmic losses. The combination of each polarization results in polarization curve. Both operating temperature and pressure can improve the performance of PEMFC.

LITERATURE CITED

Amirinejad, M., S. Rowshanzamir and M. H. Eikani. 2006. Effects of operating parameters on performance of a proton exchange membrane fuel cell. **J. Power Source**. 161: 872-875.

Baschuk, J.J. and X. Li. 2009. A comprehensive, consistent and systematic mathematical model of PEM fuel cells. **Applied Energy**. 86: 181-193.

Bernardi, D.M. and M.W. Vebrunge. 1992. A mathematical model of the solidpolymer- electrolyte fuel cell. **J. Electrochem. Soc.** 139(9): 2477–2491.

Berning, T. and N. Djilali, 2003. Three-dimensional computational analysis of transport phenomena in a PEM fuel cell-a parametric study. **J. Power Sources**. 124: 440–452.

Bird, R.B., W.E. Stewart and E.N. Lightfoot. 2005. **Transport Phenomena**. 2nd ed. John   Wiley & Sons.

Choy, C.L., Y.W. Wong, G.W. Yang, T. Kanamoto, **J. Polym. Sci.: Polym. Phys. Ed.** 37: 3359–3367.

Curtiss C.F. and R.B. Bird. 1999. **Ind. Eng. Chem. Res.** 38: 2515.

Gostick, J.T., M.W. Fowler, M. D. Pritzker, M. A. Ioannidis and L. M. Behra. 2006. In-plane and through-plane gas permeability of carbon fiber electrode backing layers. J. Power Source. 162: 228-238.

Guvelioglu, G. H. and H. G. Stenger. 2005. Computational fluid dynamics modeling of polymer electrolyte membrane fuel cells. **J. Power source**. 147: 95-106.

Guvelioglu, G. H. and H. G. Stenger. 2007. Flow rate and humidification
        effects on a   PEM fuel cell performance and operation. **J. Power
        source**. 163: 882-831.

Hoogers, G. 2003. **Fuel Cell Technology Handbook.** CRC Press, Florida.

Hwang, J.J., P.Y. Chen. 2006. Heat/mass transfer in porous electrodes of fuel cells.
        Int. J. Heat Mass Tran. 49: 2315-2327.

Khandelwal, M. and M.M. Mench. 2006. Direct measurement of through-plane
        thermal conductivity and contact resistance in fuel cell materials. **J. Power
        Source.** 161:   1106-   1115.

Kim, G.S., P.C. Sui, A.A. Shah and N. Djilali. 2010. Reduced-dimensional models for
        straight-channel proton exchange membrane fuel cells. **J. Power Source**. 195:
        3240-3249.

Kovetz, A. 1990. **The Principles of Electromagnetic Theory.** Cambridge University
        Press.

Larminie, J. and Dicks, A. 2004. **Fuel Cell System Explained.** 2nd ed. Wiley, West
        Sussex.

Leelasupakorn, H.. 2008. **The activation losses in a proton exchange membrane
        fuel cell**. Thesis, Kasetsart University.

Nguyen, P.T., T. Berning and N. Djilali. 2004. Computational model of PEM fuel cell
        with serpentine gas flow channels. **J. Power Source**. 130: 149-157.

O'Hayre, R. P. 2009. **Fuel Cell Fundamentals.** Wiley, USA.

Parthasarathy, A., S. Srinivasan, J.A. Appleby and C.R. Martin. 1992. Temperature dependence of the electrode kinetics of oxygen reduction at the platinum/Nafion interface: a microelectrode investigation. **J. Electrochem. Soc.** 139(9): 2530–2537.

Perry, R.H. and D.W. Green. **Perry's Chemical Engineer's Handbook**. 7th ed., McGraw-Hill, 1997.

Reid, R.C., J.M. Prausnitz and B.E. Poling. 1987. **The Properties of gases and Liquids**. 4th ed. **McGraw-Hill**. Boston.

Rowe, A. and X. Li. 2001. Mathematical modeling of proton exchange membrane fuel cells. J. Power Source. 102: 82-96.

Springer, T.E., T.A. Zawodzinski and S. Gottesfeld. 1991. Polymer Electrolyte Fuel Cell Model. **J. Electrochem. Soc.** 138(8): 2334-2342.

Vayenas, C.G., M.N. Tsampas and A. Katsaounis. 2007. First principles analytical prediction of the conductivity of Nafion membranes. **Electrochemica Acta.** 52: 2244-2256.

Zawodzinski, T.A., M. Neeman, L.O. Sillerud and S. Gottesfeld. 1991. Determination of water Dlffusion Coeff icients in Perfluorosulfonate Ionomeric Membranes. **J. Phy. Chem.** 95: 6040-6044.

APPENDICES
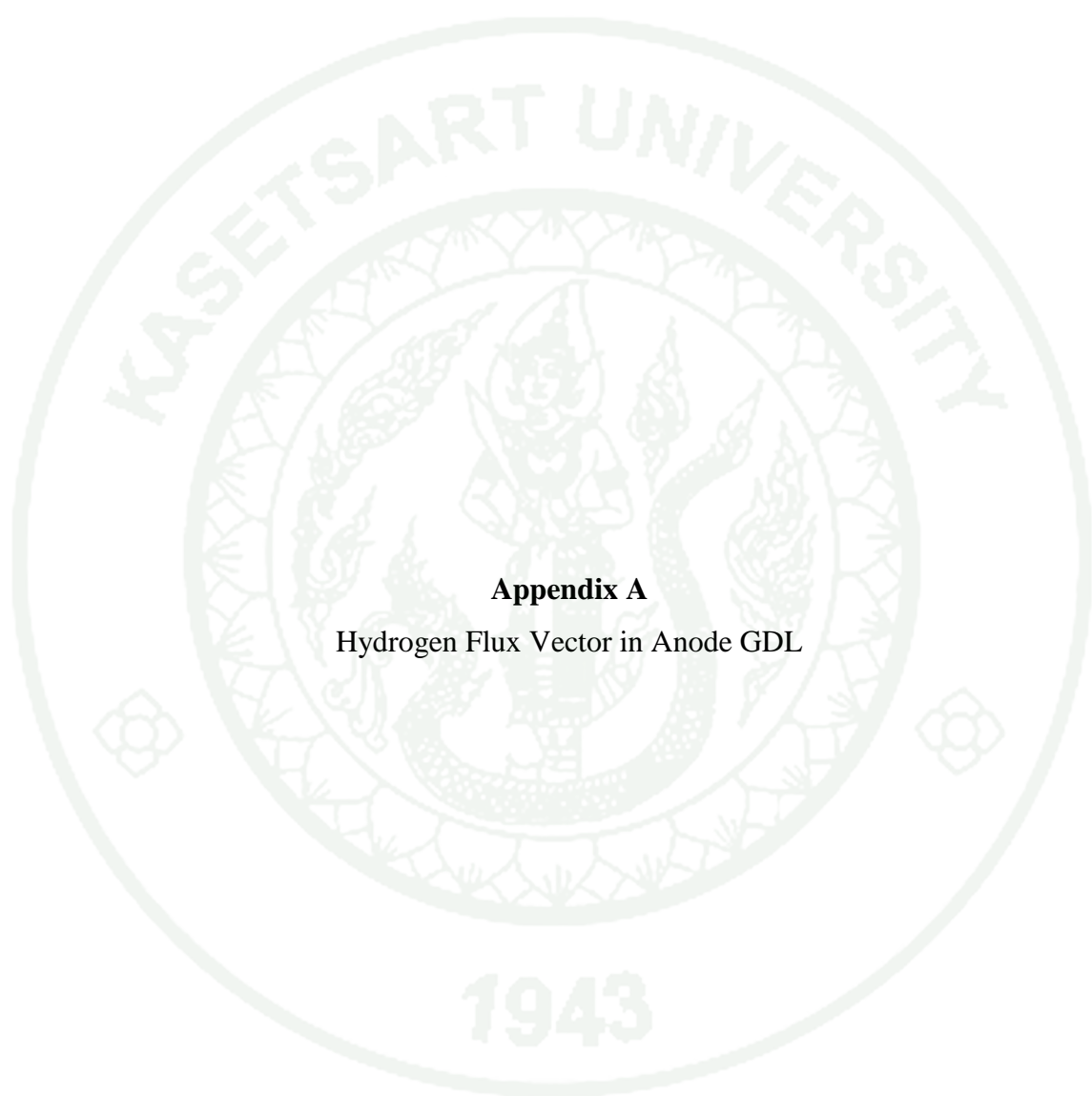
Appendix A

Hydrogen Flux Vector in Anode GDL
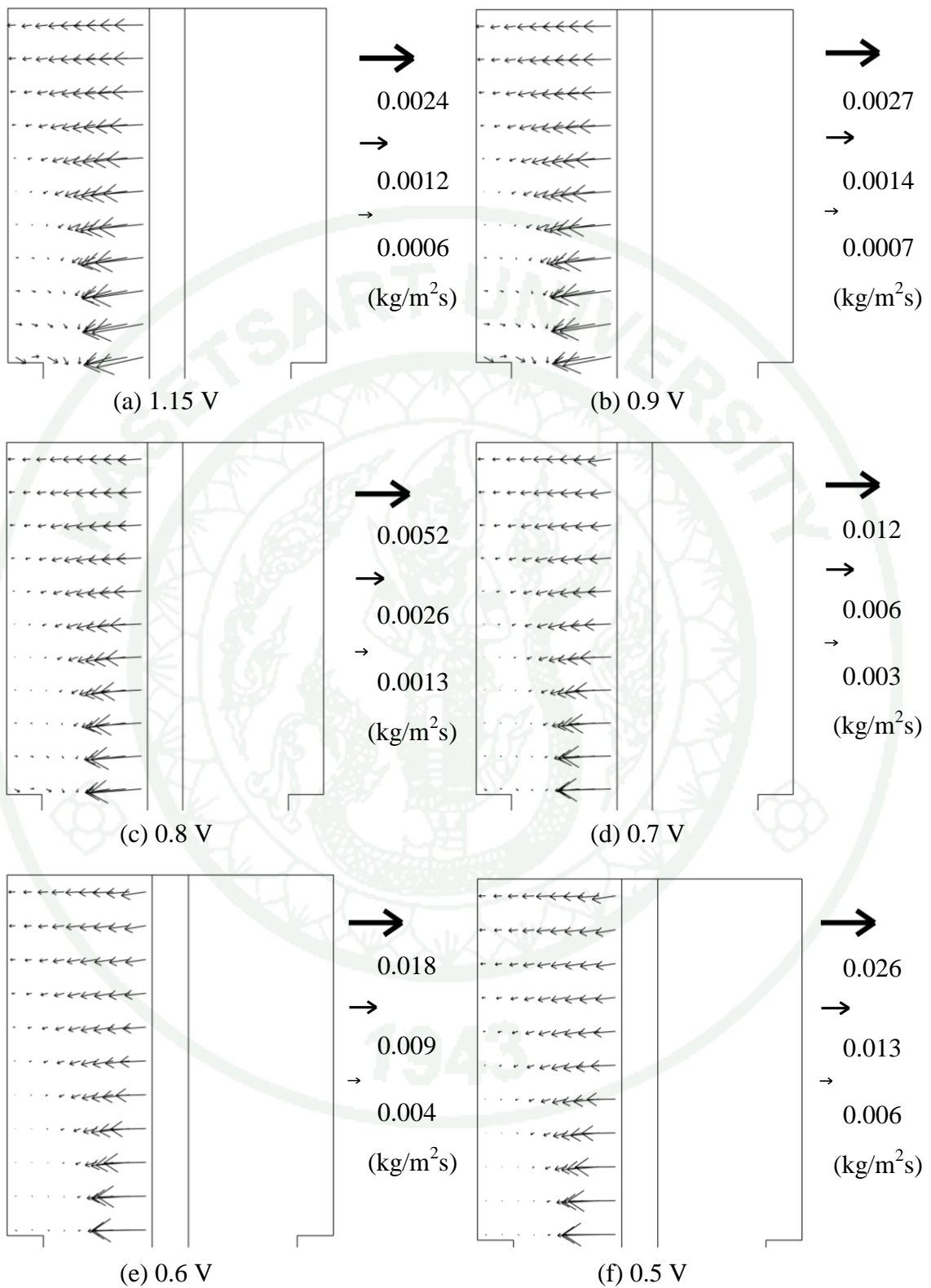
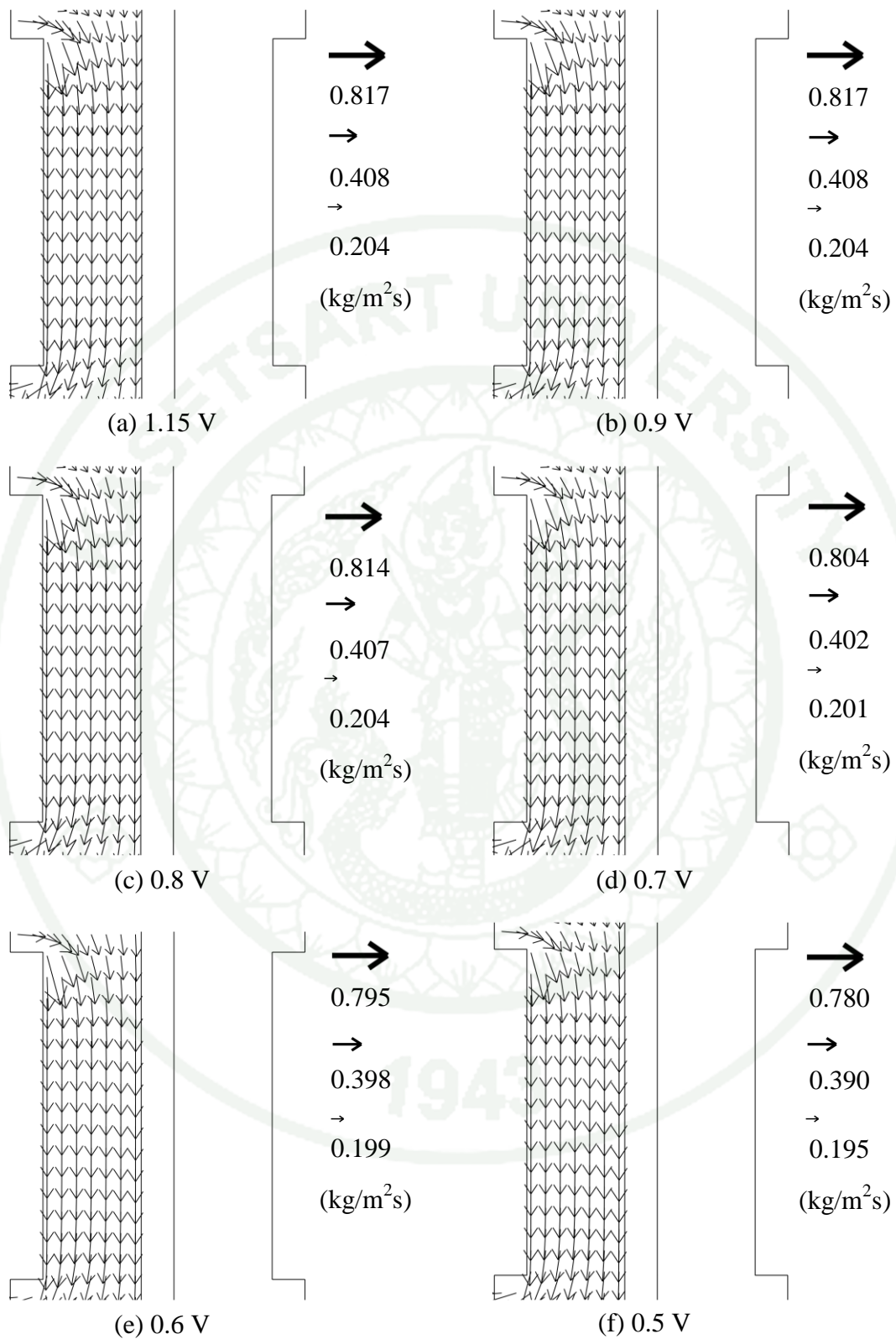**Appendix Figure A1** The diffusive flux of hydrogen in the entrance region at various operating voltages.

(a) 1.15 V

0.0022
0.0011
0.0005
(kg/m^{2}s)

(b) 0.9 V

0.0025
0.0012
0.0006
(kg/m^{2}s)

(c) 0.8 V

0.0052
0.0026
0.0013
(kg/m^{2}s)

(d) 0.7 V

0.0118
0.0059
0.0030
(kg/m^{2}s)

(e) 0.6 V

0.0176
0.0088
0.0044
(kg/m^{2}s)

(f) 0.5 V

0.0284
0.0142
0.0071
(kg/m^{2}s)
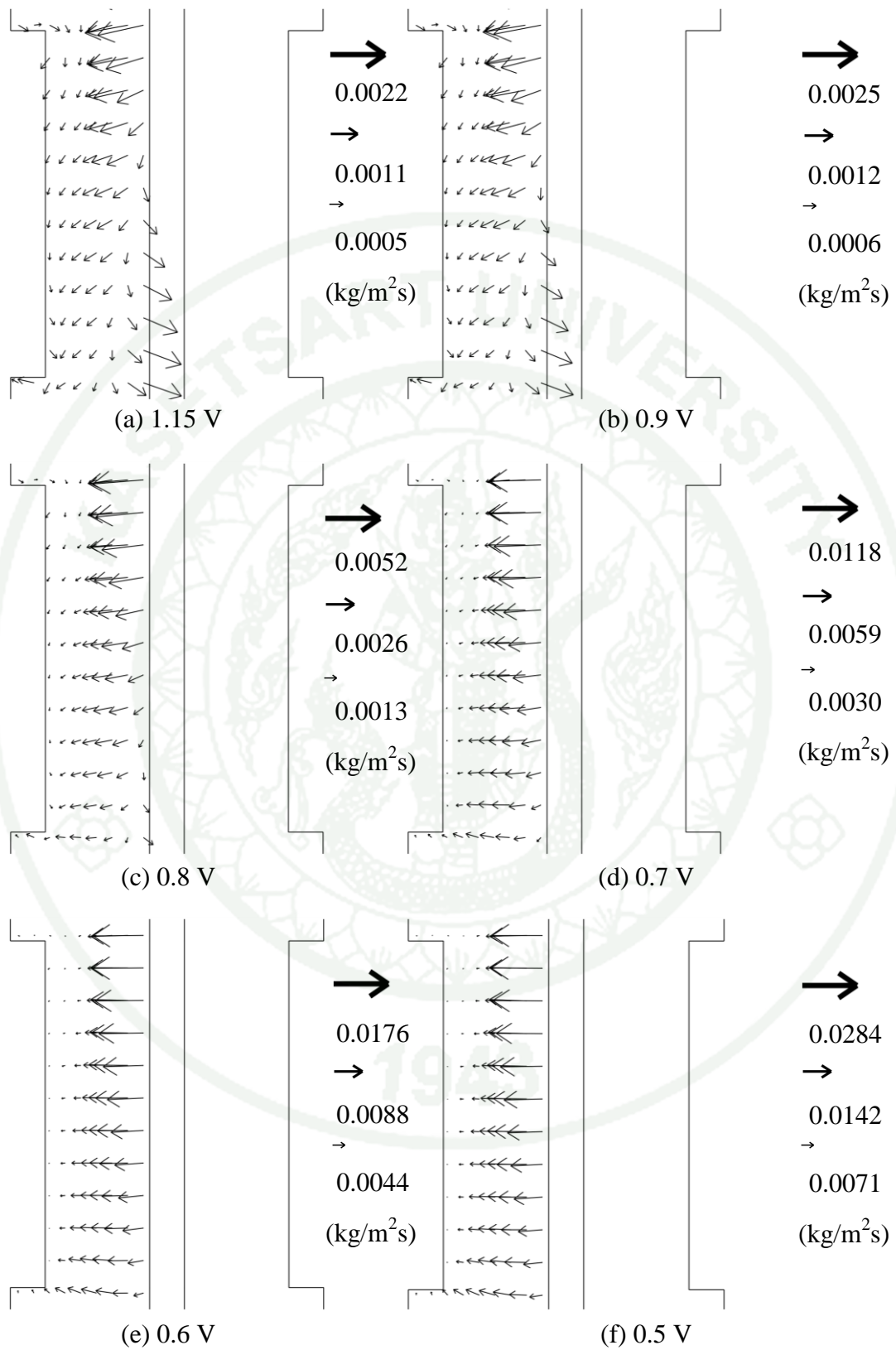
Appendix Figure A2 The diffusion flux of hydrogen in the GDL behind the channel
rib at various operating voltages.

(a) 1.15 V

0.0020

0.0010

0.0005

(kg/m²s)

(b) 0.9 V

0.0019

0.0010

0.0005

(kg/m²s)

(c) 0.8 V

0.0017

0.00087

0.00044

(kg/m²s)

(d) 0.7 V

0.0034

0.0017

0.0008

(kg/m²s)

(e) 0.6 V

0.0056

0.0028

0.0014

(kg/m²s)

(f) 0.5 V

0.0096

0.0048

0.0024

(kg/m²s)
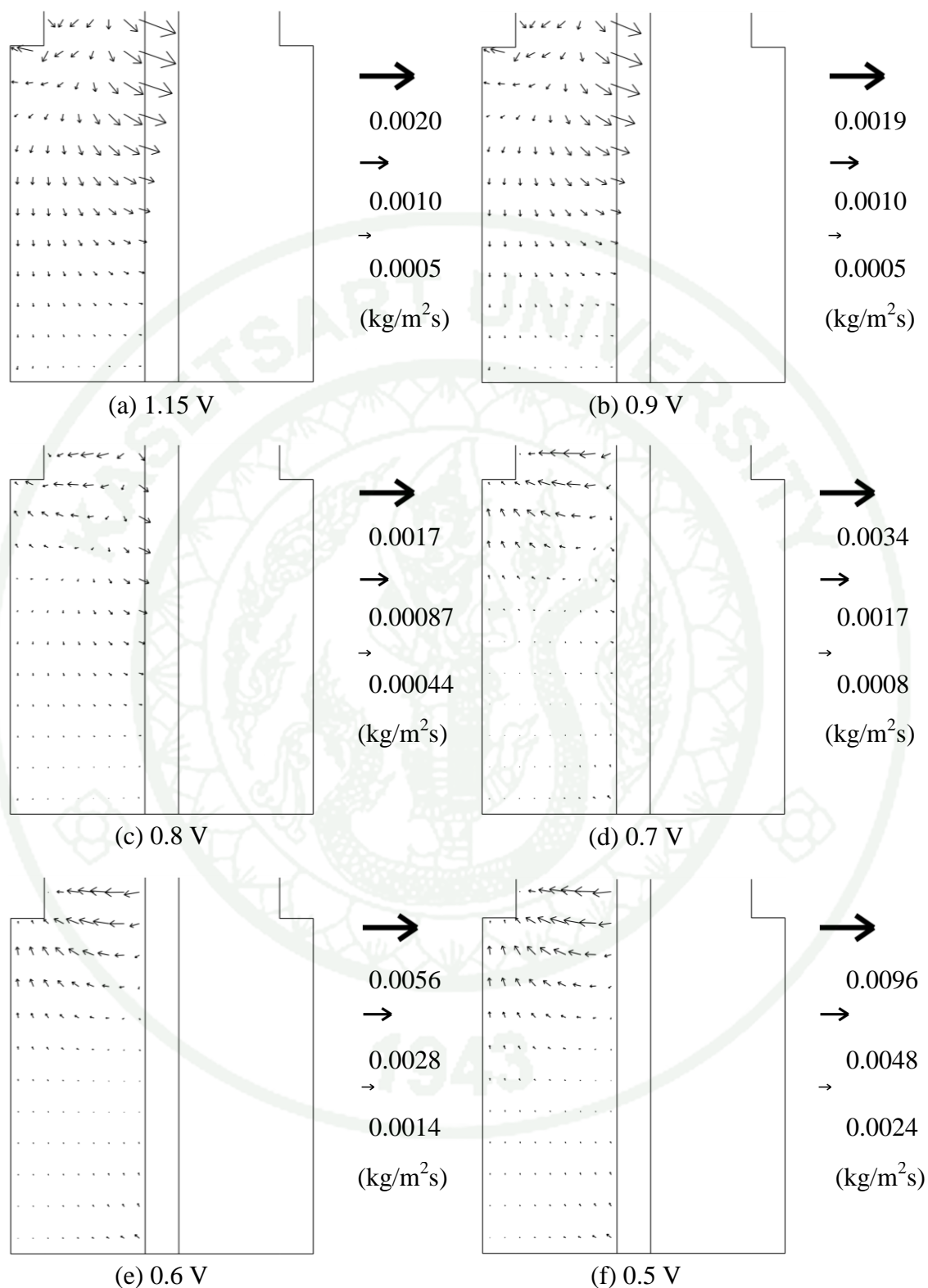
Appendix Figure A3 The diffusive flux of hydrogen in the GDL at the exit region at various operating voltages.

(a) 1.15 V

(b) 0.9 V

(c) 0.8 V

(d) 0.7 V

(e) 0.6 V

(f) 0.5 V
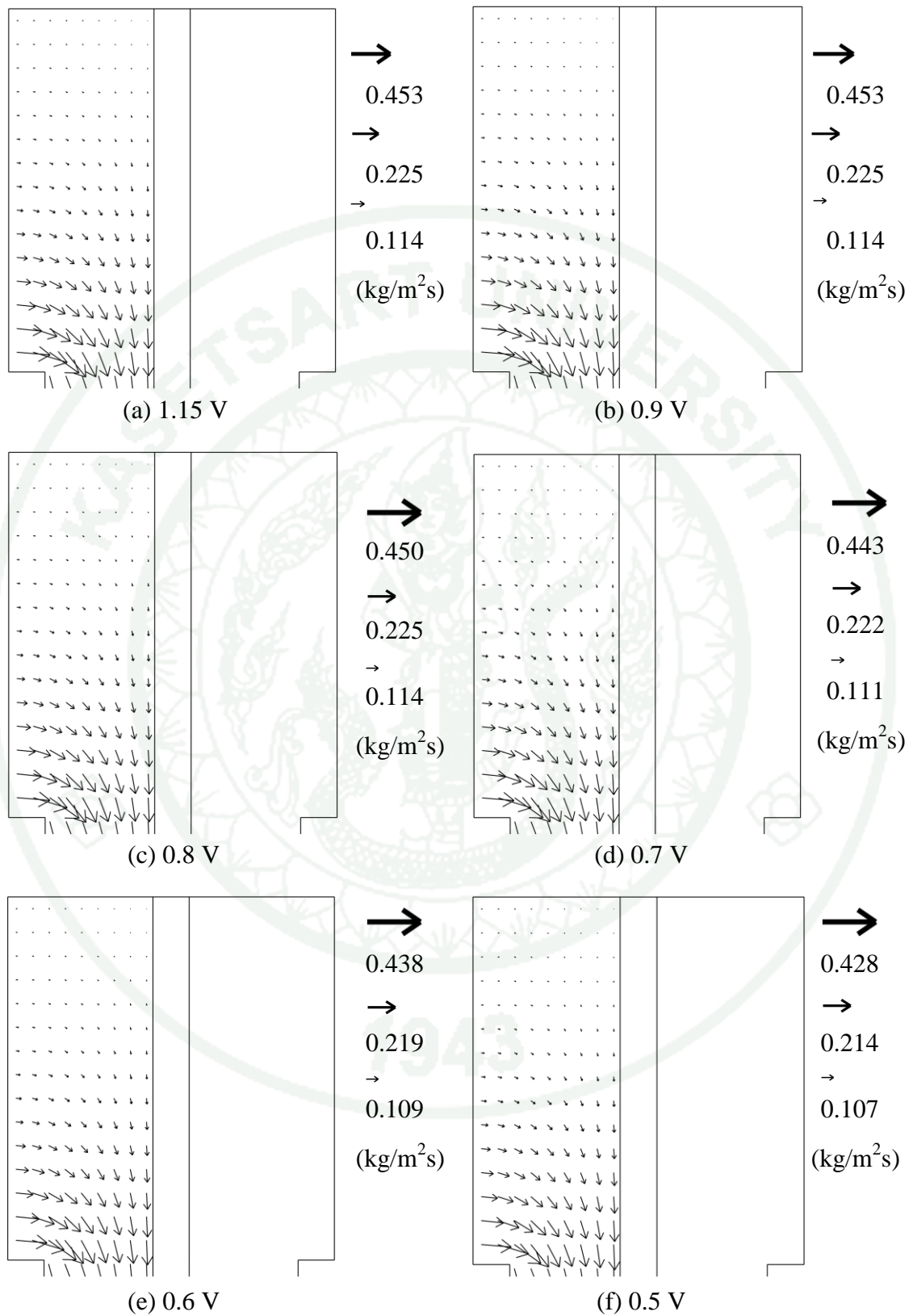
Appendix Figure A4 The convective flux of hydrogen in the entrance region at various operating voltages.

Appendix Figure A5 The convective flux of hydrogen in the GDL behind the
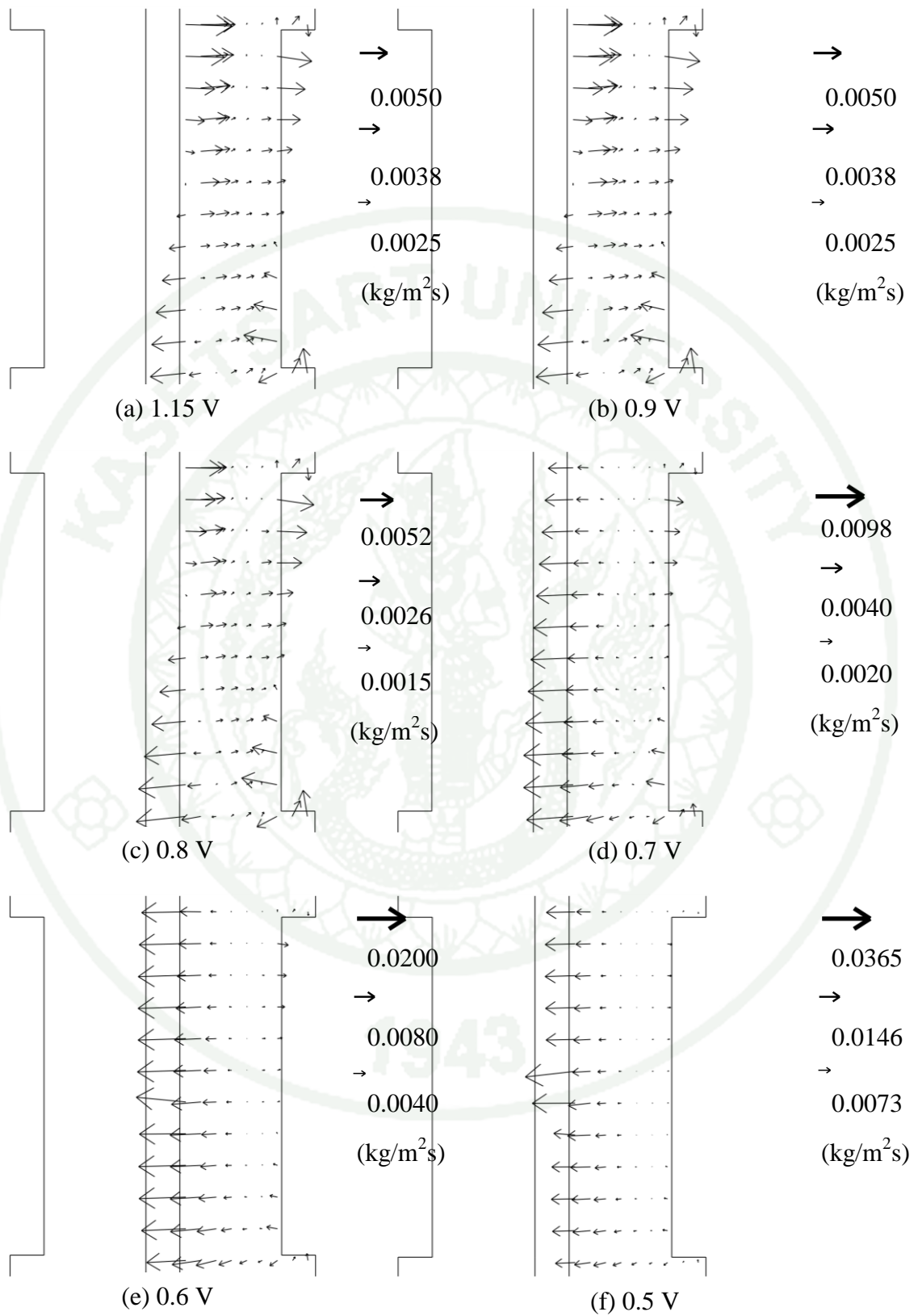channel rib at various operating voltages.
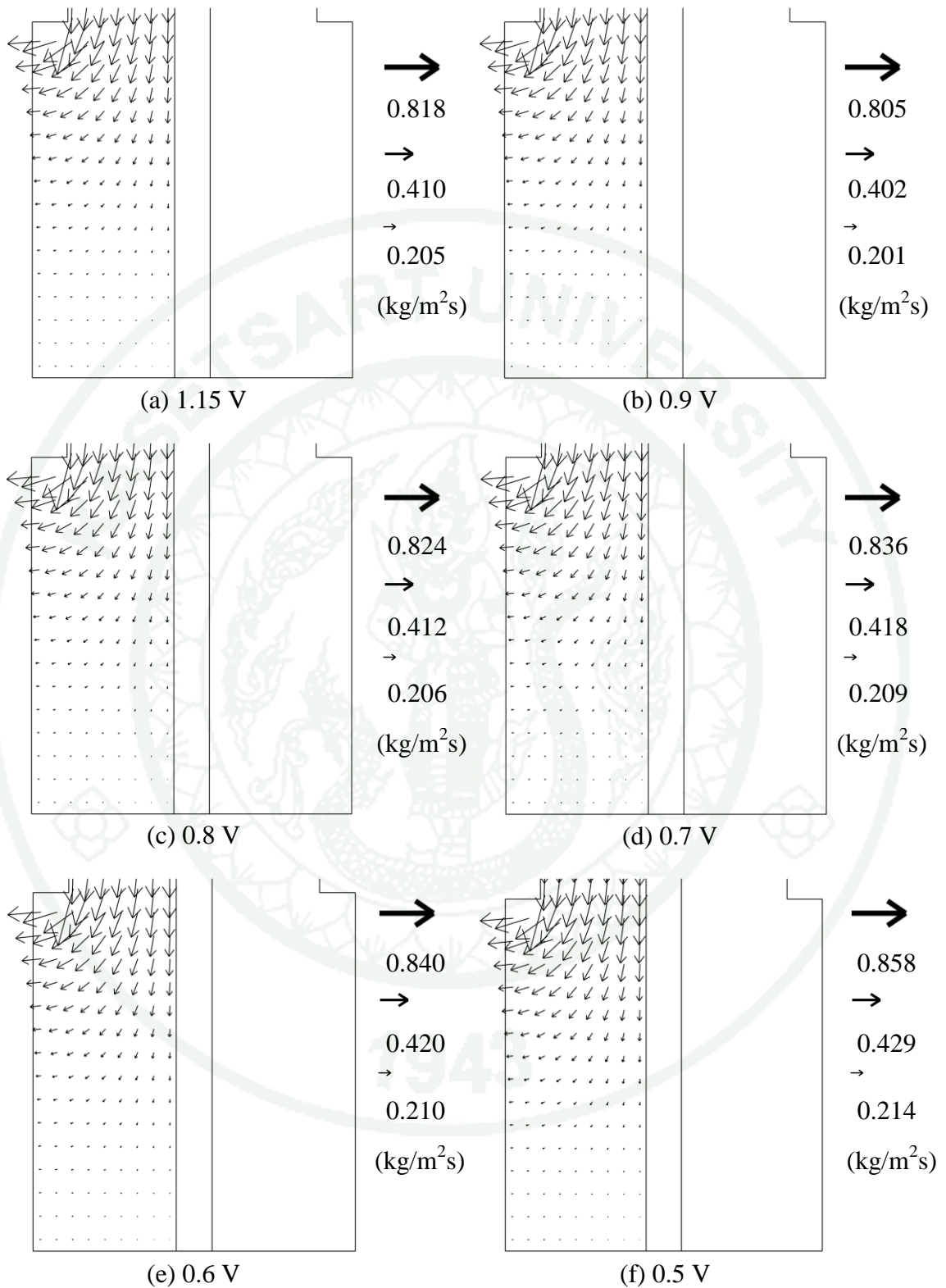
Appendix Figure A6 The convective flux of hydrogen in the GDL at the exit region
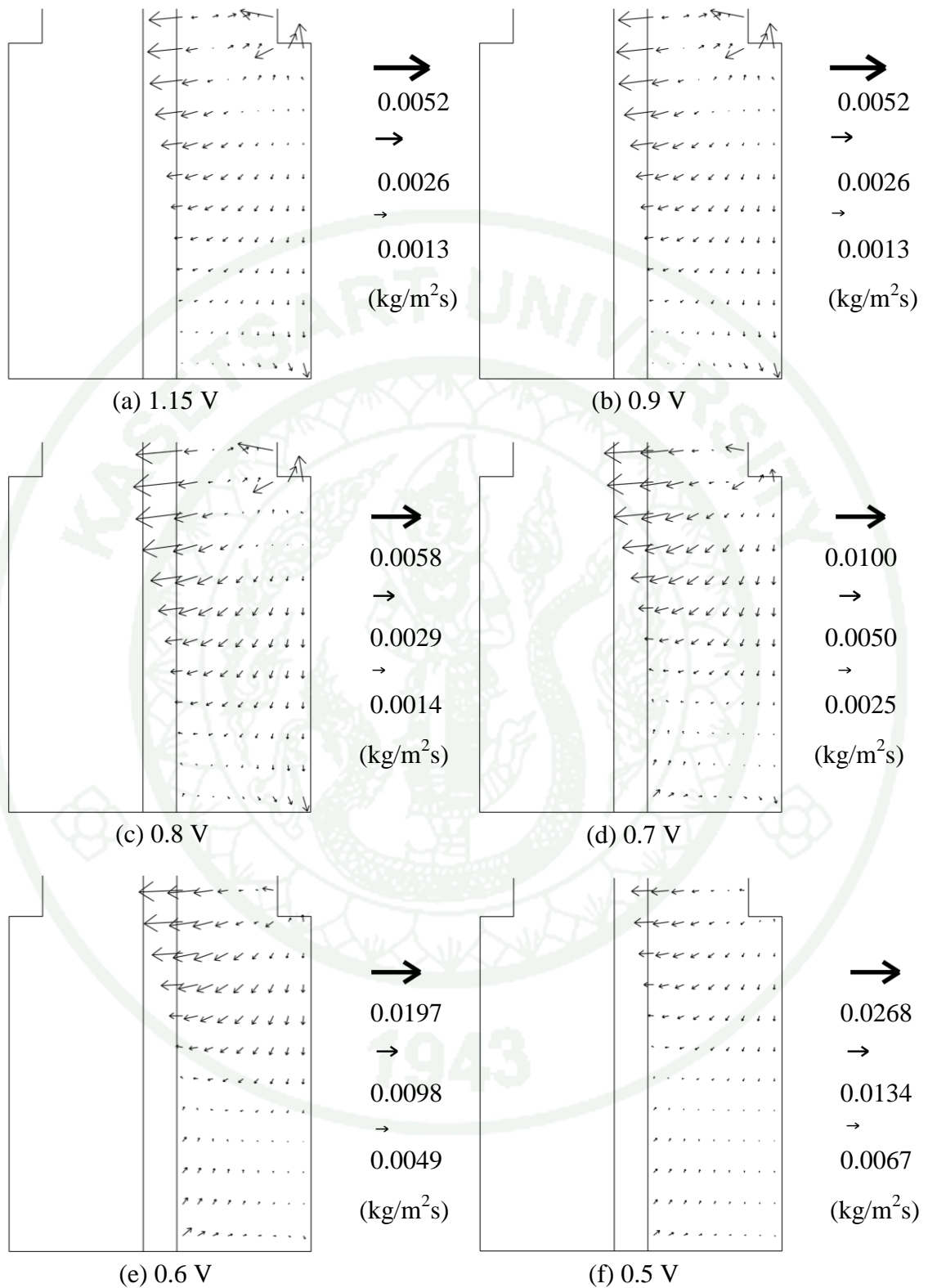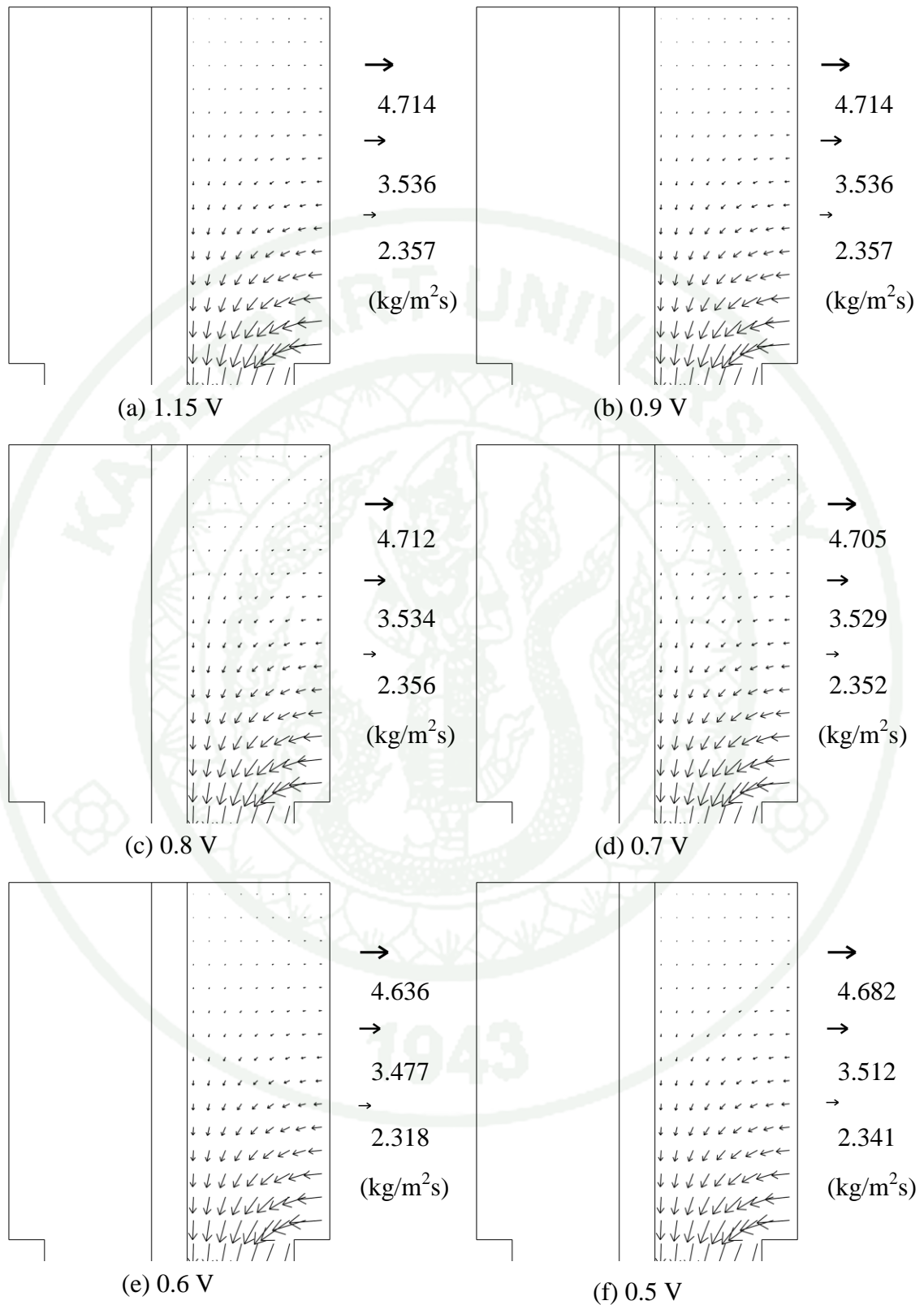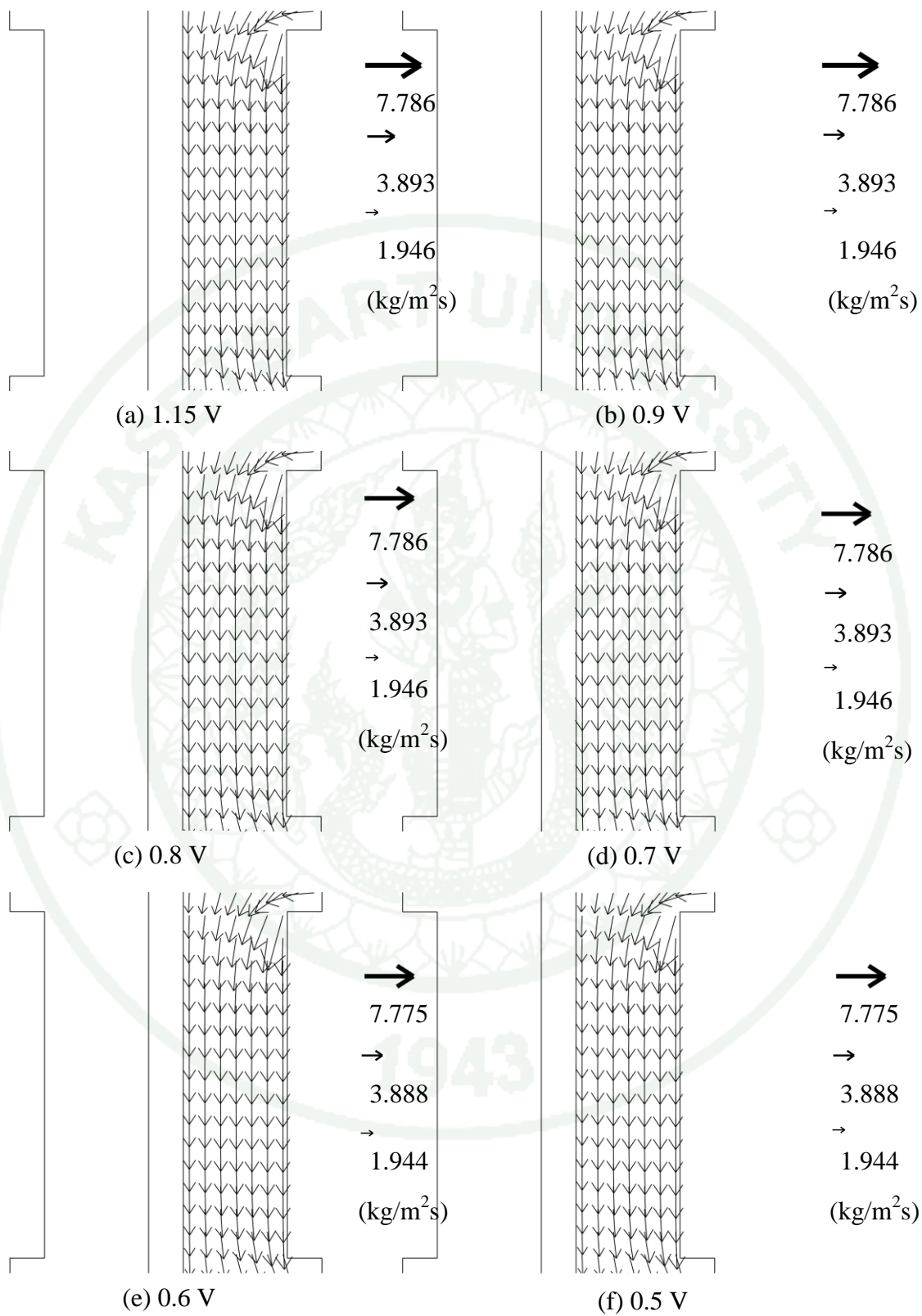
at various operating voltages.

(a) 1.15 V

(b) 0.9 V

(c) 0.8 V

(d) 0.7 V

(e) 0.6 V

(f) 0.5 V
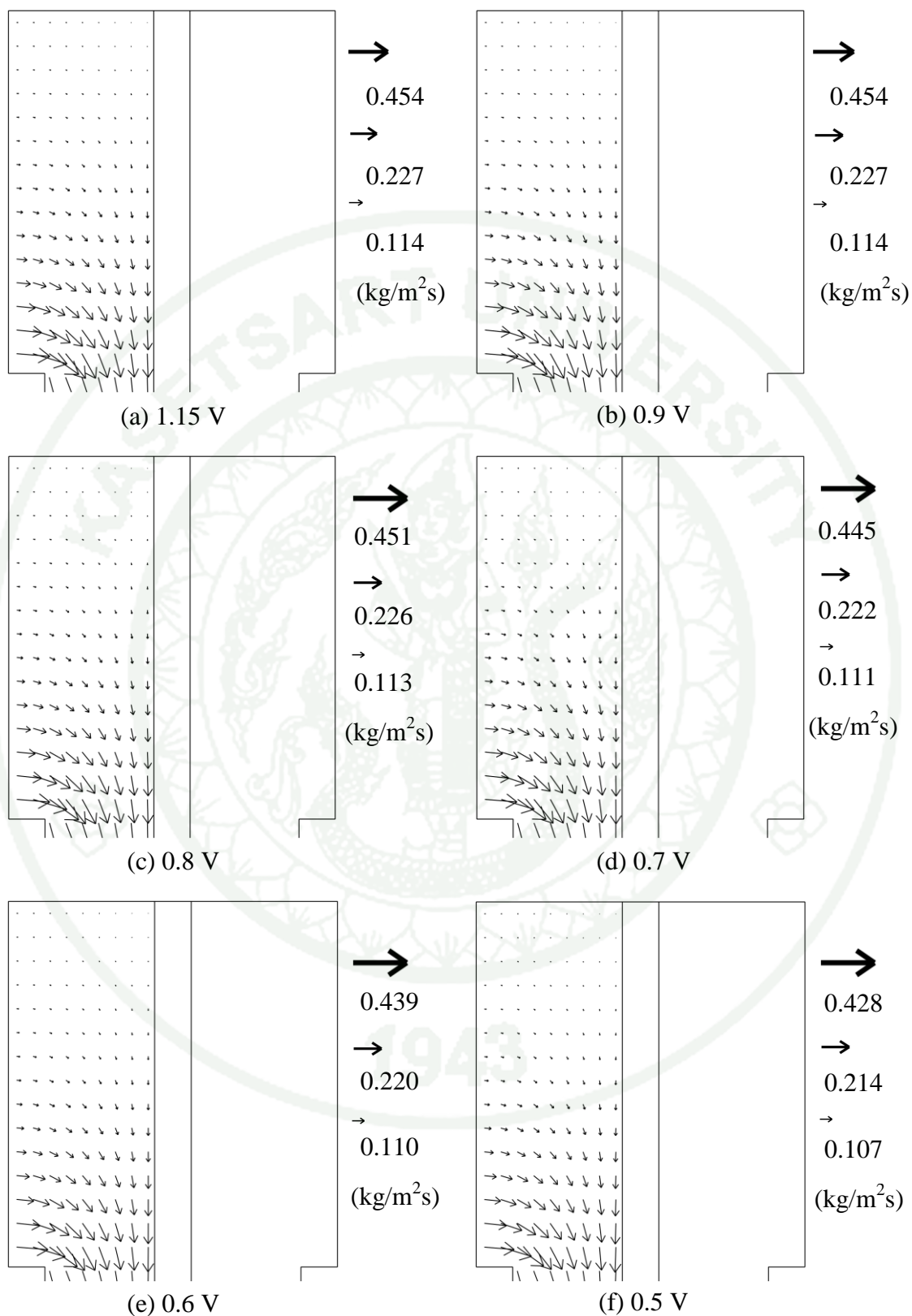
Appendix Figure A7 The total flux of hydrogen in the entrance region at various operating voltages.

(a) 1.15 V

0.817

0.408

0.204

(kg/m^{2}s)

(b) 0.9 V

0.816

0.408

0.204

(kg/m^{2}s)

(c) 0.8 V

0.812

0.406

0.203

(kg/m^{2}s)

(d) 0.7 V

0.806

0.403

0.202

(kg/m^{2}s)

(e) 0.6 V

0.790

0.395

0.198

(kg/m^{2}s)

(f) 0.5 V

0.774

0.387

0.194

(kg/m^{2}s)
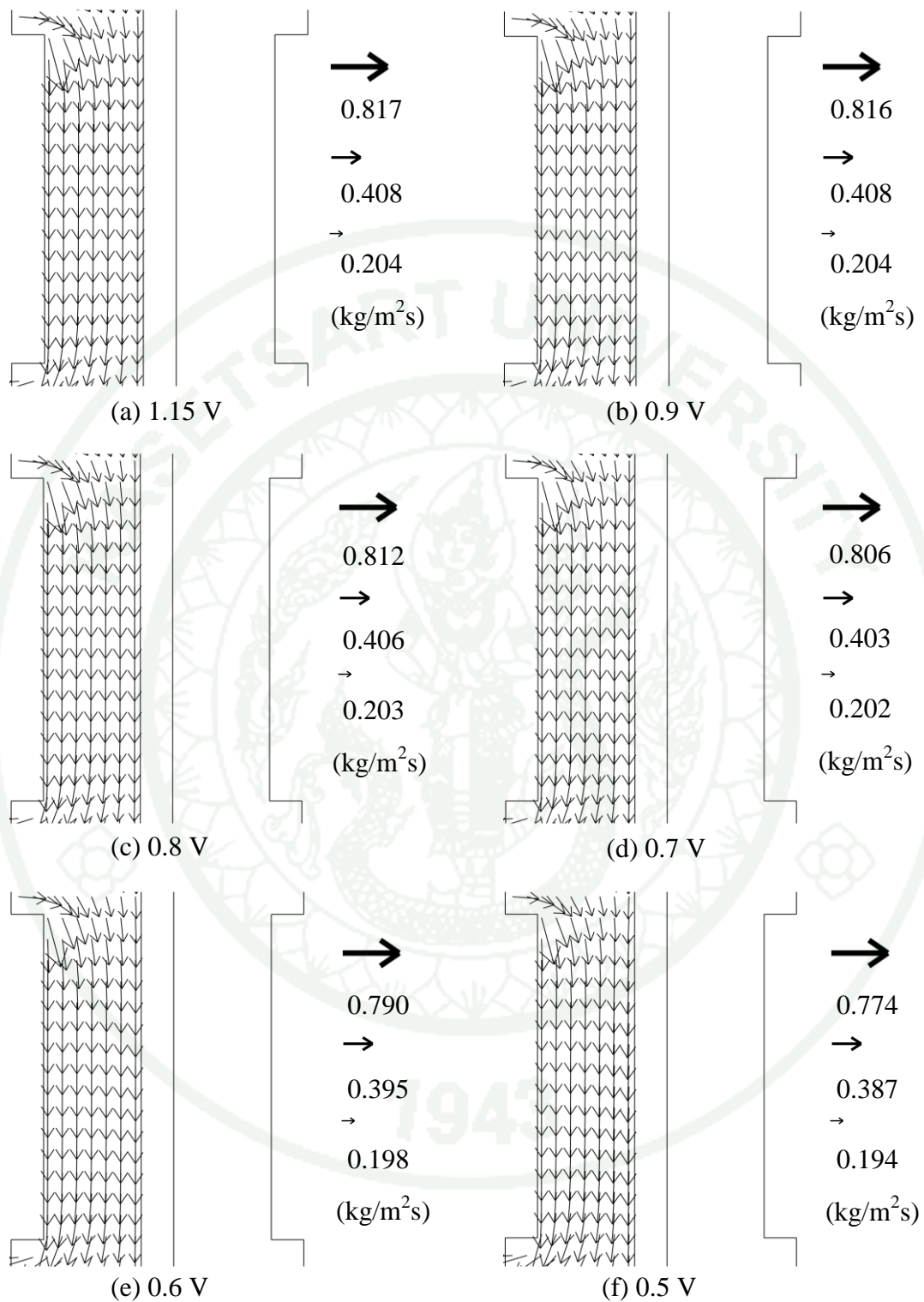
Appendix Figure A8 The total flux of hydrogen in the GDL behind the channel rib
at various operating voltages.

(a) 1.15 V

0.810

0.405

0.202

(kg/m²s)

(b) 0.9 V

0.825

0.412

0.206

(kg/m²s)

(c) 0.8 V

0.829

0.414

0.207

(kg/m²s)

(d) 0.7 V

0.828

0.414

0.207

(kg/m²s)

(e) 0.6 V

0.831

0.416

0.208

(kg/m²s)

(f) 0.5 V

0.865

0.432

0.216

(kg/m²s)
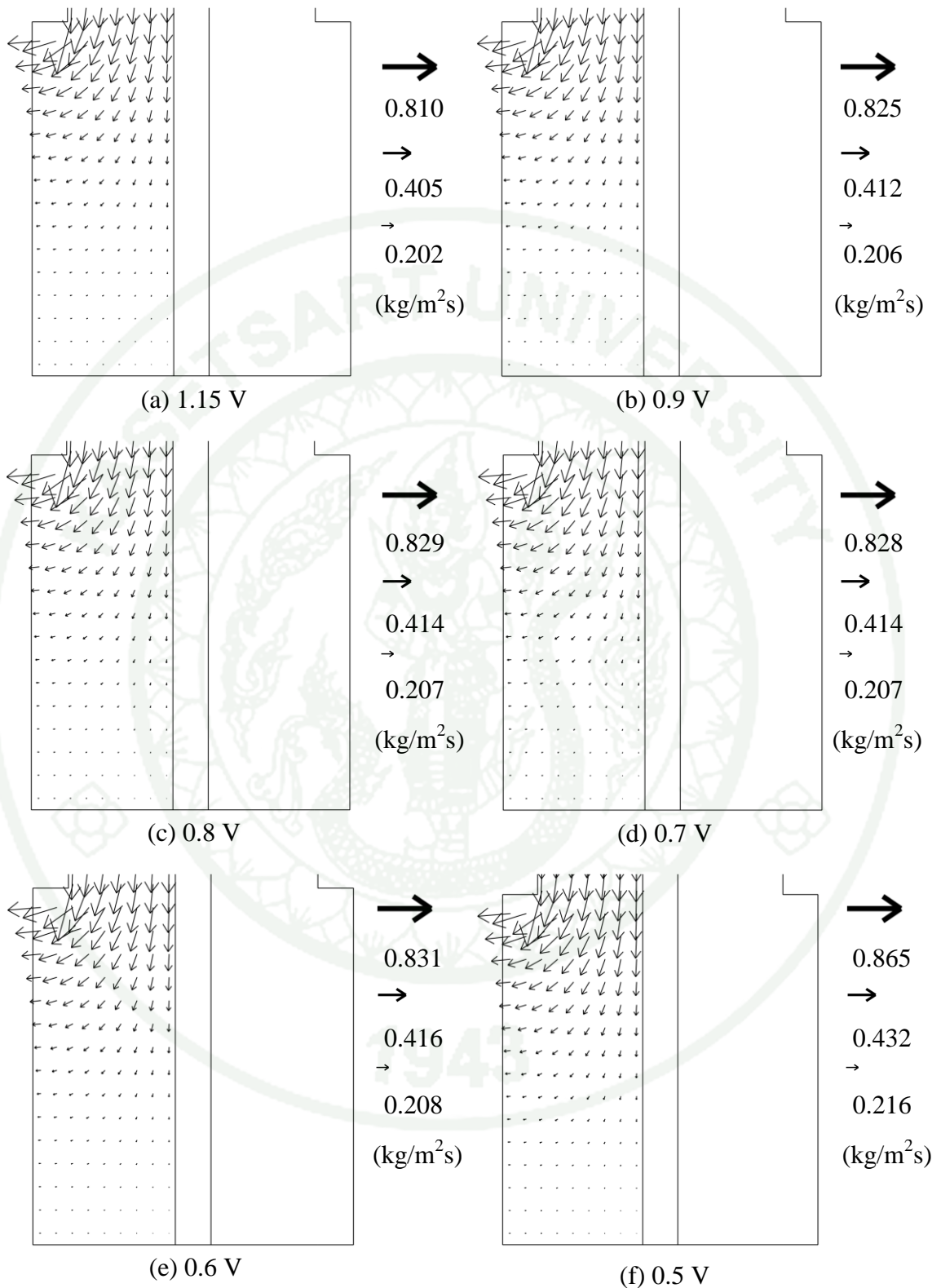
Appendix Figure A9 The total flux of hydrogen in the GDL at the exit region at various operating voltages.
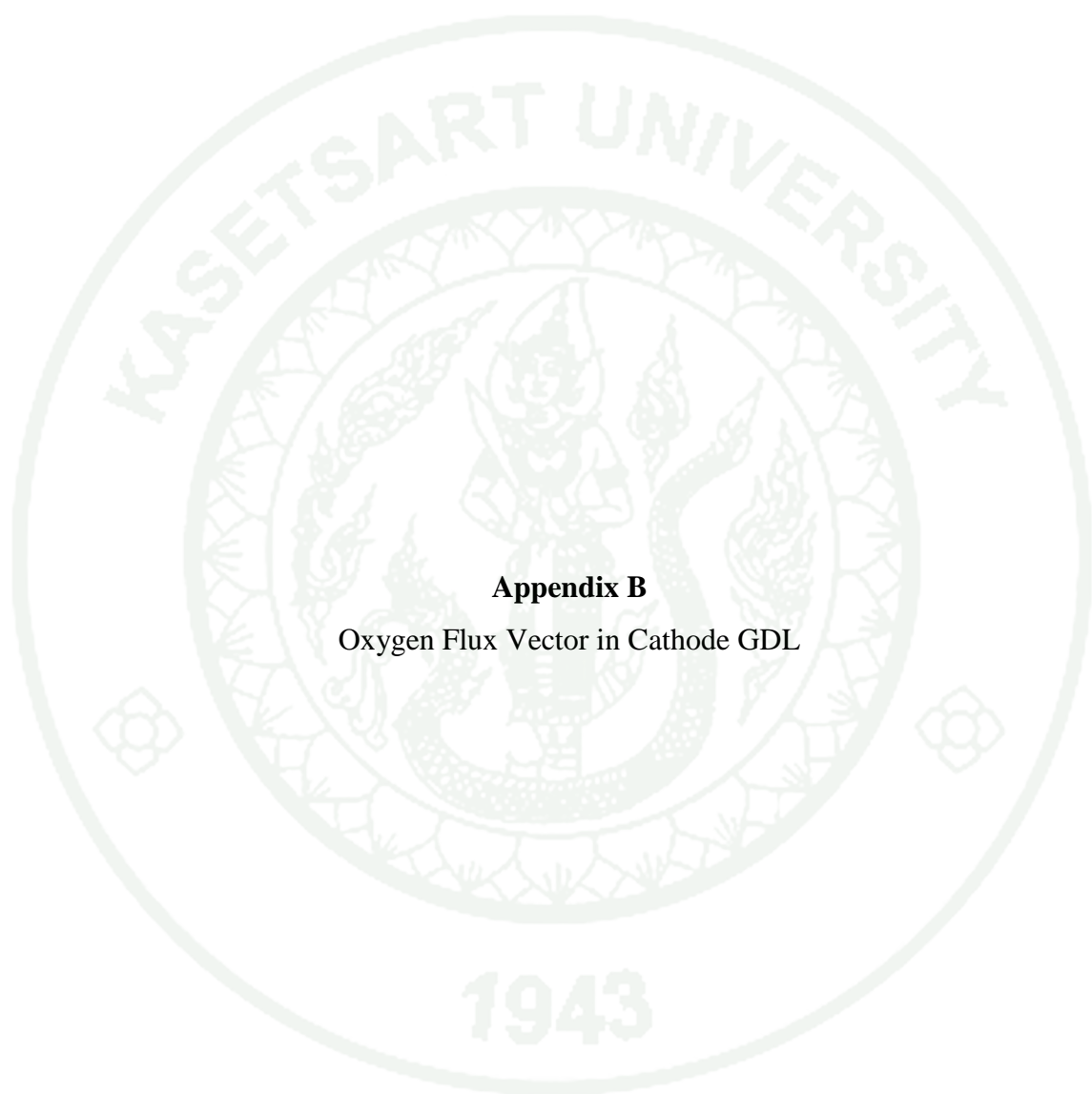
Appendix B

Oxygen Flux Vector in Cathode GDL
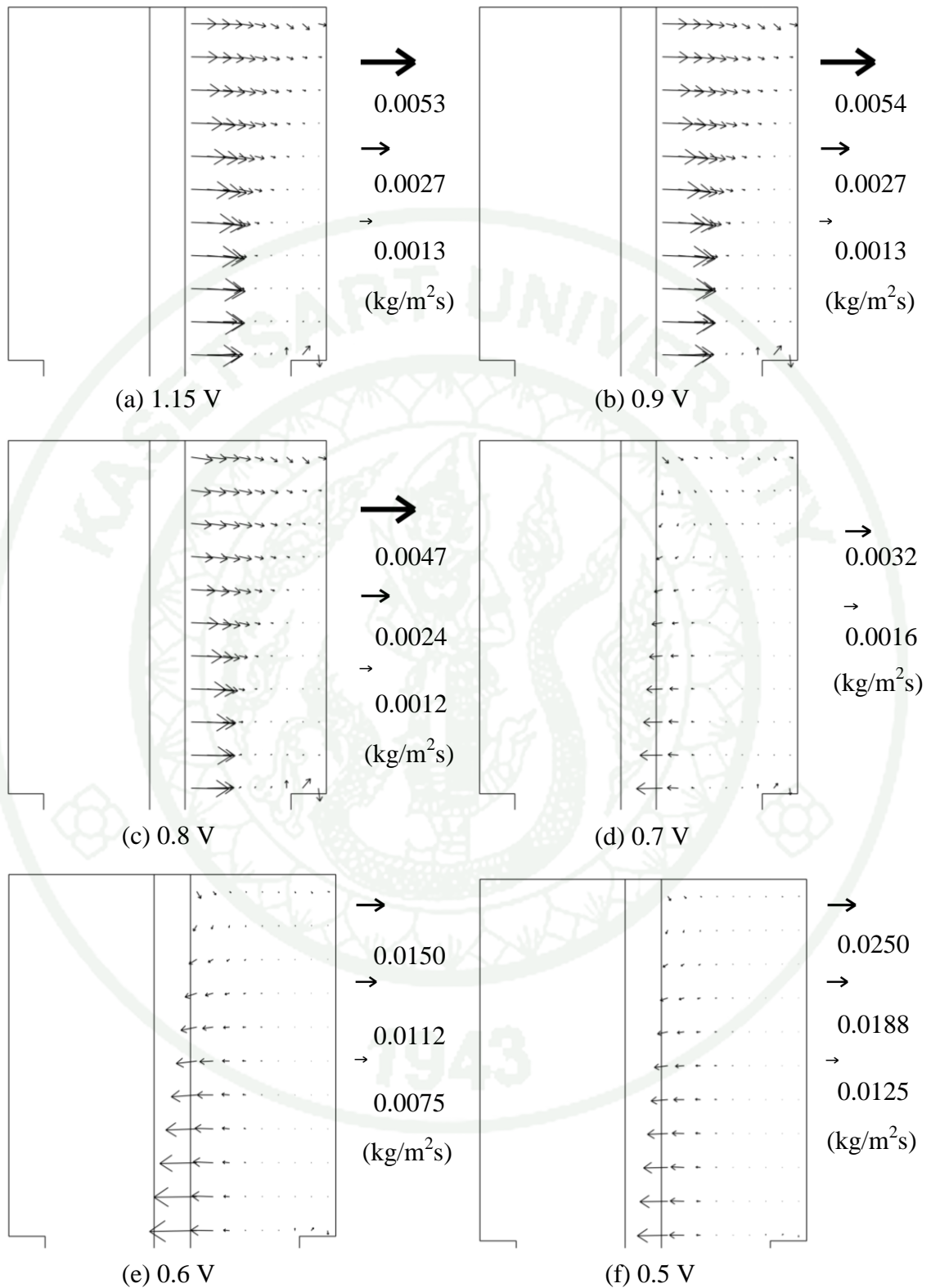
Appendix Figure B1 The diffusive flux of oxygen in the entrance region at various operating voltages.

(a) 1.15 V

(b) 0.9 V

(c) 0.8 V

(d) 0.7 V

(e) 0.6 V

(f) 0.5 V

Appendix Figure B2 The diffusion flux of oxygen in the GDL behind the channel rib at various operating voltages.

(a) 1.15 V

0.0052

0.0026

0.0013

(kg/m²s)

(b) 0.9 V

0.0052

0.0026

0.0013

(kg/m²s)

(c) 0.8 V

0.0058

0.0029

0.0014

(kg/m²s)

(d) 0.7 V

0.0100

0.0050

0.0025

(kg/m²s)

(e) 0.6 V

0.0197

0.0098

0.0049

(kg/m²s)

(f) 0.5 V

0.0268

0.0134

0.0067

(kg/m²s)

Appendix Figure B3 The diffusive flux of oxygen in the GDL at the exit region at various operating voltages.

→
4.714
→
3.536
→
2.357
(kg/m^{2}s)

(a) 1.15 V

→
4.714
→
3.536
→
2.357
(kg/m^{2}s)

(b) 0.9 V

→
4.712
→
3.534
→
2.356
(kg/m^{2}s)

(c) 0.8 V

→
4.705
→
3.529
→
2.352
(kg/m^{2}s)

(d) 0.7 V

→
4.636
→
3.477
→
2.318
(kg/m^{2}s)

(e) 0.6 V

→
4.682
→
3.512
→
2.341
(kg/m^{2}s)

(f) 0.5 V

Appendix Figure B4 The convective flux of oxygen in the entrance region at various operating voltages.

Appendix Figure B5 The convective flux of oxygen in the GDL behind the channel
rib at various operating voltages.
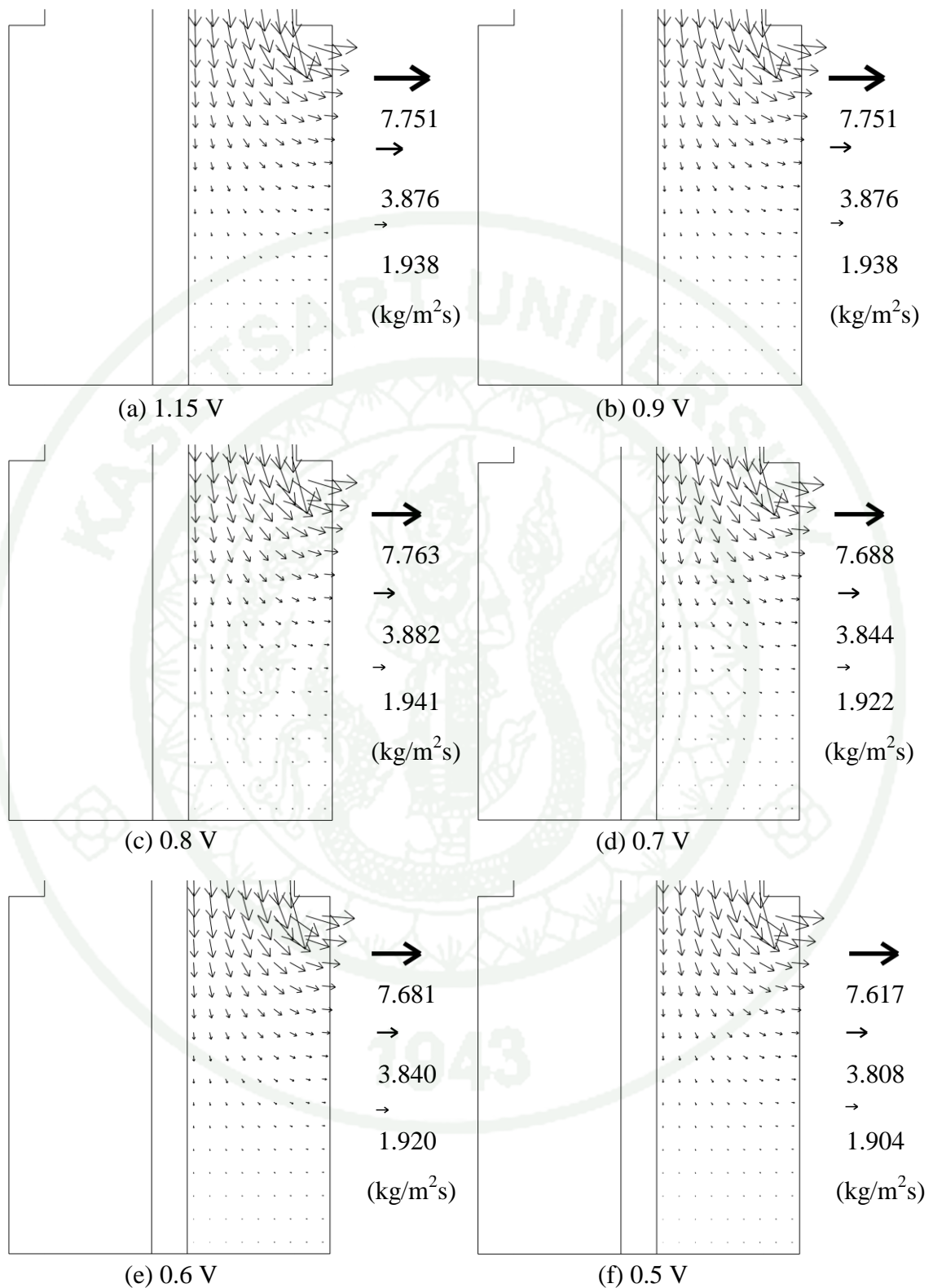
Appendix Figure B6 The convective flux of oxygen in the GDL at the exit region at various operating voltages.

(a) 1.15 V

→ 4.714
→ 3.536
→ 2.357
(kg/m²s)

(b) 0.9 V

→ 4.714
→ 3.536
→ 2.357
(kg/m²s)

(c) 0.8 V

→ 4.712
→ 3.534
→ 2.356
(kg/m²s)

(d) 0.7 V

→ 4.648
→ 3.486
→ 2.324
(kg/m²s)

(e) 0.6 V

→ 4.636
→ 3.477
→ 2.318
(kg/m²s)

(f) 0.5 V

→ 4.682
→ 3.512
→ 2.341
(kg/m²s)
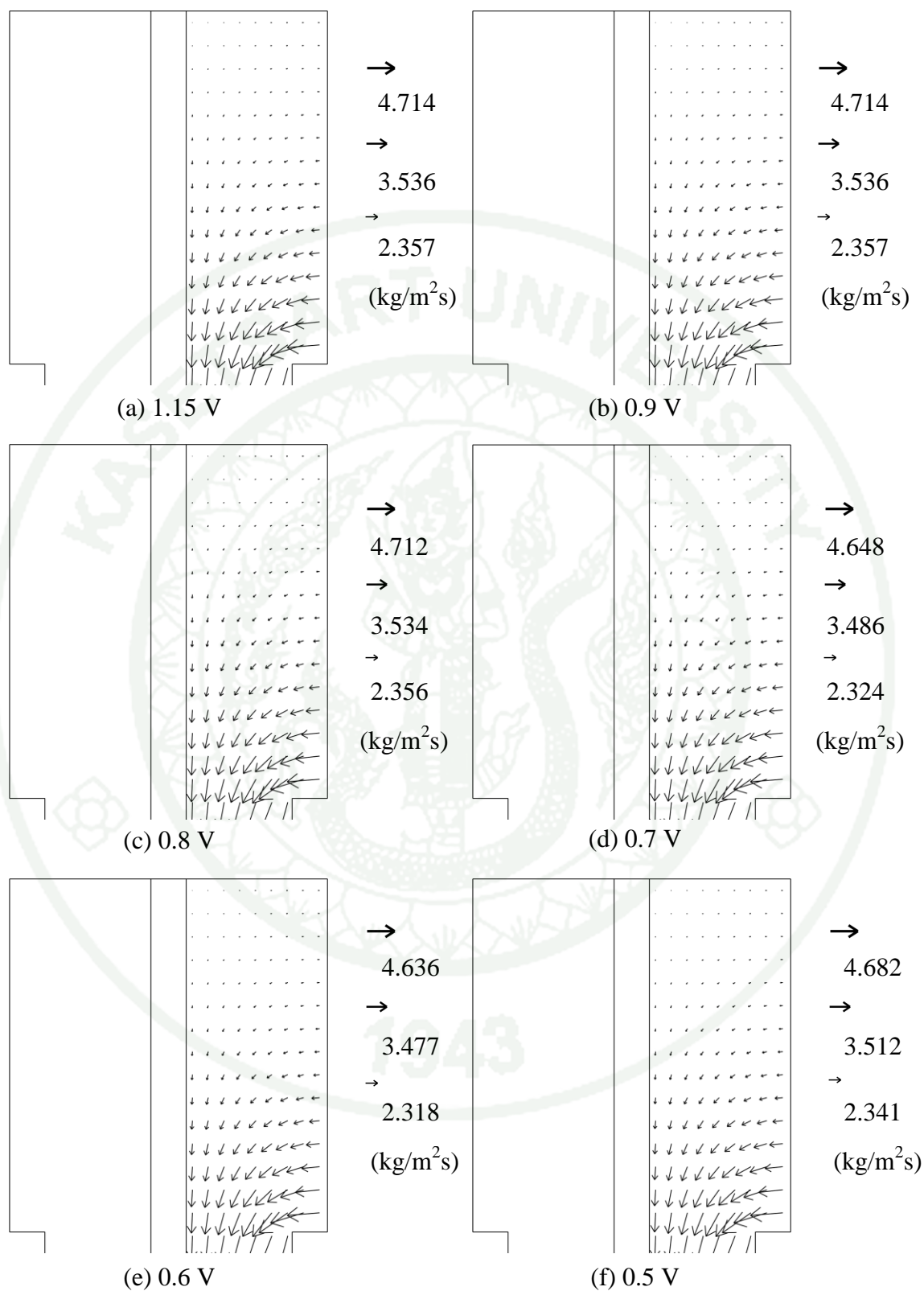
Appendix Figure B7 The total flux of oxygen in the entrance region at various
operating voltages.
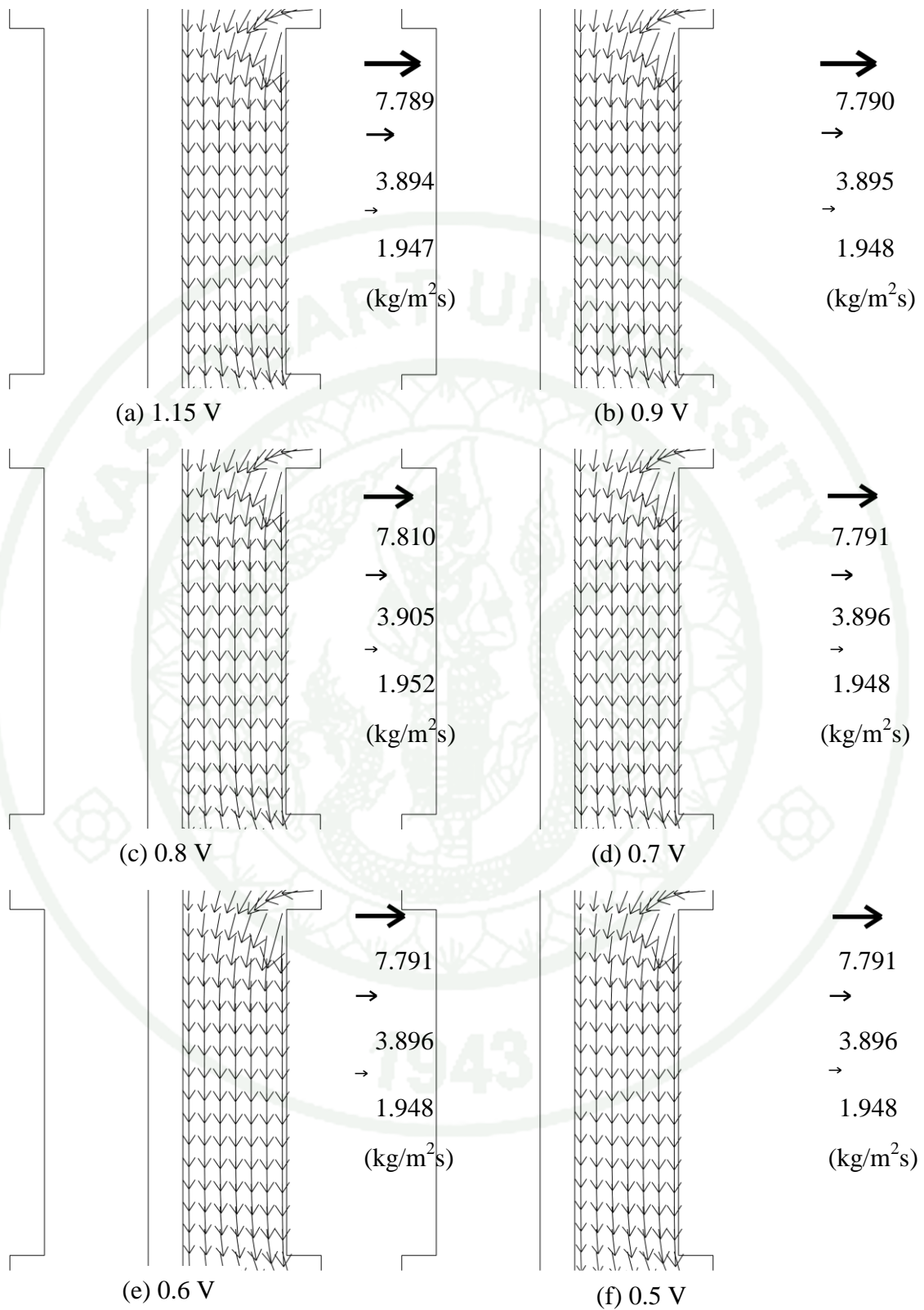
Appendix Figure B8 The total flux of oxygen in the GDL behind the channel rib at various operating voltages.

(a) 1.15 V

(b) 0.9 V

(c) 0.8 V

(d) 0.7 V

(e) 0.6 V

(f) 0.5 V
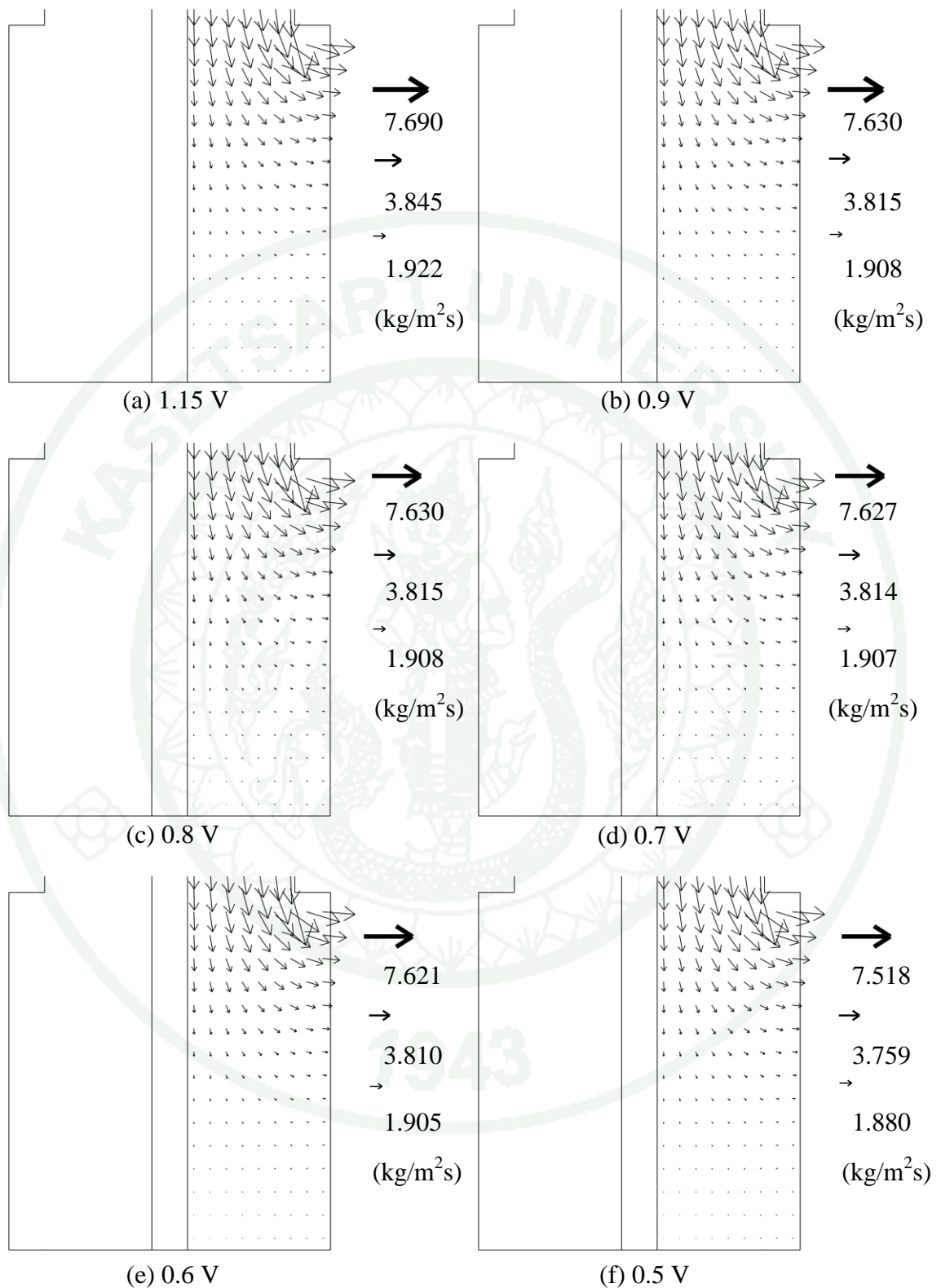
Appendix Figure B9 The total flux of oxygen in the GDL at the exit region at various operating voltages.
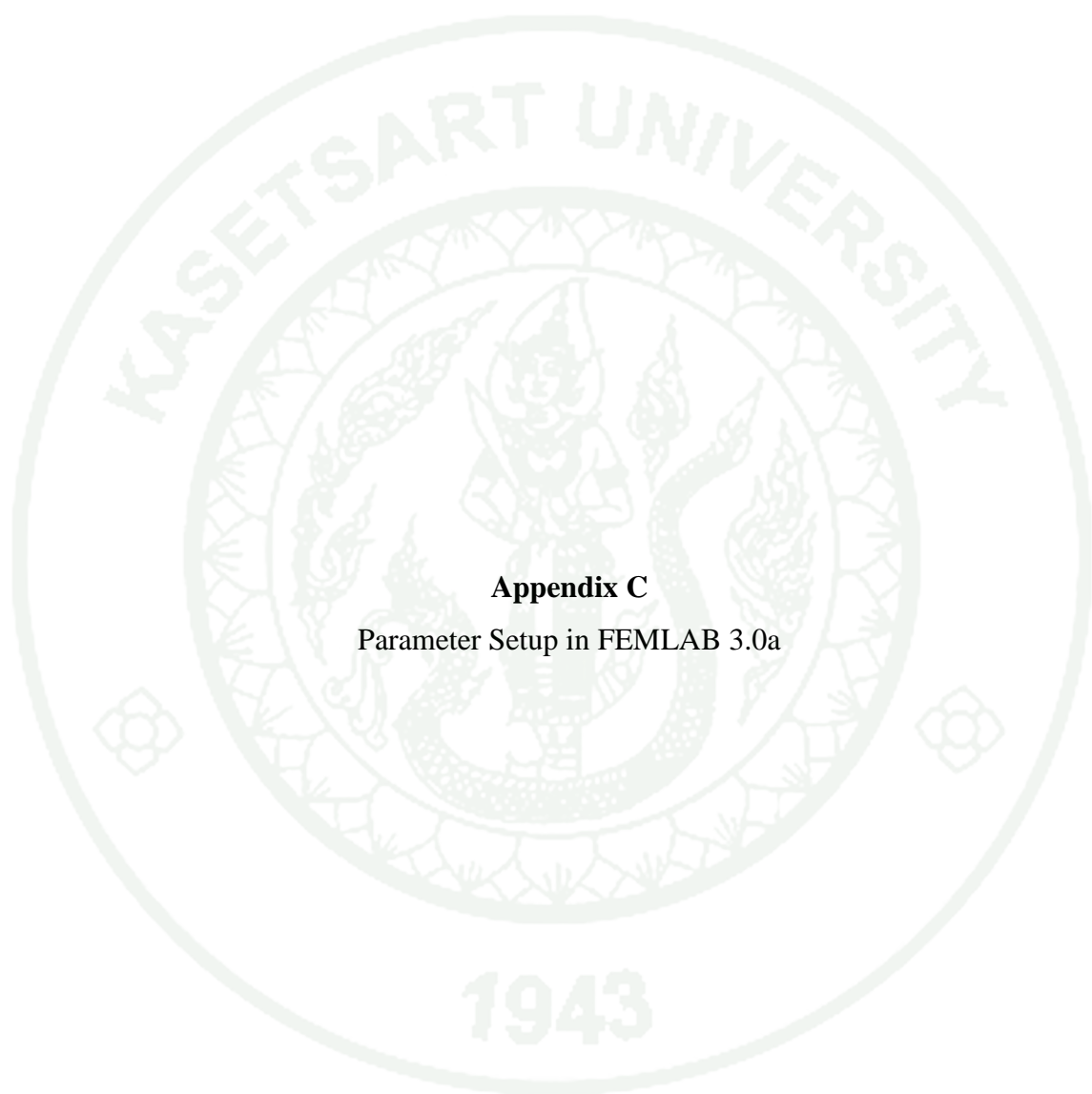
Appendix C

Parameter Setup in FEMLAB 3.0a

Appendix Table C1 Constants setup

Constants	Expressions	Descriptions
R	8.314[J/mol/K]	Gas constant
T*	353.15[K]	Humidified temperature
F	96485[C/mol]	Faraday's constant
kappa_p	1.76e-11[m^2]	Permeability of GDL
p_ref	1[atm]	Reference pressure
p_a_in	1.1*p_ref	Inlet pressure, anode
p_c_in	1.1*p_ref	Inlet pressure, cathode
E_eq_a	0[V]	Anode reversible voltage
i0_a	1[A/cm^2]	Anode exchange current density,
eps_mac	0.88	Gas diffusion layer's porosity
D0H2_H2O	9.15e-5[m^2/s]	Binary diffusivity at reference state
T0H2_H2O	307.1[K]	Reference temperature
D0O2_H2O	2.82e-5[m^2/s]	Binary diffusivity at reference state
T0O2_H2O	308.1[K]	Reference temperature
wH2Oa_in	(yH2Oa_in*MH2O)/(yH2Oa_in*MH2O+yH2a_in*MH2)	Water inlet mass fraction at anode
wH2a_in	1-wH2Oa_in	Hydrogen inlet mass fraction at anode
wO2c_in	yO2c_in*MO2/(yH2Oc_in*MH2O+yO2c_in*MO2)	Oxygen inlet mass fraction at cathode

Appendix Table C1 (Continued)

Constants	Expressions	Descriptions
wH2Oc_in	yH2Oc_in*MH2O/(yH2Oc_in*MH2O+yO2c_in*MO2)	Water inlet mass fraction at cathode
MH2	2[g/mol]	Hydrogen molecular weight
MH2O	18[g/mol]	Water molecular weight
MO2	32[g/mol]	Oxygen molecular weight
xH2_in	(wH2a_in/MH2)/(wH2a_in/MH2+(wH2Oa_in)/MH2O)	Hydrogen inlet mole fraction at anode
xO2_in	(wO2c_in/MO2)/(wO2c_in/MO2+wH2Oc_in/MH2O)	Oxygen inlet mole fraction at cathode
Mm	1.1[kg/mol]	Sulfonate Equivalent molecular weight of Nafion
rho_dry	1980[kg/m^3]	Dry Nafion® density
n_sat	2.5	Drag coefficient at saturation level (100°C)
p_sat_in	10^(-2.1794+0.02953*(-273+T)-9.1837e-005*(-273+T)^2+1.4454e-007*(-273+T)^3)[bar]	Water vapor saturation pressure
yH2Oa_in	p_sat_in/p_a_in	Water mole fraction at anode inlet
yH2a_in	1-yH2Oa_in	Hydrogen mole fraction at anode inlet
yH2Oc_in	p_sat_in/p_c_in	Water mole fraction at cathode inlet
yO2c_in	(1-yH2Oc_in)	Oxygen mole fraction at cathode inlet

Appendix Table C1 (Continued)

Constants	Expressions	Descriptions
L_cat	0.2	Catalyst loading
n_H2	2	Electron transfer number, anode
alp_H2	0.5	Charge transfer coefficient, anode
n_O2	2	Electron transfer number, cathode
V_cell*	1.15	Fuel cell output voltage
T_c*	353.15[K]	Operating temperature of fuel cell
A_vis	1.16145	Viscosity calculated constant
B_vis	0.14874	Viscosity calculated constant
C_vis	0.52487	Viscosity calculated constant
D_vis	0.7732	Viscosity calculated constant
E_vis	2.16178	Viscosity calculated constant
F_vis	2.43787	Viscosity calculated constant
sigmaH2O	2.641	Hard sphere diameter of water (Å)
epK_H2O	809.1[K]	Characteristic energy of water
sigmaH2	2.827	Hard sphere diameter of hydrogen (Å)
epK_H2	59.7[K]	Characteristic energy of Hydrogen

Appendix Table C1 (Continued)

Constants	Expressions	Descriptions
sigmaO2	3.467	Hard sphere diameter of oxygen (Å)
epK_O2	106.7[K]	Characteristic energy of oxygen

Appendix Table C2 Scalar expressions setup

Names	Expressions	Descriptions
eta_a	phi_s-phi_m-E_eq_a	Activation overpotential at anode
eta_c	phi_s-phi_m-E_eq_c	Activation overpotential at cathode
i_a	i0_a*(exp(n_H2*alp_H2*F*eta_a/R/T_m)-exp(-n_H2*(1-alp_H2)*F*eta_a/R/T_m))	Local current density at anode
i_c	i0_c*(exp(n_O2*alp_O2*F*eta_c/R/T_m)-exp(-n_O2*(1-alp_O2)*F*eta_c/R/T_m))	Local current density at cathode
D_lda	exp(2416*(1/303-1[K]/T_m))*(2.563-0.33*lda+0.0264*lda^2-0.000671*lda^3)*1e-6[cm^2/s]	Water diffusivity in Nafion® membrane
sigma_m	sigma_303*exp(1268*(1/303-1[K]/T_m))	Proton conductivity of Nafion® membrane

Appendix Table C2 (Continued)

Names	Expressions	Descriptions
E_eq_c	1.229[V]+(-163.23)*(T_cell-298.15)/2/F-(R*T_cell/2/F)*log(1/(yH2a_in*p_a_in/p_ref)/(yH2Oc_in*p_c_in/p_ref)^0.5)	Equilibrium potential of cathode reaction
Tdi_H2O	T_cell/epK_H2O	Dimensionless temperature, water
ome_H2O	A_vis*Tdi_H2O^(-B_vis)+C_vis*exp(-D_vis*Tdi_H2O)+E_vis*exp(-F_vis*Tdi_H2O)	Collision integral of water
vis_h2o	26.69e-7[Pa*s]*((18[1/K]*T_cell)^0.5)/((sigmaH2O^2)*ome_H2O)	Viscosity of water vapor
Tdi_H2	T_cell/epK_H2	Dimensionless temperature, hydrogen
ome_H2	A_vis*Tdi_H2^(-B_vis)+C_vis*exp(-D_vis*Tdi_H2)+E_vis*exp(-F_vis*Tdi_H2)	Collision integral of hydrogen
vis_h2	26.69e-7[Pa*s]*((2[1/K]*T_cell)^0.5)/((sigmaH2^2)*ome_H2)	Viscosity of hydrogen gas
Tdi_O2	T_cell/epK_O2	Dimensionless temperature, oxygen
ome_O2	A_vis*Tdi_O2^(-B_vis)+C_vis*exp(-D_vis*Tdi_O2)+E_vis*exp(-F_vis*Tdi_O2)	Collision integral of oxygen
vis_O2	26.69e-7[Pa*s]*((32[1/K]*T_cell)^0.5)/((sigmaO2^2)*ome_O2)	Viscosity of oxygen gas
k_eff	0.4133[W/m/K]-(4e-4[W/m/K^2]*T_cell)	Effective thermal conductivity of Nafion®

Appendix Table C3 Subdomain expressions setup

(a) Subdomain 1: Anode gas diffusion layer

Name	Expressions
rho_mix	(x_wH2_MSa*MH2+x_wH2Oa_MSa*MH2O)*p_gdl/(R*T_s)
E	phi_s
xH2	x_wH2_MSa
wReact	wH2
wH2O	wH2Oa
T_cell	T_s
p_sat	10^(-2.1794+0.02953*(-273+T_s)-9.1837e-005*(-273+T_s)^2+1.4454e-007*(-273+T_s)^3)[bar]
D_H2H2O	D0H2_H2O*p_ref*(T_s/T0H2_H2O)^1.5/p_gdl
D_effH2H2O	D_H2H2O*eps_mac^1.5
vis_a	(1.414*xH2*vis_h2+4.243*(1-xH2)*vis_h2o)/(1.414*xH2+4.243*(1-xH2))

Appendix Table C3 (Continued)

(b) Subdomain 2: Nafion[®] membrane

Name	Expressions
E	phi_m
lda	cH2O*Mm/rho_dry
sigma_303	100*(-0.00326+0.005193*lda)
T_cell	T_m
p_sat	10^(-2.1794+0.02953*(-273+T_m)-9.1837e-005*(-273+T_m)^2+1.4454e-007*(-273+T_m)^3)[bar]
n_drag	n_sat*lda/22

Appendix Table C3 (Continued)

(c) Subdomain 3: Cathode gas diffusion layer

Name	Expressions
rho_mix	(x_wO2_MSc*MO2+x_wH2Oc_MSc*MH2O)*p_gdl/(R*T_s)
E	phi_s
xO2	x_wO2_MSc
wReact	wO2
wH2O	wH2Oc
T_cell	T_s
p_sat	10^(-2.1794+0.02953*(-273+T_s)-9.1837e-005*(-273+T_s)^2+1.4454e-007*(-273+T_s)^3)[bar]
D_O2H2O	D0O2_H2O*p_ref*(T_s/T0O2_H2O)^1.5/p_gdl
D_effO2H2O	D_O2H2O*eps_mac^1.5
D_O2N2	D0O2_N2*p_ref*(T_s/T0O2_N2)^1.5/p_gdl
D_effO2N2	D_O2N2*eps_mac^1.5
D_N2H2O	D0H2O_N2*p_ref*(T_s/T0H2O_N2)^1.5/p_gdl
D_effN2H2O	D_N2H2O*eps_mac^1.5
vis_c	(5.657*xO2*vis_O2+4.243*(1-xO2)*vis_h2o)/(5.657*xO2+4.243*(1-xO2))

Appendix Table C4 boundary expressions setup

(a) Boundary 1: reactive boundary layer at anode

Names	Expressions
u_a	i_a*(0.5*MH2+n_drag*MH2O)/(F*rho_mix)
aw	x_wH2Oa_MSa*p_gdl/p_sat
lda	(0.0043+17.81*aw-39.85*aw^2+36*aw^3)*(aw>0)*(aw<=1)+(14+1.4*(-1+aw))*(aw>1)*(aw<=3)

(b) Boundary 1: reactive boundary layer at cathode

Names	Expressions
u_c	i_c*(0.25*MO2-(0.5+n_drag)*MH2O)/(F*rho_mix)
aw	x_wH2Oc_MSc*p_gdl/p_sat
lda	(0.043+17.81*aw-39.85*aw^2+36*aw^3)*(aw>0)*(aw<=1)+(14+1.4*(-1+aw))*(aw>1)*(aw<=3)
i0_c	7657000[mA/cm^2]*exp((-7366)[K]/T_cell+1.315*L_cat)
alp_O2	0.001678[1/K]*T_cell
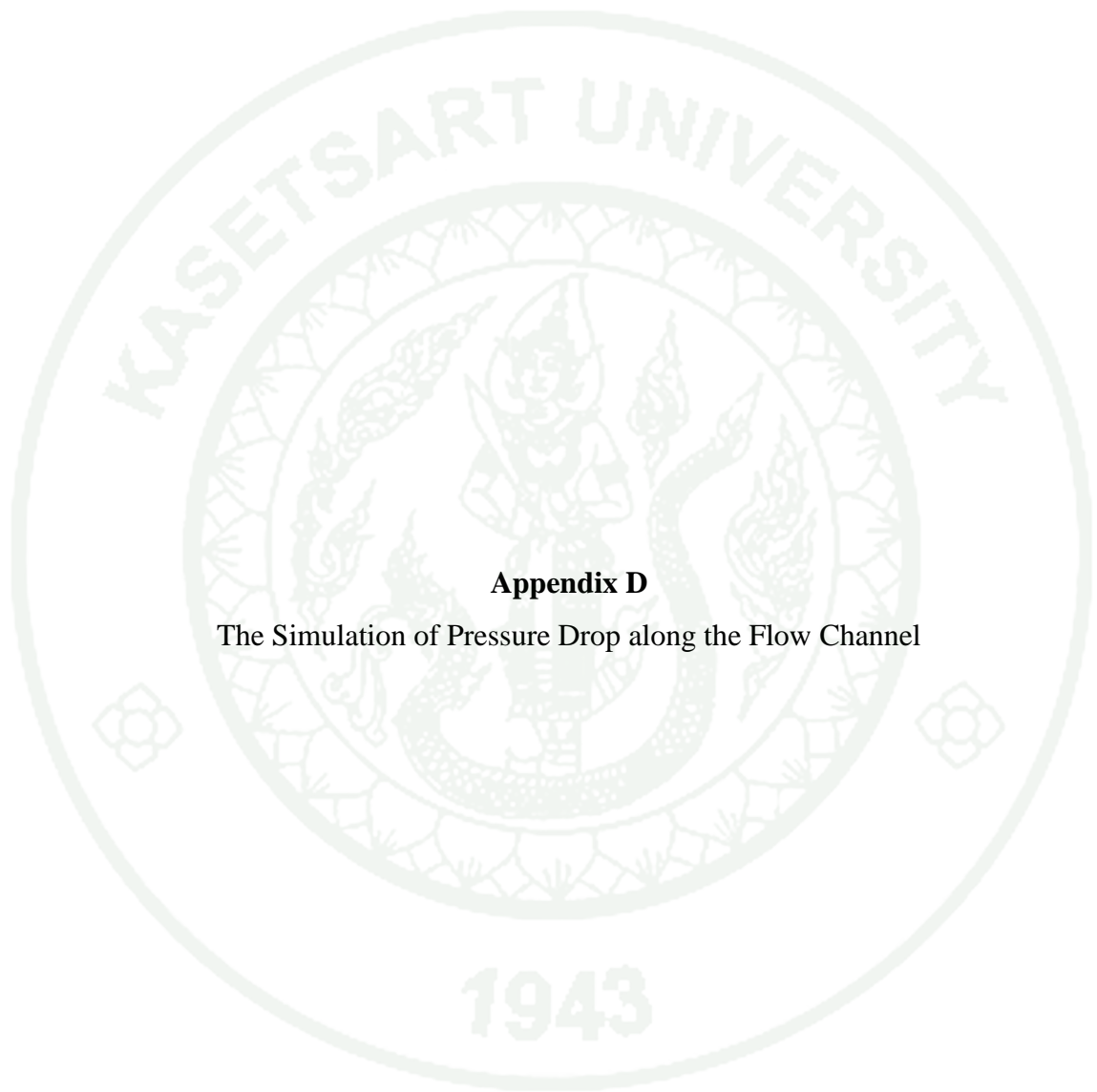
Appendix D

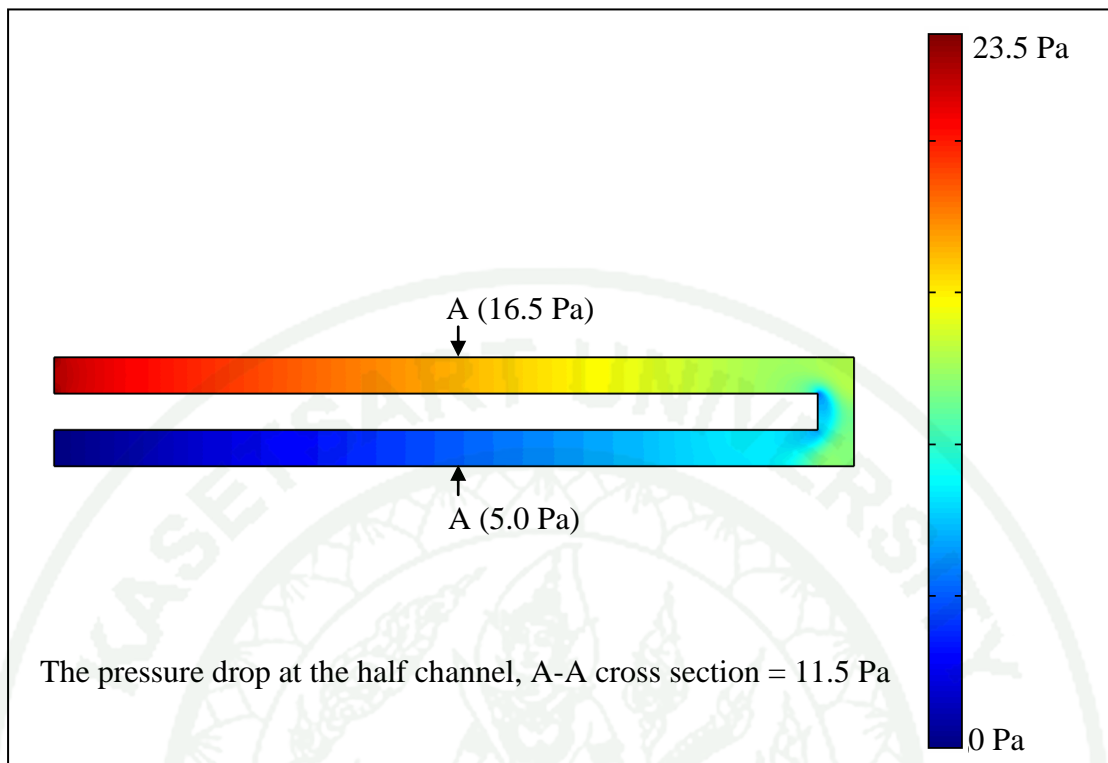The Simulation of Pressure Drop along the Flow Channel

The geometry of flow channel is show in **Appendix Figure D1**. It consists of two channels connected at the end. The width of the channel is 1 mm and the channel length is 22 mm. The upper channel is the inlet channel and the lower channel is the outlet channel. The geometry configuration is the same of both anode and cathode.
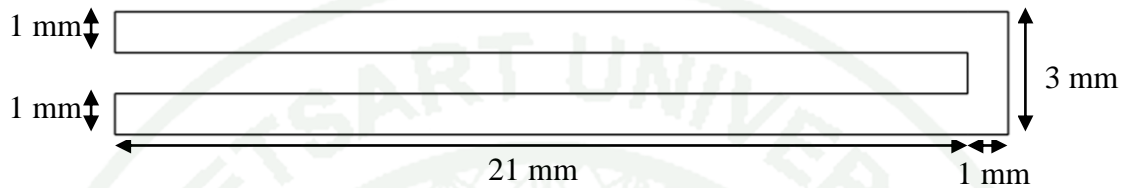

Appendix Figure D1 The geometry of flow channel.

Hydrogen is used as a fuel at the anode and oxygen is an oxidant at the cathode. The anode gas flow rate is 0.2 L/min and the cathode gas flow rate is 0.1 L/min. The fed gases are fully humidified. The operating temperature is 80°C and the operating pressure is 1 atm.

The pressure distribution is calculated by Navier-Stoke's equation. The simulation is done at steady state, isothermal, and fully developed flow. Assumed the ideal gas law is applied. The pressure distributions are shown in **Appendix Figure D2** and **D3** for anode and cathode, respectively.

**Appendix Figure D2** The pressure distribution in anode flow channel
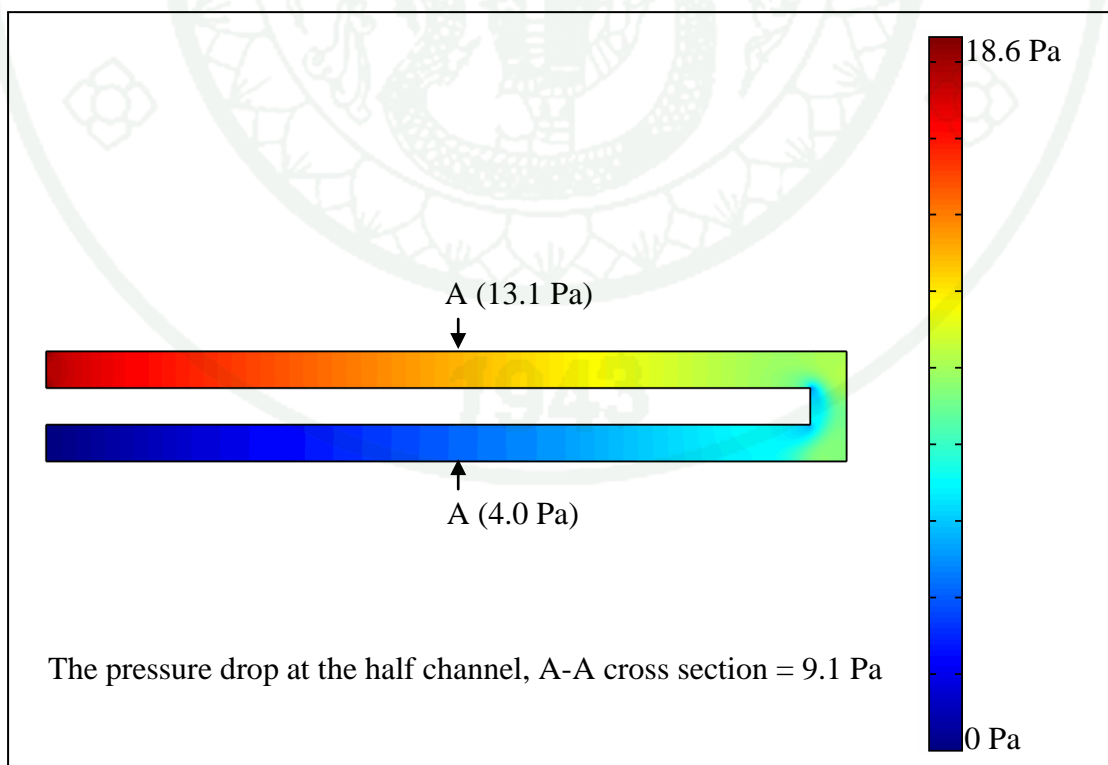
Appendix Figure D3 The pressure distribution in cathode flow channel
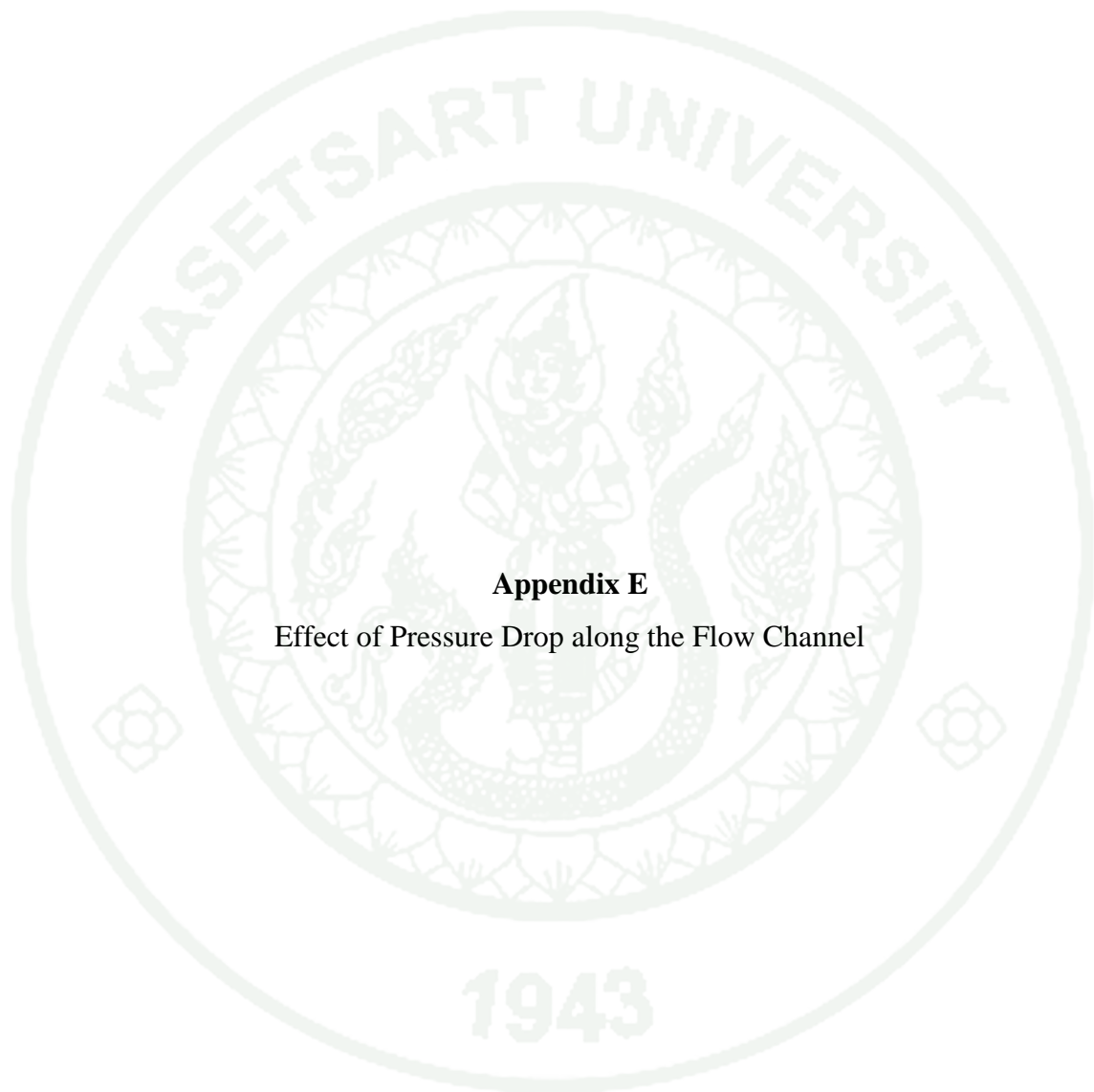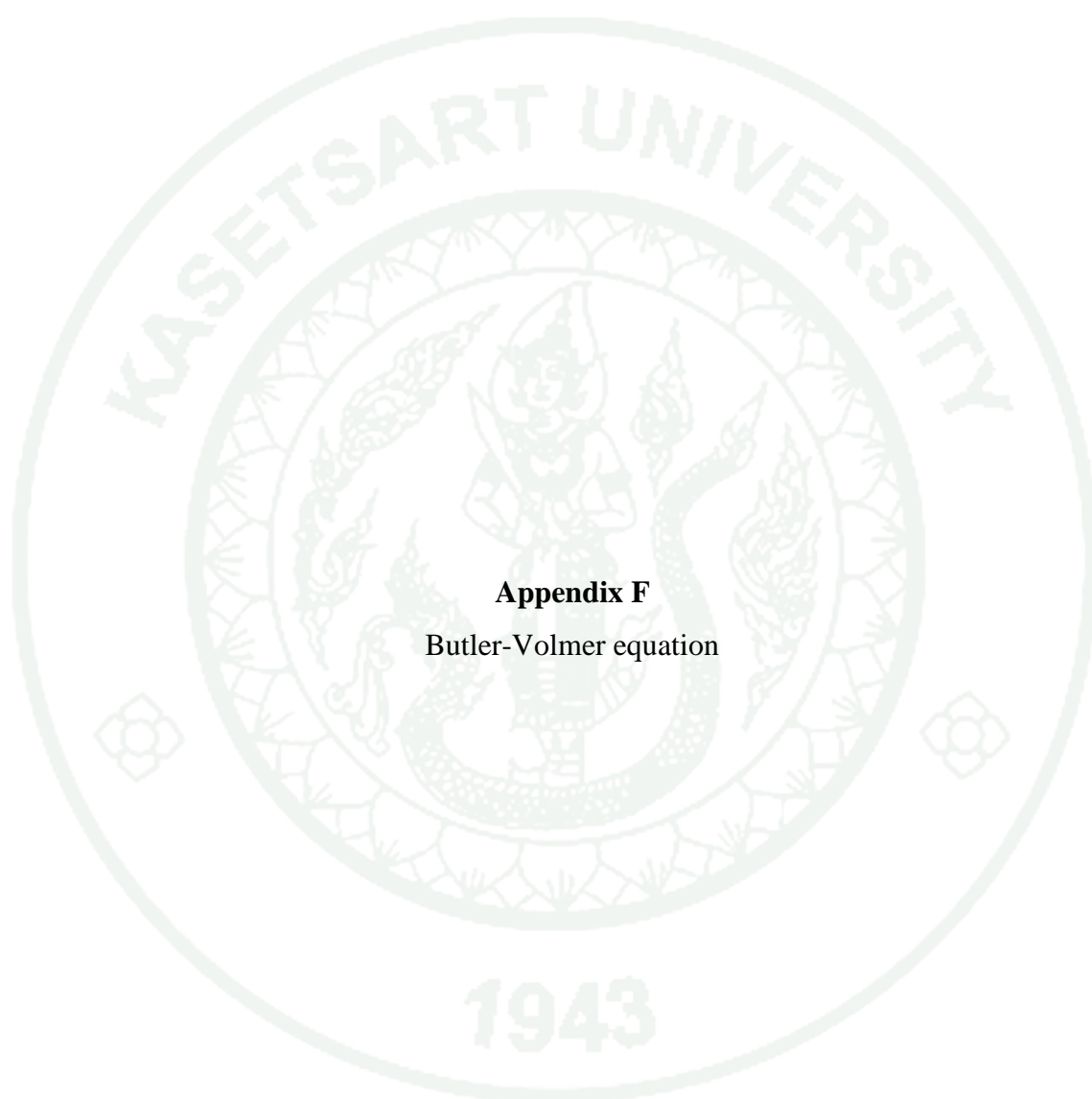
Appendix E

Effect of Pressure Drop along the Flow Channel

The pressure drop along the flow channel is difference when the difference operating flow rate is applied. The detail of pressure drop along the flow channel is presented in **Appendix D**. The simulated polarization curve at various pressure drop is plotted in **Appendix Figure E1**. The pressure drop is varied to 2 and 3 times of the normal operating condition, 11.5 Pa for anode and 9.1 Pa for cathode. The results shows that the polarization curves are nearly the same. Therefore, in this simulation, the increasing of pressure drop have a small effect to the polarization curve. This simulation result does not reflect the phenomena usually observed in experiment. This discrepancy should be further clarified.
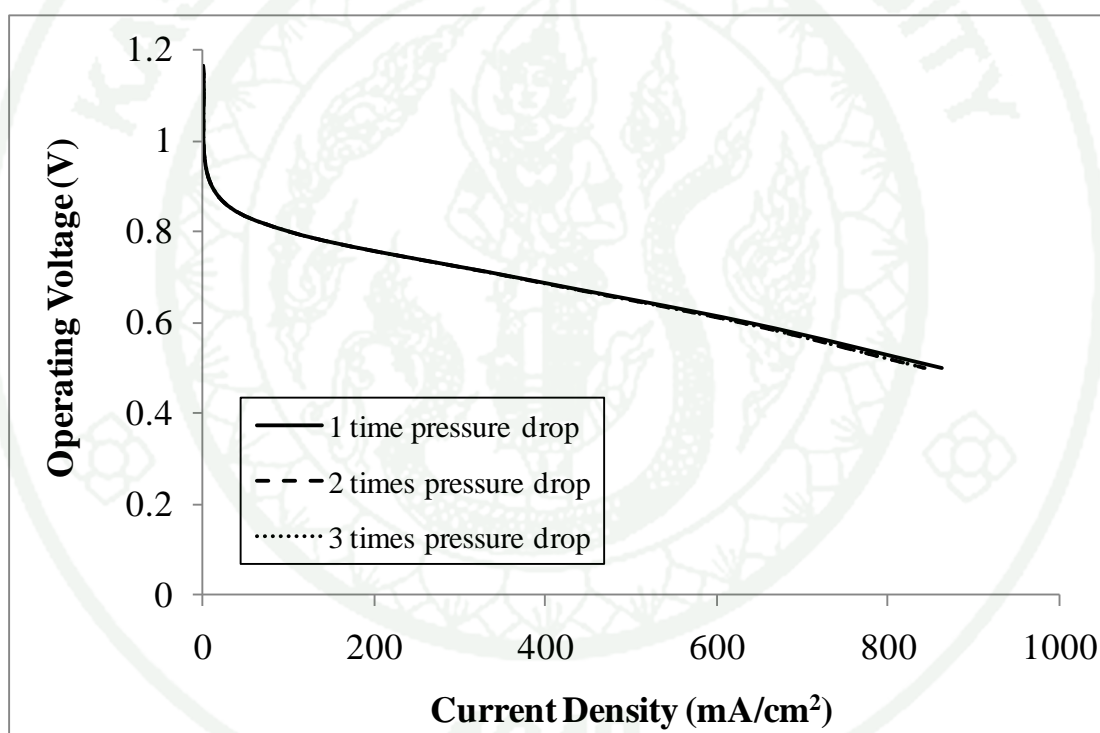

Appendix Figure E1 The polarization curve at various pressure drop along the flow channel. The pressure drops at normal operating condition for the experiment are 16.5 Pa and 14.1 Pa for anode and cathode, respectively.

Appendix F

Butler-Volmer equation

The net rate of reaction is given by the difference rates between the forward and reverse reactions.

Forward reaction: $M \cdots H \rightarrow (M + e^-) + H^+$ Oxidation

Reverse reaction: $(M + e^-) + H^+ \rightarrow M \cdots H$ Reduction
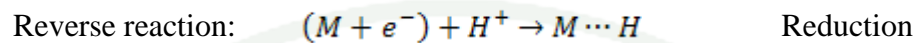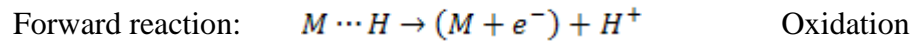
At equilibrium, the current densities for the forward and reverse reactions are both given by exchange current density (j_0). Away from the equilibrium, the forward and reverse current densities can be write by starting from j_0 and taking into the changes in the forward and reverse activation barriers.

$$j_{fw} = j_0 exp(\alpha nF\eta/RT) \tag{94}$$

$$j_{rev} = j_0 exp(-(1-\alpha)nF\eta/RT) \tag{95}$$

The net current ($j_{fw} - j_{rev}$) is then

$$j_{net} = j_0[exp(\alpha nF\eta/RT) - exp(-(1-\alpha)nF\eta/RT)] \tag{96}$$

$$\text{\textit{Oxidation}} \qquad\qquad \text{\textit{Reduction}}$$

This equation is known as the Butler-Volmer equation. Then, the value of an activation overvoltage for each reaction can be considered. If the activation overvoltage is positive, the oxidation term is dominated and the reduction term is neglected. This refers to the anode reaction. In contrast, if the activation overvoltage is negative, the reduction term is dominated and the oxidation term is neglected. This refers to the cathode reaction.

The calculation of activation overvoltage is done by subtracting the reversible potential from the chemical energy of the reaction system, see **Appendix Figure F1** (O'Hayre, 2009). The electrical potential of the system is equal to the decreasing of potential from electrode to membrane. Thus the expression of activation overvoltage at anode and cathode are

$$\eta_{act,a} \quad = \quad \varphi_{P,a} - \varphi_{R,a} - E_{rev,a} \quad = \quad \varphi_{GDL,s} - \varphi_{m,a} - E_{eq,a} \qquad (97)$$

$$\eta_{act,c} \quad = \quad \varphi_{P,c} - \varphi_{R,c} - E_{eq,c} \quad = \quad \varphi_{GDL,c} - \varphi_{m,c} - E_{eq,c} \qquad (98)$$
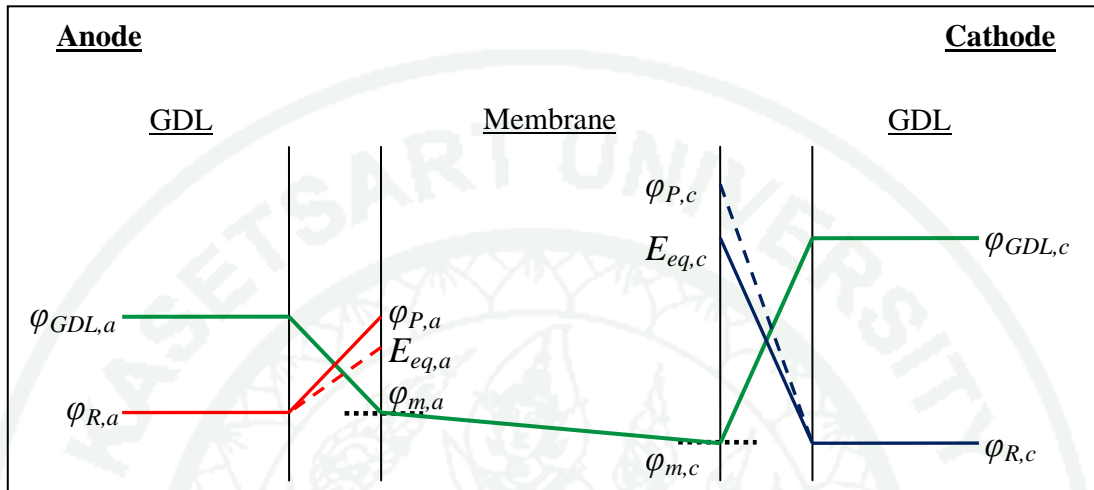
Appendix Figure F1 The potential diagram. φ_{GDL} is GDL potential, φ_m is a membrane potential, φ_R is potential of reactant, φ_P is potential of product, and E_{eq} is an equilibrium potential. The subscripts a and c refer to anode and cathode, respectively.

CURRICULUM VITAE

NAME   : Mr. Kitipoom Tangwongpimook

BIRTH DATE   : October 12, 1984

BIRTH PLACE : Bangkok, Thailand

EDUCATION   : <u>**YEAR**</u>   <u>**INSTITUTE**</u>   <u>**DEGREE/DIPLOMA**</u>

2005   Kasetsart Univ.   B.Sc.(Chemistry)

SCHOLARSHIP :   National Center of Excellence for Petroleum, Petrochemical

and Advanced Materials through Department of Chemical

Engineering at Kasetsart University